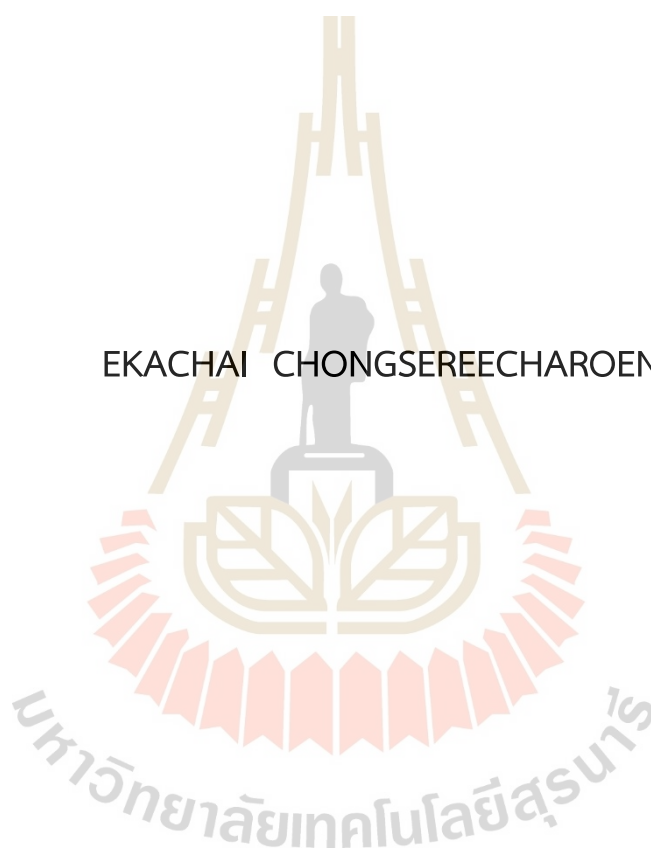


PREPARATION AND CHARACTERIZATION OF SPUTTERED METAL
OXIDE MULTILAYER THIN FILMS FOR OPTICAL APPLICATION

EKACHAI CHONGSEREECHAROEN



A Thesis Submitted in Partial Fulfillment of the Requirements for the
Degree of Doctor of Philosophy in Applied Physics
Suranaree University of Technology
Academic Year 2021

การเตรียมฟิล์มบางหลายชั้นโลหะออกไซด์ด้วยเทคนิคสเปตเตอร์ริง
และการหาลักษณะเฉพาะเพื่อการประยุกต์ใช้เชิงแสง



วิทยานิพนธ์นี้เป็นส่วนหนึ่งของการศึกษาตามหลักสูตรปริญญาวิทยาศาสตรดุษฎีบัณฑิต
สาขาวิชาฟิสิกส์ประยุกต์
มหาวิทยาลัยเทคโนโลยีสุรนารี
ปีการศึกษา 2564

PREPARATION AND CHARACTERIZATION OF SPUTTERED METAL OXIDE
MULTILAYER THIN FILMS FOR OPTICAL APPLICATION


Suranaree University of Technology has approved this thesis submitted in
partial fulfillment of the requirements for the Degree of Doctor of Philosophy

Thesis Examining Committee




(Prof. Dr. Rattikorn Yimnirun)

Chairperson



(Assoc. Prof. Dr. Prayoon Songsirittthigul)

Member (Thesis Advisor)



(Assoc. Prof. Dr. Saroj Rujirawat)

Member



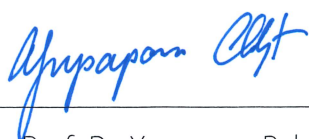
(Assoc. Prof. Dr. Prapan Manyum)

Member



(Dr. Narong Chanlek)

Member



(Assoc. Prof. Dr. Yupaporn Ruksakulpiwat)

Vice Rector for Academic Affairs
and Quality Assurance



(Prof. Dr. Santi Maensiri)

Dean of Institute of Science

เอกชัย จงเสรีเจริญ : การเตรียมฟิล์มบางหลายชั้นโลหะออกไซด์ด้วยเทคนิคสเปตเตอร์ริงและการหาลักษณะเฉพาะเพื่อการประยุกต์ใช้เชิงแสง (PREPARATION AND CHARACTERIZATION OF SPUTTERED METAL OXIDE MULTILAYER THIN FILMS FOR OPTICAL APPLICATION) อาจารย์ที่ปรึกษา : รองศาสตราจารย์ ดร.ประยูร สงศิริฤทธิกุล, 107 หน้า

คำสำคัญ: ฟิล์มบางโลหะออกไซด์, ฟิล์มบางหลายชั้น

โลหะออกไซด์เป็นวัสดุที่มีบทบาทสำคัญสำหรับการใช้เป็นวัสดุเคลือบเชิงแสงเนื่องจากมีสมบัติที่สามารถปรับเปลี่ยนได้หลายประการ เช่น ความโปร่งแสง ความมีเสถียรภาพต่อสภาวะแวดล้อมและสารเคมี เป็นต้น ไทเทเนียมไดออกไซด์และซิลิกอนไดออกไซด์คือวัสดุที่เป็นที่รู้จักอย่างดีในการนำไปใช้เป็นวัสดุเคลือบผิวเชิงแสง ในงานวิจัยนี้ ฟิล์มบางไทเทเนียมไดออกไซด์ถูกเตรียมด้วยกระบวนการอาร์เอฟแมกนีตรอนสเปตเตอร์ริงแบบดั้งเดิมและแบบที่มีวิธีการรีแอคทีฟแก๊สไทมมิง (RGT) สำหรับฟิล์มบางไทเทเนียมไดออกไซด์ถูกเตรียมด้วยกระบวนการอาร์เอฟแมกนีตรอนสเปตเตอร์ริงแบบดั้งเดิมนั้น ฟิล์มที่เตรียมได้ทุกชั้นมีค่าการส่งผ่านที่สูงมากกว่าร้อยละ 85 ในช่วงแสงที่ตามองเห็น ค่าการส่งผ่านของฟิล์มมีแนวโน้มลดลงเมื่อเตรียมด้วยความดันขณะเคลือบที่มีค่าสูง ผลจากการวัดด้วยเทคนิคการดูดกลืนรังสีเอกซ์ (XANES) ฟิล์มบางทุกเงื่อนไขมีโครงสร้างเป็นการผสมกันของเฟสรูไทล์และอนาเทส และผลการวิเคราะห์โครงสร้างเฉพาะบริเวณ (EXAFS) พบว่าที่การเตรียมด้วยความดันต่ำจะส่งผลให้ระยะพันธะไกลกว่าที่การเตรียมด้วยความดันสูง

สำหรับการเตรียมฟิล์มบางไทเทเนียมไดออกไซด์ด้วยกระบวนการอาร์เอฟแมกนีตรอนสเปตเตอร์ริงแบบ RGT ที่ความดันขณะเคลือบและกำลังที่ใช้เคลือบคงที่ เงื่อนไขการเตรียมที่ใช้สำหรับการศึกษานี้คือช่วงระยะเวลาที่ปล่อยให้ไหลเข้าและหยุดการไหลของแก๊สออกซิเจนเข้าไปขณะเคลือบจากผลการวัดสมบัติเชิงแสงด้วยเครื่องวัดการดูดกลืนแสงชนิดแบบอัลตราไวโอเล็ตและแสงมองเห็นพบว่า ค่าการส่งผ่านของชั้นงานที่เคลือบจะแตกต่างจากชั้นงานที่ไม่ถูกเคลือบอย่างเห็นได้ชัดตำแหน่งที่มีค่าการส่งผ่านสูงสุดของตัวอย่างที่ให้แก๊สออกซิเจนในช่วงที่สั้นกว่าจะมีตำแหน่งที่ค่าความยาวคลื่นสูงกว่า และโดยเฉลี่ยแล้วค่าการส่งผ่านของชั้นงานที่เคลือบจะมีค่าน้อยกว่าชั้นงานที่ไม่ได้เคลือบด้วยฟิล์มไทเทเนียมไดออกไซด์ ผลจากการวัดด้วยเทคนิค XANES พบโครงสร้างที่ผสมกันของเฟสรูไทล์และอนาเทส ซึ่งในการหาสัดส่วนของเฟสรูไทล์ต่ออนาเทสในโครงสร้างของฟิล์มจะใช้เทคนิคการรวมกันเชิงเส้น ซึ่งผลที่ได้สอดคล้องเป็นอย่างดีกับผลจากการวัดด้วยเทคนิคการเลี้ยวเบนของรังสีเอกซ์ นอกจากนี้ มีการแสดงผลจากการหาแนวโน้มของกราฟ EXAFS เพื่อดูระยะของพันธะในฟิล์มที่เตรียมได้อีกด้วย

ฟิล์มบางหลายชั้นของไทเทเนียมไดออกไซด์และซิลิกอนไดออกไซด์ ถูกเตรียมและศึกษา ลักษณะเฉพาะ ชั้นฟิล์มของซิลิกอน ไดออกไซด์ถูกเตรียมด้วยเทคนิคสปัตเตอร์ริงแบบ RGT เคลือบลง บนชั้นฟิล์มไทเทเนียมไดออกไซด์ในหลาย ๆ ชั้นงานที่ถูกเตรียมด้วยเงื่อนไขต่าง ๆ ก่อนหน้านี้ ฟิล์ม บางหลายชั้นที่เตรียมได้มีสเปกตรัมค่าการส่งผ่านที่เปลี่ยนไปจากสเปกตรัมที่ได้จากฟิล์มบางชั้นเดียว โดยจะมีตำแหน่งที่ให้ค่าการส่งผ่านสูงสุดเลื่อนไปทางความยาวคลื่นที่สูงกว่า ในกรณีนี้เตรียมด้วยการ ให้แก๊สออกซิเจนในช่วงที่สั้นกว่า ค่าการส่งผ่านโดยเฉลี่ยของฟิล์มบางหลายชั้น พบว่ามีค่าสูงกว่าฟิล์ม บางชั้นเดียว จากผลการทดลองเหล่านี้ทำให้ได้ว่า ฟิล์มบางหลายชั้นของของไทเทเนียมไดออกไซด์ และซิลิกอน ไดออกไซด์นั้นเหมาะสมสำหรับการนำไปประยุกต์ใช้ในการเคลือบกันการสะท้อนและ ฟิลเตอร์



สาขาวิชาฟิสิกส์

ปีการศึกษา 2564

ลายมือชื่อนักศึกษา

ลายมือชื่ออาจารย์ที่ปรึกษา

EKACHAI CHONGSEREECHAROEN : PREPARATION AND CHARACTERIZATION OF
SPUTTERED METAL OXIDE MULTILAYER THIN FILMS FOR OPTICAL APPLICATION.
THESIS ADVISOR : ASSOC. PROF. PRAYOON SONGSIRIRITTHIGUL, Ph.D. 107 PP.

Keyword: Metal oxide thin films, Multilayer

Metal oxides are important role of the optical coating materials because of its tunable properties, excellent optical transparency, and chemical and environmental stability. Titanium dioxide and silicon dioxide are two well-known materials to produce the optical thin films. Titanium dioxide thin films were successfully fabricated via RF magnetron sputtering and reactive gas timing (RGT) sputtering. For RF magnetron sputter deposition, all samples exhibit a high transmittance ($> 85\%$) in visible region. The transmittance tended to decrease as the working pressure increased. Refractive index depends on working pressure. Mixing phase of Rutile and Anatase were found in all films corresponding to XANES results. The fitted plots of EXAFS data in the R-space show that the bond length of the lower working pressure sample is greater than that of higher.

By using RGT technique, TiO_2 thin films were fabricated with fixed working pressure and power. The oxygen flow timing was varied. The transmittance spectra from UV-vis measurement of the RGT samples are obviously different from the spectrum of uncoated glass slide. The maximum transmittance spectra obtained with shorter oxygen flow timings exhibit longer wavelengths compared to those obtained with longer flow timings. All of the investigated metal oxides lowered the optical transmittance of undeposited glass when applied as a single layer of TiO_2 and the transmittance is slightly sensitive to in the film structure. The normalized Ti K-edge XANES result in fluorescence mode at different oxygen timing sequence are reported. The characteristics in pre-edge and white line regions reveal the rutile-anatase phase mixture. Linear combination fitting of XANES data exhibits that weight of TiO_2 anatase and rutile depend on the oxygen flow timing which is good agreement between XANES and XRD results. Bond length between Ti – O and Ti - Ti were shown by EXAFS results.

$\text{TiO}_2+\text{SiO}_2$ multilayer thin films were fabricated. Transmittance of $\text{TiO}_2+\text{SiO}_2$ multilayer is different from SiO_2 single layer. XANES and EXAFS results are analyzed. In the visible area, the light transmittance of $\text{SiO}_2\text{-TiO}_2$ multilayer films was larger than that of a single layer TiO_2 film. The shorter oxygen flow duration results in a larger wavelength shift in the maximum transmittance spectrum. These multilayer thin films are suitable to be used for anti-reflection coating and filter applications.



School of Physics
Academic Year 2021

Student's Signature 
Advisor's Signature 

ACKNOWLEDGEMENTS

My thesis could not have been completed without the assistance and support from several people, to whom I would like to convey my sincere gratitude.

Firstly, I would like to express my profound gratitude to Prof. Dr. Rattikorn Yimnirun, my big boss and chairman of my thesis defense committee, for his valuable support, advice, very gentle patience and guidance in every steps. Moreover, not only his scientific support, but also his great perspective and trust were a great help and motivation throughout my study life.

I thank Assoc. Prof. Dr. Prayoon Songsiririthigul, my thesis advisor at Suranaree University of Technology. He gives really valuable perspectives, advice, suggestions, and support for my graduation.

I would like to also thank Assoc. Prof. Dr. Saroj Rujirawat for supporting and suggesting me in scientific aspects and for accepting me to be a member of his group.

I would like to express my grateful to Dr. Narong Chanlek for his valuable assistance, push and pull motivation and suggestion in this research work.

I am also grateful to Dr. Mati Horprathum at NECTEC for the professional supports and suggestion in this research.

I thank all staff at Beamline 3.2 and Beamline 5.3, Synchrotron Light Research Institute (SLRI), everybody in our characterization group, school of physics, Suranaree University of Technology (SUT).

Special thanks to Miss Jenjira Tanamai for her love and encouragement.

It is impossible to name all who was a great help during my Ph.D. study, for the wonderful times we shared.

Finally, I would like to express appreciation to my family, my parents and my older brothers for their love and everything in my life.

Ekachai Chongsereechoen

CONTENTS

	Page
ABSTRACT IN THAI.....	I
ABSTRACT IN ENGLISH.....	III
ACKNOWLEDGEMENTS	V
CONTENTS	VI
LIST OF TABLES	VIII
LIST OF FIGURES	IX
LIST OF ABBREVIATIONS	XV
CHAPTER	
I INTRODUCTION	1
1.1 Background	1
1.2 Objectives and structure of this thesis.....	3
1.3 Scope and limitations.....	3
II LITERATURE REVIEW	4
2.1 Metal Oxide Thin Films	4
2.1.1 Silicon Dioxide Thin Film	4
2.1.2 Titanium Dioxide Thin Film	12
2.1.3 Other Metal Oxide Thin Film.....	19
2.2 Thin Films for Optical Applications.....	22
2.2.1 Interference in thin films	22
2.2.2 Multilayer thin films.....	23
2.2.3 Anti - Reflective Coating	27
2.2.4 High Reflection Coating.....	28

CONTENTS (Continued)

	Page
III EXPERIMENTAL AND TECHNIQUES	35
3.1 Thin films preparation	35
3.1.1 RF Magnetron Sputter Deposition.....	35
3.1.2 Reactive Gas Timing Sputter Deposition.....	38
3.2 Thin films characterization techniques	40
3.2.1 X-ray diffraction (XRD)	40
3.2.2 Scanning electron microscopy (SEM)	42
3.2.3 X-ray Absorptions Spectroscopy (XAS).....	44
3.2.4 UV-Vis-NIR spectroscopy	47
3.2.5 Spectroscopic ellipsometry.....	48
IV RESULTS AND DISCUSSION	51
4.1 TiO ₂ thin films prepared by RF magnetron sputtering.....	51
4.2 TiO ₂ thin films fabricated by Reactive Gas Timing (RGT) magnetron sputtering	61
4.3 SiO ₂ films fabricated by custom-built RF magnetron sputtering	76
4.4 TiO ₂ +SiO ₂ Multilayer Thin Films.....	82
V CONCLUSION	90
REFERENCES	92
APPENDIX	103
CURRICULUM VITAE	106

LIST OF TABLES

Table	Page
2.1 Deposition parameters.....	6
2.2 Roughness values (Ra and rms) of the SiO _x films obtained by AFM, their thickness and density obtained by XRR).....	7
2.3 Grain size (D), average surface roughness (R _{ave}) and thickness calculated with the Sanepoel method of samples produced at various O ₂ /Ar + O ₂ ratios	17
2.4 Light transmittance, refractive indices and thickness values of single layer films and light transmittance values of multilayer films	21
3.1 Sputtering yields by 500 eV ions	34
4.1 Thickness of TiO ₂ thin films prepared by RF magnetron sputtering at different working pressure.....	57
4.2 Weight of TiO ₂ Anatase and Rutile in TiO ₂ thin films with different oxygen flow timing and R-factor obtained from the linear combination fitting of XANES data.....	71
4.3 EXAFS-derived structural parameters for TiO ₂ thin films.....	74

LIST OF FIGURES

Figure	Page
2.1 Chemical Structure Model of silicon dioxide	5
2.2 Surface morphology of the films deposited at different process pressures (a) 0.27 Pa, (b) 0.53 Pa, (c) 0.80 Pa, (d) 1.33 Pa.....	7
2.3 High-resolution Si 2p XPS spectra measured at the film surface referenced to C 1s at 284.8 eV	8
2.4 Refractive index of the films a as a function of the optical wavelength for samples S2, S4, S6 and S10, and b at 632.8 nm as a function of film density	9
2.5 Optical transmittance of the glass substrate and systems glass/film.....	10
2.6 Sputtering rate with added oxygen to that without oxygen for 1 mm film thickness deposited at 8×10^{-2} Pa as a function of oxygen partial pressure	10
2.7 The surface roughness (nm) and deposition rate (nm /min) (Left) vs. substrate temperature (K) (Right) vs. argon gas flow (sccm).....	11
2.8 The primitive cells of rutile, brookite and anatase.....	12
2.9 Surface morphologies of the TiO ₂ films with different post-annealing temperature: (a) as-grown film, (b) film post-annealed at 550 °C, and (c) at 900 °C. (d) XRD patterns of the as-grown film and films post-annealed at 550 °C and 900 °C.....	14
2.10 Optical transmission spectra of TiO ₂ polymorph films	15
2.11 Plot of refractive index versus wavelength for as-deposited and annealed TiO ₂ thin films.....	16
2.12 XRD patterns of various samples produced at different O ₂ /Ar + O ₂ ratios.....	17
2.13 Optical transmittance spectra of various samples produced at different O ₂ / Ar+ O ₂ ratios.....	17
2.14 Ti2p (a) and O1s (b) XPS spectra of TiO ₂ thin films	18
2.15 Effect of hot-isostatic pressing and annealing treatment on optical constants of HfO ₂ and Ta ₂ O ₅ films.....	20

LIST OF FIGURES (Continued)

Figure	Page
2.16 % light transmittance spectra of single layer films.....	22
2.17 Light paths through a thin film on glass.....	23
2.18 Schematic of a multilayer thin films.....	24
2.19 Schematics of (a) hydrophobic and (b) hydrophilic surfaces of the SiO ₂ film. The R represents alkoxy group remained after sintering on the SiO ₂ film surface. TiO ₂ coating solution was applied to the SiO ₂ film surfaces to fab- ricate the multilayer structure	26
2.20 Examples of FE-SEM images of the 2nd TiO ₂ 250nm film surfaces for (a) clear, (b) cracks, and (c) delamination morphologies. The inserted contact angles were measured on the 1st SiO ₂ films before deposition of the 2nd TiO ₂ film	26
2.21 Propagation of light rays through a single layer film on substrate ($n_s > n$)	27
2.22 Schematic representation of a metal multi-dielectric mirror	28
2.23 Reflectance spectra of one-, three-, five- and seven-DBR stacks with their optical images.....	29
2.24 (Left) Schematic of a multilayer structure (Right) A FIB image (SEM) of a multilayer structure	30
2.25 Optical constants (n and k) measured for (a) TiO ₂ and (b) SiO ₂ films.....	31
2.26 UV-Vis-NIR reflectance spectra from calculations and experimental measurement at the quarter wave condition	32
3.1 Some calculated sputtering yields.....	35
3.2 Sputtering yield as a function of angle-of-incidence of the bombarding ion	36
3.3 Schematic diagram of mechanism of magnetron sputter coating machine.....	37
3.4 RF magnetron sputtering system at BL6, SLRI	38

LIST OF FIGURES (Continued)

Figure	Page
3.5 Schematic representation of argon and oxygen mass flow rate versus time used for depositing TaO thin film by the conventional reactive sputtering and RGT techniques.....	39
3.6 Reactive Gas Timing magnetron sputtering system at NECTEC.....	40
3.7 Schematic representation of Bragg's Law for XRD.....	41
3.8 XRD (BRUKER, D8 ADVANCE) at SUT.....	42
3.9 Schematic diagram of (a) basic SEM components and (b) different types of SEM signals	43
3.10 SEM machine (Zeiss AURIGA FE-SEM/FIB/EDX) located at SUT	43
3.11 The principle for XAS spectra	44
3.12 Theoretical and algorithm for XANES and EXAFS spectra	45
3.13 Energy range of (a) XANES and EXAFS spectra (b) K-space spectra and (c) R-space spectra	46
3.14 SUT-NANOTEC-SLRI beamline setup (BL5.2), SLRI.....	47
3.15 UV-vis spectrophotometer at SUT	48
3.16 Configuration in spectroscopic ellipsometry for a determined incidence angle (θ , degrees). The changes of amplitude (Ψ , degrees) and phase (Δ , degrees) of the reflected elliptically polarized light are measured by the detector.....	49
3.17 Schematic diagram of a polarizer-sample-rotating analyzer ellipsometer	50
4.1 XRD results of the titanium oxide thin films with different power	52
4.2 SEM (left) and AFM (right) images of the titanium oxide thin films with different working pressure.....	54
4.3 Optical transmittance of the titanium oxide thin films deposited on glass with different working pressure.....	56
4.4 Refractive index in the 250–1650 nm wavelength range for the titanium oxide thin films with different working pressure	57

LIST OF FIGURES (Continued)

Figure	Page
4.5 XANES spectra of the titanium oxide thin films with different working pressure compared with the standard spectra of Ti foil, rutile and anatase TiO ₂	59
4.6 EXAFS spectra fitted using ARTEMIS in R-space of the titanium oxide thin films with working pressure of 2.2 and 12.4 Pa.....	60
4.7 Cross-sectional and Top-view SEM images of the titanium oxide thin films with oxygen flow timing.	63
4.8 Optical transmittance of the titanium oxide thin films with different oxygen flow timing.....	66
4.9 XRD results of the titanium oxide thin films with oxygen flow timing.....	67
4.10 Raman results of the Titanium Oxide thin films with different oxygen timing sequence.	68
4.11 The normalized Ti K-edge XANES spectra of TiO ₂ thin films prepared by conventional reactive and RGT technique at different oxygen flow timing (the enlarged view of spectra in pre-edge region showed in inset).....	69
4.12 Ti K-edge EXAFS (weighted by k ²) from experiment (blue line) and fitting (red circle) of TiO ₂ thin films prepared by conventional reactive and RGT technique at different oxygen flow timing. Model fits to the experimental filtered EXAFS in the k-space are also shown (insets)	72
4.13 View of entire sputtering system (In the rack, A = Turbopump Controller, B = RF Power Supply (600 W) and C = Matching Box.	77
4.14 Transmittance of the Silicon Oxide thin films prepared by custom-built RF magnetron sputtering with different sputtering pressure	78
4.15 Transmittance of the Silicon Oxide thin films with different sputtering power.....	78
4.16 XRD Spectrum of the Silicon Oxide thin films deposited at 50W, 0.8 Pa for 90 min.	79

LIST OF FIGURES (Continued)

Figure	Page
4.17 SEM micrographs of the Silicon Oxide thin films deposited at 100 and 150 W.....	80
4.18 SEM micrographs of the Silicon Oxide thin films with different sputtering pressure.....	80
4.19 SEM micrographs of the Silicon Oxide thin films with different sputtering time.....	81
4.20 Cross- section SEM micrograph of the Silicon Oxide thin films deposited on Si wafer shows the thickness of 100 nm	82
4.21 Optical transmittance of Silicon Oxide layers deposited on glass substrates with different deposition time	83
4.22 Transmittance of 15 min Silicon Oxide layers deposited on various TiO ₂ films.	83
4.23 Transmittance of 30 min Silicon Oxide layers deposited on various TiO ₂ films.	84
4.24 Transmittance of 45 min Silicon Oxide layers deposited on various TiO ₂ films.	84
4.25 Transmittance of 60 min Silicon Oxide layers deposited on various TiO ₂ films.	85
4.26 Optical transmittance of various deposition time Silicon Oxide layers deposited on various TiO ₂ films.....	86
4.27 The normalized Si K-edge XANES spectra of Silicon Oxide layers with different deposition time compared with SiO ₂ powder standard.	87
4.28 The normalized Si K-edge XANES spectra of 60 min Silicon Oxide layers deposited on various TiO ₂ films.....	87
4.29 The normalized Si K-edge XANES spectra of different deposition time SiO ₂ layer coated on TiO ₂ films prepared by conventional reactive sputtering	88
4.30 Si K-edge EXAFS (weighted by k^2) from experiment (black line) and fitting (red circle) of SiO ₂ layers coated on TiO ₂ films prepared by conventional reactive and RGT sputter technique at different oxygen flow timing	89

LIST OF ABBREVIATIONS

°C	Degree Celsius
Å	Angstrom
BL5.2	Beamline 5.2
EXAFS	Extended X-ray Absorption Fine Structure
E ₀	Absorption edge
E _B	Binding Energy
eV	Electron-Volt
GIXRD	Grating Incident X-ray Diffraction
h	Plank's Constant
I _e	Electron Current
I _p	Photon Current
LCF	Linear Combination Fitting
RGT	Reactive Gas-Timing
SEM	Scanning Electron Microstructure
SLRI	Synchrotron Light Research Institute
UV	Ultraviolet
VIS	Visible
XANES	X-ray Absorption Near Edge Structure
XAS	X-ray Absorption Spectroscopy
XRD	X-ray Diffraction
λ	Wavelength
σ ²	Debye-Waller factor
S ₀ ²	Scale Factor

CHAPTER I

INTRODUCTION

1.1 Background

Multilayer optical thin films have been coated on substrate in order to obtain desired reflectance and transmittance of specific wavelength of light and have wide range of applications such as anti-reflection coatings, high reflection coating, highly reflecting laser mirrors, dichroic mirrors, various kinds of optical filters, beam splitters, heat reflectors, solar cell covers and thin-film polarizers. Multilayer optical coatings are used to modify the interaction of light with a surface by utilizing the interference of reflections from multiple interfaces. The performance of an optical coating is highly sensitive to any variations of layer refractive indices and thickness. Accurate control of film parameters, thickness, composition uniformity and roughness, is necessary to accomplish the designed particular function of the coating stack (Hilfiker *et al.*, 2019). It is important to know the thickness, optical and absorption properties of individual layer as a function of wavelength to predict the behavior of modern optoelectronic and optical devices (Sultan *et al.*, 2015).

Metal oxide is an important role of the optical coating materials because of its tunable properties, excellent optical transparency, and chemical and environmental stability (Park *et al.*, 2017). Common metal oxide coating materials are SiO_2 , TiO_2 , Al_2O_3 , ZnO , Nb_2O_5 , HfO_2 and Ta_2O_5 . Silicon dioxide (SiO_2) and titanium dioxide (TiO_2) are famous coating materials due to their excellent properties and producibility. Titanium dioxide films are widely used in various fields of applications, for example, gas sensors, photocatalysis, solar cells, optical devices, etc. They have high optical transmittance with high refractive index in the visible range, outstanding chemical stability, high photocatalytic activity, satisfied mechanical hardness and non-toxicity (Pjević *et al.*, 2015).

Silicon dioxide is an inexpensive optical coating material with low refractive index, high transmittance from the ultraviolet (UV) to near infrared (NIR) region, good insulation and chemical and mechanical properties. It is widely used in optical multilayer films when coupling with a high refractive index material (Wang *et al.*, 2018). In addition, SiO₂ films are a key part of gate dielectrics in semiconductor industry because of their high resistivity, superb dielectric strength, large band gap, high melting point, and native, low defect density interface with Si (Šimurka *et al.*, 2018). Hence, these are the reason that TiO₂ and SiO₂ films are suitable candidates for many optical applications.

Up to now, many methods such as electron beam evaporation, ion assisted deposition, ion beam sputtering, magnetron sputtering, sol-gel, evaporation, chemical vapour deposition, and so on are used to prepare TiO₂ and SiO₂ thin films on various types of substrates. Among these methods radio frequency (RF) magnetron sputter deposition has many benefits, for instance, excellent control of film quality and thickness over large deposition areas, good adhesion, density and uniformity (Braeuer *et al.*, 2010). Therefore, rf magnetron sputtering has become an interesting technique for the preparation of controllable metal oxide films at low substrate temperatures (Jeong *et al.*, 2004). Basically, the film thickness is adjusted by controlling the deposition rate and time. In order to control the refractive index of the optical films a method that has been proposed is varying the porosity of thin films. However, film porosity is not easy to reproduce, especially when using different experimental or industrial setups. Thus, control of composition is a more reliable possibility to tailor the film refractive index (Gracia *et al.*, 2006).

In this work, the preparation of metal oxide single layer thin films with desired optical and structural properties for optical applications by using RF magnetron sputtering is studied and the various analytical techniques including synchrotron-based characterization methods are extensively used to characterize the prepared films. SiO₂ and TiO₂ are two main focused metal oxide materials in this study and thin film multilayer of these two materials is designed and fabricated.

1.2 Objectives and structure of this thesis

In this work, the preparation of metal oxide single layer thin films with desired optical and structural properties by using RF magnetron sputter deposition is studied. The various analytical techniques including synchrotron-based characterization methods are extensively used to characterize the prepared films. Thin film multilayer of two kinds of material is designed and fabricated. The research objectives are described below.

- To prepare the metal oxide single layer thin films by RF magnetron sputtering on glass substrate with controllable refractive index and film thickness.
- To investigate the optical and structural properties of prepared films.
- To study the relationship between the preparation conditions and film properties especially refractive index and film thickness.
- To design and fabricate thin film multilayer with two kinds of material.

1.3 Scope and limitations

- RF magnetron sputtering is the deposition technique of metal oxide thin films for this work.
- SiO_2 and TiO_2 are two main focus materials for metal oxide single layer thin film.
- Optical properties of metal oxide thin films will be investigated by UV-Vis-NIR spectrophotometer and spectroscopic ellipsometer.
- The film properties will be characterized by X-ray diffraction (XRD), scanning Electron Microscopy (SEM), Atomic Force Microscopy (AFM), X-ray Photoelectron Spectroscopy (XPS), X-ray absorption spectroscopy (XAS).
- The effects of deposition parameters on the optical and properties of thin films will be focused.

CHAPTER II

LITERATURE REVIEW

In order to achieve the metal oxide thin film multilayer with desired properties for this work, a basic understanding of sputtering technology, metal oxide thin films, and thin films for optical applications are required. Additional background information is provided relating to the structural and optical characterizations of thin films. This information gives an overview of the fundamental knowledge for this study.

2.1 Metal Oxide Thin Films

Metal oxides play a significant role in many areas of physics, chemistry and materials science. The metal elements are able to form a large diversity of oxide compounds. Metal oxides have been widely used in optical applications because of its tunable properties, excellent optical transparency, and chemical and environmental stability (Park *et al.*, 2017). Common metal oxide coating materials are SiO_2 , TiO_2 , Al_2O_3 , Nb_2O_5 , HfO_2 and Ta_2O_5 . Silicon dioxide (SiO_2) and titanium dioxide (TiO_2) are the famous coating materials due to their excellent properties and mass production ability.

2.1.1 Silicon Dioxide Thin Film

Silicon dioxide, also known as silica and its chemical formula is SiO_2 , is a main compound extensively found in quartz and sand. Its atomic weight is 60.08 g/mol. Silicon dioxide is an oxide formed by Si^{+4} and O^{2-} . The compound is mostly found in the crystalline form by a cation Si central, coordinated to 4 anion O, so that the structure of silica has a tetrahedral geometry. It also exists in amorphous solid or other crystalline forms as rhombohedral, hexagonal, cubic, nonclinical or orthorhombic geometry. The chemical structure model of silicon dioxide can be shown as the below figure. It is transparent to gray, odorless, crystalline or amorphous solid, and insoluble in water and acid. Its melting and boiling point are 1600 °C and 2230 °C, respectively.

It has energy bandgap of 8.9 eV approximately. Its density is 2.65 g m/L. For the chemical properties, silicon dioxide is not very reactive compound since the polarity of molecule is zero. The Si forms two double bonds with the oxygen, so it is extremely stable.

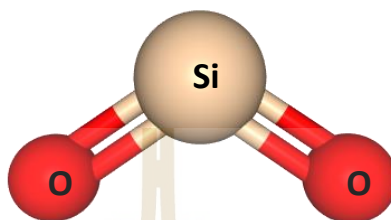


Figure 2.1 Chemical Structure Model of silicon dioxide. (Adapted from <https://pubchem.ncbi.nlm.nih.gov/compound/24261>).

For using as coating material, silicon dioxide has an inexpensive price, low refractive index, high transmittance from the ultraviolet (UV) to near infrared (NIR) region, good insulation and chemical and mechanical properties. Coupling of silicon dioxide layer with a high refractive index material can be done for making optical multilayer films (Wang *et al.*, 2018). In addition, SiO₂ films are an important part in semiconductor industry due to their high resistivity, good dielectric strength, large band gap, high melting point, and native, low defect density interface with Si (Šimurka *et al.*, 2018). SiO₂ band gap with the value of 8.9±0.1 eV were shown in Seguni's paper. There are several methods to produce silicon dioxide thin films, for example, DC and RF magnetron sputtering (Lee *et al.*, 2006 and Jeong *et al.*, 2004), ion beam sputtering (Wang *et al.*, 2018), electrospinning (Raut *et al.*, 2013), sol-gel (Dou *et al.*, 2016), dip-coating (Chi *et al.*, 2011).

Šimurka studied the optical and mechanical properties of amorphous SiO₂ thin films deposited on soda-lime silicate float glass by reactive RF magnetron sputtering at room temperature. The sputtering chamber was evacuated to a base pressure lower than 1.2×10⁻⁴ Pa before starting the deposition.

Moreover, in order to clean the surface of the silicon target before each deposition, 5 min of pre-sputtering was performed. The magnetron power remained

the same at 300 W during reactive sputtering. The deposition parameters of each sample are shown in Table 2.1. The dependence of the process pressure on the properties was examined. The film densities are strongly influenced by the process pressure and shift between 2.38 and 1.91 g/cm³ as the pressure changes from 0.27 to 1.33 Pa.

Table 2.1 Deposition parameters (Šimurka *et al.*, 2018).

Sample	Pressure		Argon	Oxygen	Deposition rate
	(mTorr)	(Pa)	(sccm ^a)	(sccm ^a)	(nm.min ⁻¹)
S2	2	0.23	18.7	2.4	8.3
S4	4	0.53	18.7	2.3	11.3
S6	6	0.80	18.7	2.3	12.4
S10	10	1.33	18.7	2.3	10.1

^aStandard cubic centimeters per minute

Figure 2.2 shows the evolution of surface morphology with increasing process pressure. As can be seen, the arithmetic and root mean square roughness (Ra and rms) increase significantly with increasing process pressure. On the other hand, density exhibits opposite trend and decreases with the pressure from 2.38 to 1.91 g cm⁻³ (Table 2.2).

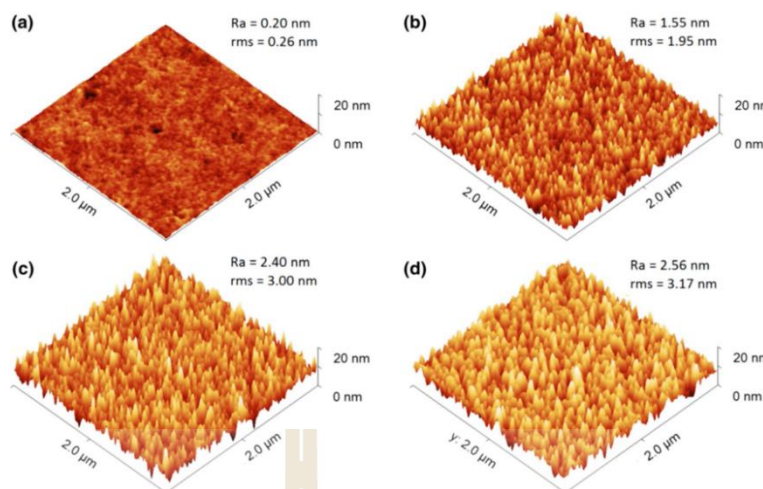


Figure 2.2 Surface morphology of the films deposited at different process pressures (a) 0.27 Pa, (b) 0.53 Pa, (c) 0.80 Pa, (d) 1.33 Pa (Šimurka *et al.*, 2018).

Table 2.2 Roughness values (R_a and rms) of the SiO_x films obtained by AFM, their thickness and density obtained by XRR (Šimurka *et al.*, 2018).

Sample	Pressure(Pa)	$R_a(nm)$	$rms(nm)$	Thickness(nm)	Density($g.cm^{-3}$)
S2	0.27	0.20	0.26	269	2.38 ± 0.01
S4	0.53	1.55	1.95	327	2.16 ± 0.01
S6	0.80	2.40	3.00	298	1.98 ± 0.05
S10	1.33	2.56	3.17	192	1.91 ± 0.01

Figure 2.3 shows the Si 2p XPS spectra measured at the film surface referenced to C 1s at 284.8 eV. The result revealed a stable position of Si 2p (~ 103.2 eV) typical for stoichiometric O/Si = 2.0 ratio for films prepared at the pressure ranging from 0.53 to 1.33 Pa. For the sample S2 deposited at the lowest pressure of 0.27 Pa, the Si 2p peak shifts to lower binding energy (103.0 eV) with substoichiometric O/Si = 1.8 ratio. Shift to the lower binding energies indicates the presence of suboxide structure suggesting

that the oxygen flow was not sufficient to fully oxidize the sputtered silicon resulting in $\text{SiO}_{1.8}$ thin film.

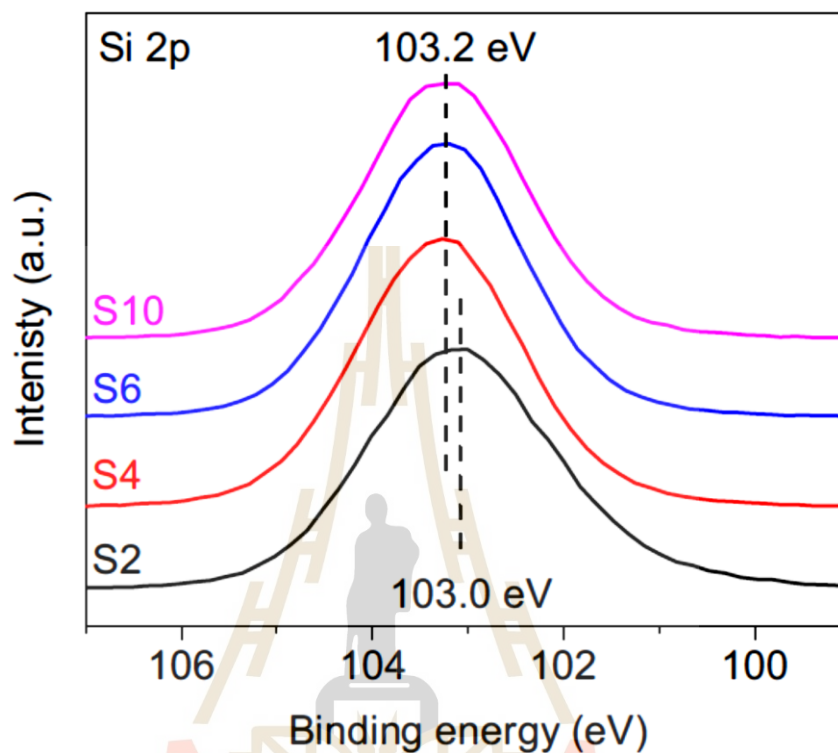


Figure 2.3 High-resolution Si 2p XPS spectra measured at the film surface referenced to C 1s at 284.8 eV (Šimurka *et al.*, 2018).

For the optical properties Figure 2.4 shows the refractive index of the prepared films. As can be seen, the refractive index decreases with the increasing process pressure in the whole spectral range. Figure 4b illustrates the development of refractive index with the film density at the wavelength of 632.8 nm. The refractive indices of the films vary between 1.37 and 1.52 when density increases from 1.91 to 2.38 g/cm³. All the films exhibit high transparency and do not significantly vary from the transparency of the glass substrate (Figure 4). Only approximately 1.3% lower transmittance in the visible light region was observed for the sample S2 deposited at the lowest process pressure (Figure 2.5). This decrease in transmittance can be attributed to the suboxide structure detected by XPS.

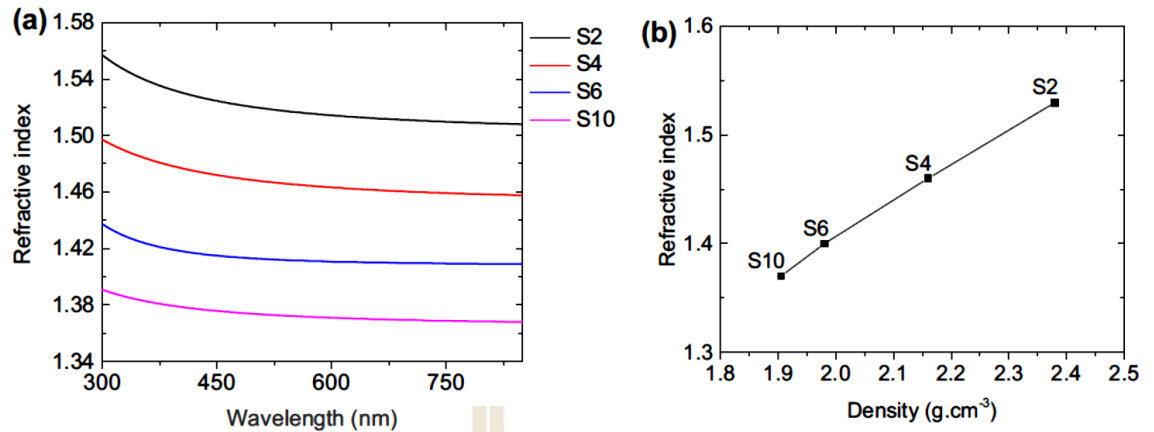


Figure 2.4 Refractive index of the films a as a function of the optical wavelength for samples S2, S4, S6 and S10, and b at 632.8 nm as a function of film density (Šimurka *et al.*, 2018).

Fujiyama *et al.* studied the effect of O₂ partial pressure on the mechanical properties of SiO₂ films deposited by rf magnetron sputtering using SiO₂ target with a purity of 99.99%. Figure 2.6 indicates the deposition rate of SiO₂ films as a function of the O₂ partial pressure, where the flow rate of argon gas is 10 cm³/min. The deposition rate clearly decreases by 35% due to the addition of the O₂ gas into the argon atmosphere. In addition, the rate is independent on the existence of O₂ partial pressure. The composition of sputtered SiO₂ films in pure argon gas is deficient in oxygen compared to that for bulk SiO₂, but it is close to that of bulk SiO₂ when oxygen gas with a pressure of above about 2×10⁻² Pa is added.

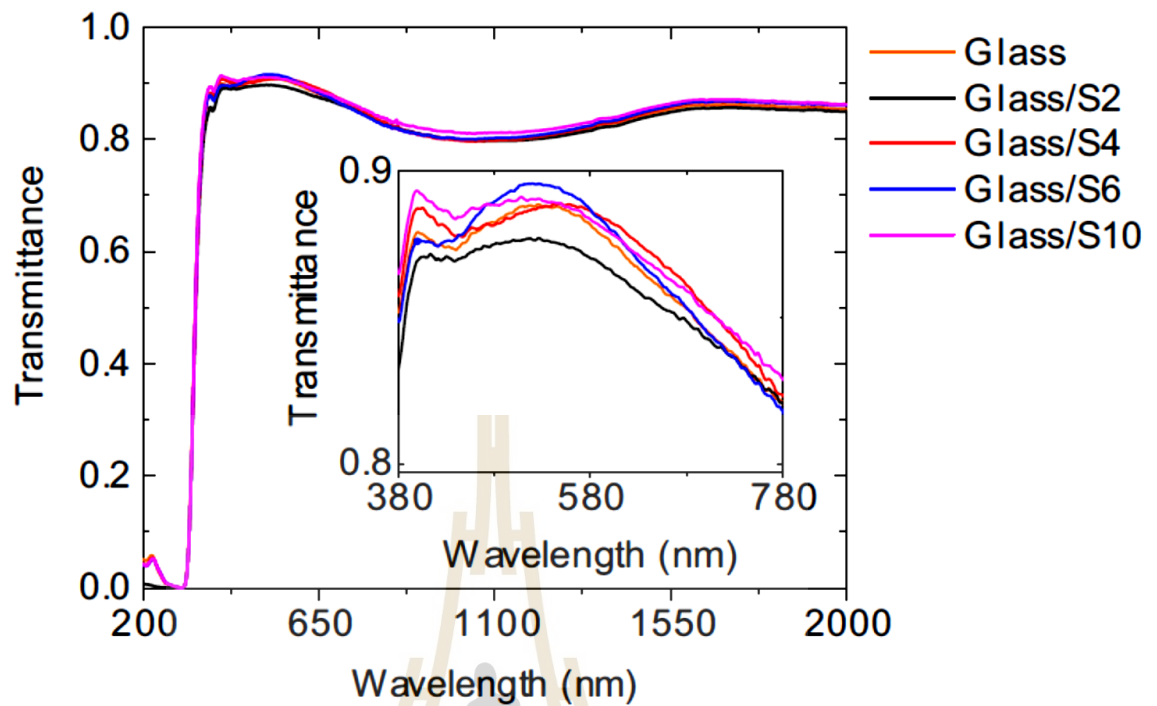


Figure 2.5 Optical transmittance of the glass substrate and systems glass/film (Šimurka *et al.*, 2018).

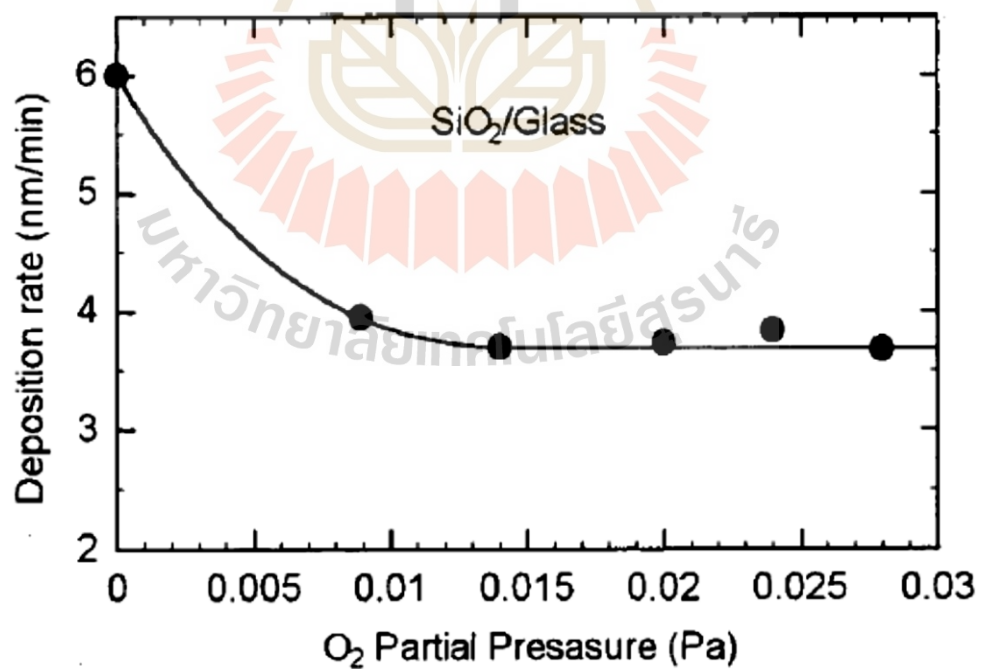


Figure 2.6 Sputtering rate with added oxygen to that without oxygen for 1 mm film thickness deposited at 8×10^{-2} Pa as a function of oxygen partial pressure (Fujiyama *et al.*, 2002).

Table 1. The density, thickness and root-mean-square surface roughness of the deposited SiO₂ layer for samples A1, A2, A3 and A4 ascertained from XRR

Sample	Density (g cm ⁻³)	Thickness (nm)	Roughness (nm)
A1	2.35	75.32	1.16
A2	2.34	75.82	0.84
A3	2.35	81.39	0.80
A4	2.33	79.90	0.67

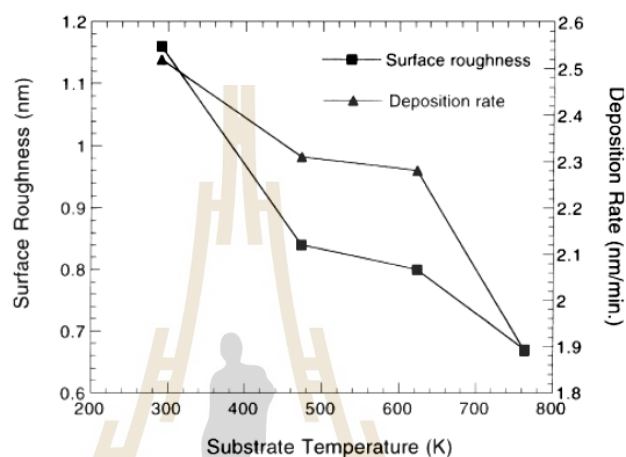


Table 2. The density, thickness and root-mean-square surface roughness of the deposited SiO₂ layer for samples B1, B2, B3 and B4 ascertained from XRR

Sample	Density (g cm ⁻³)	Thickness (nm)	Roughness (nm)
B1	2.28	49.77	0.51
B2	2.32	67.22	0.70
B3	2.26	70.18	1.51
B4	2.37	70.83	2.38

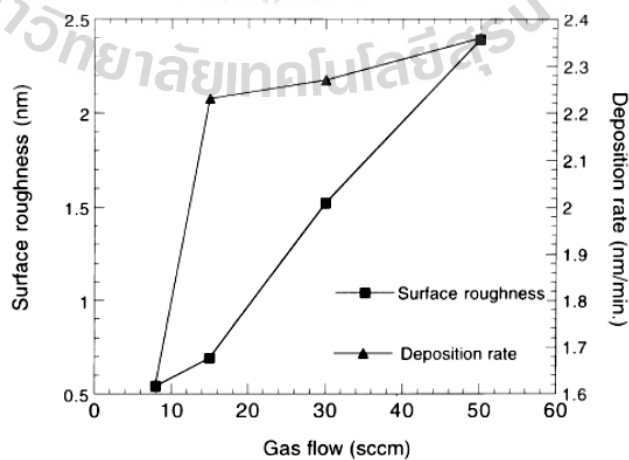


Figure 2.7 The surface roughness (nm) and deposition rate (nm /min) (Left) vs. substrate temperature (K) (Right) vs. argon gas flow (sccm) (Kojima *et al.*, 1999).

Kojima *et al.* studied grazing-incidence XRR characterization of as-grown SiO₂ thin films deposited on Si(100) substrates by rf magnetron sputtering with various substrate temperatures and gas flow rates. The results show that an increase of substrate temperature from room temperature to 763 K only slightly decreases the surface roughness (Figure 2.7). Comparatively, the surface morphology is strongly controlled by the gas flow conditions during deposition. The surface roughness increases almost linearly from 0.51 to 2.38 nm when the argon flow rate is increased from 8 to 50 sccm (Figure 7). The XPS results confirm that it is possible to prepare high-quality SiO₂ thin films by the sputtering method.

2.1.2 Titanium Dioxide Thin Film

Titanium dioxide (TiO₂) usually occurs in amorphous form and also in three crystalline polymorphs: anatase, rutile and brookite. The most abundant and most extensively studied polymorph is the rutile phase. Anatase and rutile phases are tetragonal in nature while brookite exhibits an orthorhombic structure (Figure 2.8) (Esch *et al.*, 2014).

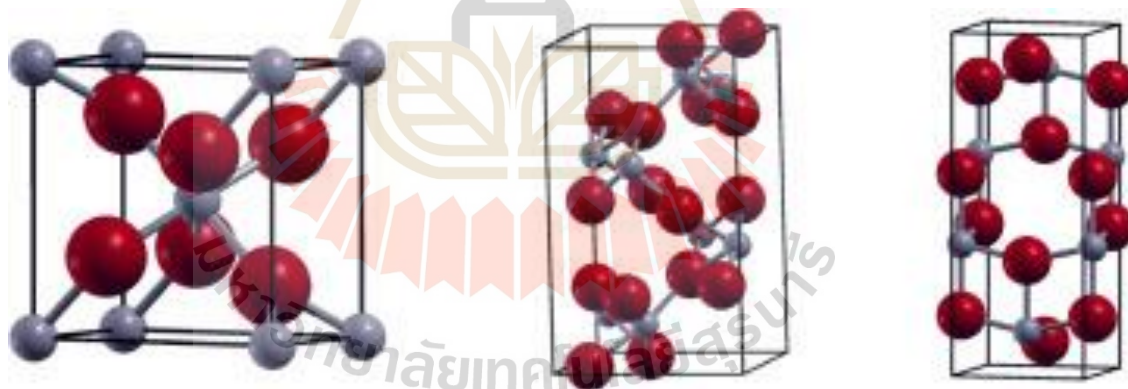


Figure 2.8 The primitive cells of rutile, brookite and anatase (from left to right, Esch *et al.*, 2014).

TiO₂ has melting and boiling points of 1840 °C and 2900 °C, respectively. For physical properties, titanium dioxide is an odorless and tasteless white crystalline powder. The bulk density of rutile phase is 4.13 g/cm³. It has a band gap of 3.0 eV (Zhang *et al.*, 2014). The rutile structure is very compact and thermodynamically most stable phase at all temperatures, and has higher refractive index than anatase (2.7 vs 2.52, at 550 nm wavelength). Rutile phase exhibits better optical activity than anatase

and is used for antireflective and dielectric applications (Nair *et al.*, 2014). Moreover, the rutile is widely used as a white pigment material due to good scattering effect that protects material from ultraviolet radiations (Nair *et al.*, 2011).

Titanium dioxide thin films are used in a wide range of applications, such as gas sensors, photocatalysis, solar cells, optical devices, etc. They have high optical transmittance with high refractive index in the visible range, outstanding chemical stability, high photocatalytic activity, good mechanical hardness and non-toxicity (Pjević *et al.*, 2015). Different techniques can be used to fabricate TiO₂ films, for example, DC and RF magnetron sputtering, chemical vapor deposition (CVD), Pulsed laser deposition (PLD), hydrothermal method and Sol-Gel (Wang *et al.*, 2017).

Kang *et al.* study the effect of crystallization in TiO₂ thin films on optical properties characterized by transmittance measurements using UV-VIS spectrophotometry. TiO₂ thin films with amorphous and anatase phases were prepared using an RF sputtering and a TiO₂ (99.99%) target with a 5-cm diameter. Deposition process was performed at an RF power of 120 W. The TiO₂ films were deposited on quartz substrates at room temperature for 120 min. The distance between the target and substrate was 10 cm and the sputtering gas was Ar (20 sccm). The base pressure of the chamber was less than 6.67×10^{-3} Pa, and the working pressure was approximately 1.33×10^{-1} Pa.

Amorphous and anatase TiO₂ films were obtained by post-annealing in a tubular furnace at temperatures of 550 °C for 120 min in air. Figure 2.9(a) – (c) show the surface morphologies of the TiO₂ films with post-annealing. The grain growth indicating crystallization occurred when the film was postannealed at 550 °C, and the morphology with dense surface and no grain was obtained in the film post-annealed at 900 °C. Figure 2.9(d) shows the XRD pattern of the as-grown TiO₂ film and TiO₂ films post-annealed at 550 and 900 °C.

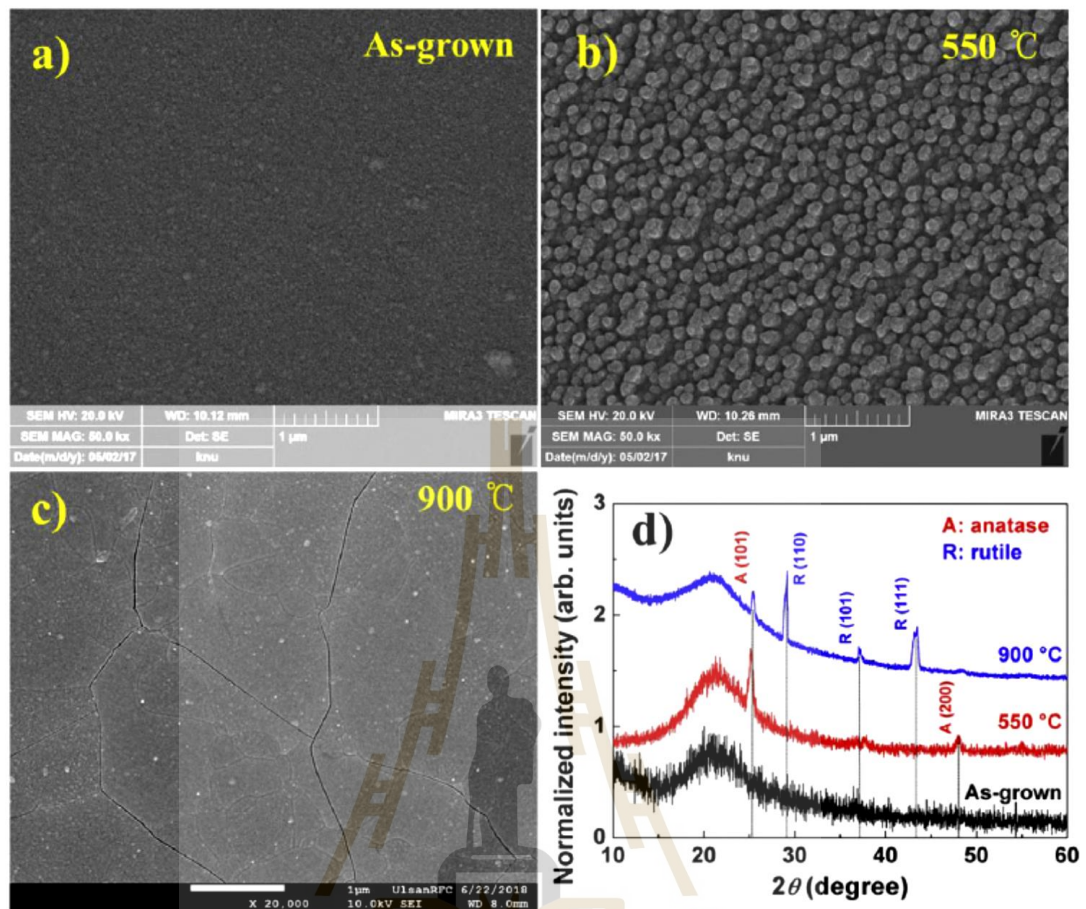


Figure 2.9 Surface morphologies of the TiO₂ films with different post-annealing temperature: (a) as-grown film, (b) film post-annealed at 550 °C, and (c) at 900 °C. (d) XRD patterns of the as-grown film and films post-annealed at 550 °C and 900 °C (Kang *et al.*, 2018).

The optical transmission spectra of the TiO₂ polymorph films were shown in Figure 2.10. The films have a high transmittance of $\sim 80\%$, and the fundamental absorption edge at a wavelength of approximately 360 nm. The absorption edge shifts slightly toward longer wavelengths with increasing post-annealing temperature (Figure 10 inset). This results from the crystallization because of the post-annealing. Additionally, the optical constant spectra of the films showed a gradual change above 3.5 eV.

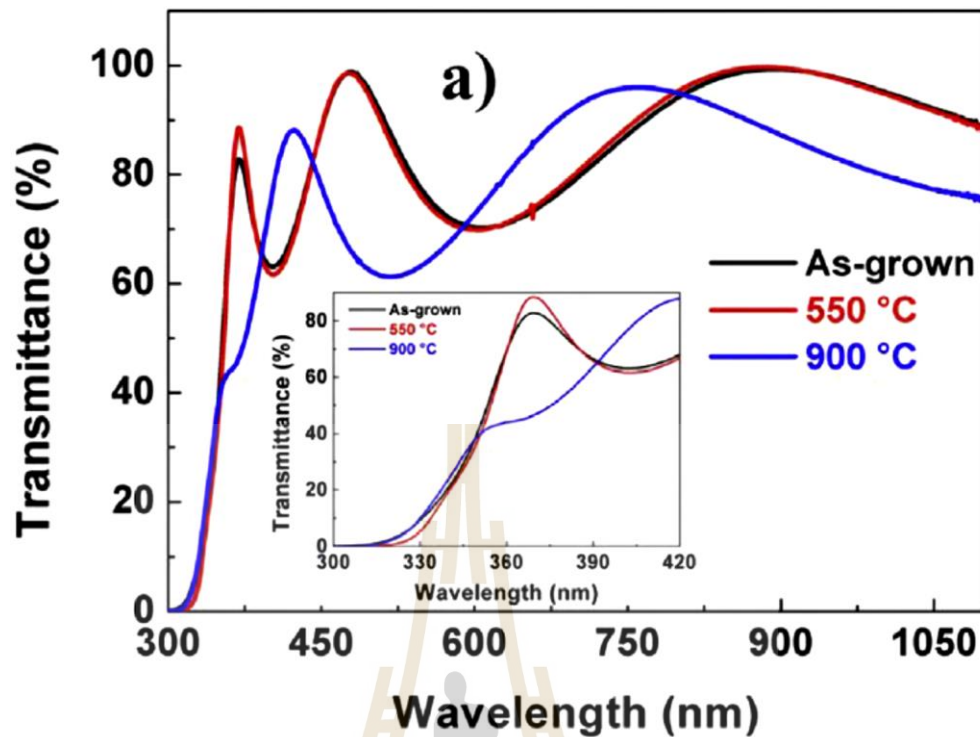


Figure 2.10 Optical transmission spectra of TiO_2 polymorph films (Kang *et al.*, 2018).

Nair *et al.* studied the optical parameters induced by phase transformation in RF magnetron sputtered TiO_2 thin films which were deposited onto quartz substrates using a ceramic TiO_2 target at a pressure of 0.01 mbar, a power of 300W and a substrate temperature of 573 K. Thermal annealing to the prepared film for 2 h at 873 K in air produced the formation of anatase phase, and a phase transformation to rutile with rod-like surface morphology was observed at 1073 K. The refractive index increased with increase in annealing temperature (Figure 2.11) because rutile is the optically active phase.

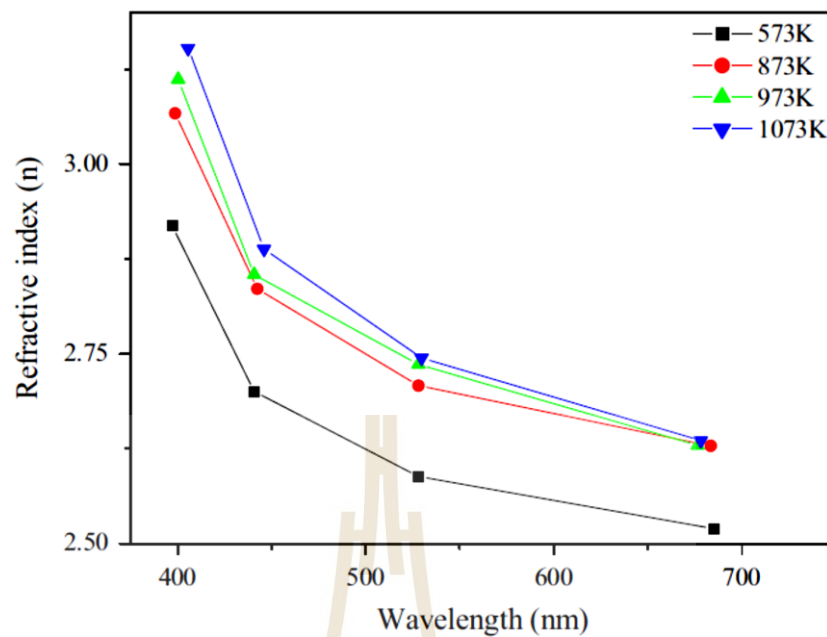


Figure 2.11 Plot of refractive index versus wavelength for as-deposited and annealed TiO_2 thin films (Nair *et al.*, 2014).

Grayeli Korpi *et al.* reported influence of the oxygen partial pressure on the growth and optical properties of RF-sputtered anatase TiO_2 thin films. Titanium dioxide films with thicknesses around 300 nm were deposited on glass substrates by reactive RF magnetron sputtering using a pure TiO_2 target at constant RF sputtering power (200 W), high working pressure (5×10^{-3} Torr) and room temperature. The details of samples are given in Table 2.3 which indicate that the surface roughness and crystallinity are noticeably dependent on the presence of small oxygen concentrations during the preparation. The grain size of the films and the surface roughness significantly decrease when the O_2 addition is increased. Figure 2.12 shows the XRD patterns of TiO_2 films deposited at different $\text{O}_2/(\text{Ar} + \text{O}_2)$ ratios. These diffraction patterns show three well-defined peaks corresponding to the planes (1 0 1), (2 0 0) and (2 1 1) of the anatase crystalline phase (JCPDS 21-1272). The intensity of the anatase peaks depends on the oxygen concentration in the chamber during sample preparation, increasing the peak intensities as the $\text{O}_2/(\text{Ar} + \text{O}_2)$ ratio from 0 to 0.2, and decreasing again for $\text{O}_2/(\text{Ar} + \text{O}_2) = 0.3$. It was noticed that an excessive presence of oxygen during film deposition obstructs the crystallization of the anatase phase.

Table 2.3 Grain size (D), average surface roughness (R_{ave}) and thickness calculated with the Sanepoel method of samples produced at various $O_2/Ar + O_2$ ratios (Grayeli Korpi *et al.*, 2017).

Samples	$O_2/Ar + O_2$ ratio	D (nm)	R_{ave} (nm)	thickness (nm)
1	0	144.2	18.9	304.12
2	0.1	121.5	14.2	299.51
3	0.2	26.0	3.4	295.94
4	0.3	18.1	2.0	295.06

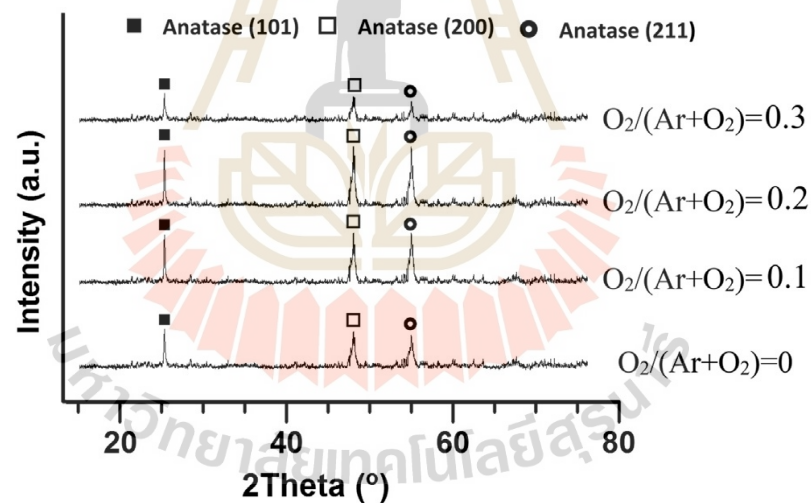


Figure 2.12 XRD patterns of various samples produced at different $O_2/Ar + O_2$ ratios (Grayeli Korpi *et al.*, 2017).

For optical results, the transmittance spectra of the TiO_2 films at various $O_2/Ar + O_2$ ratios are shown in Figure 2.13. The average transmittance of the different samples is approximately 85% in the visible region respecting to reference blank glass substrate. When the sample prepared under pure Ar ambient, the transmittance in visible light is decrease, probably due to its larger surface roughness.

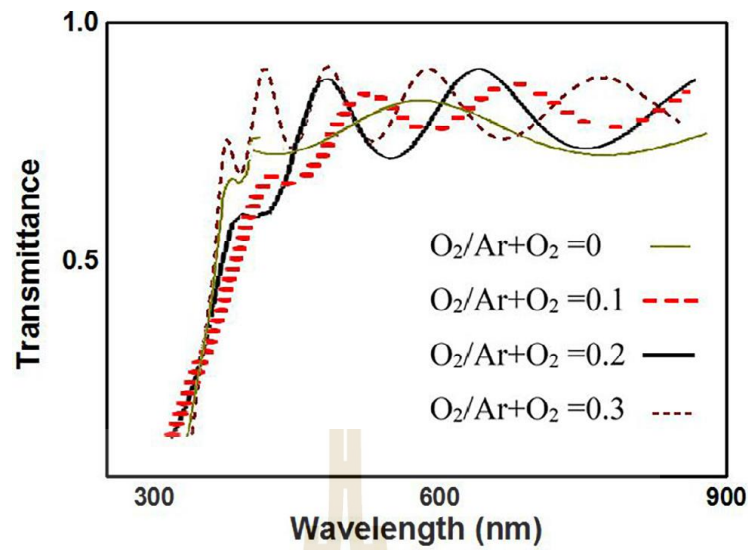


Figure 2.13 Optical transmittance spectra of various samples produced at different $O_2/Ar + O_2$ ratios (Grayeli Korpi *et al.*, 2017).

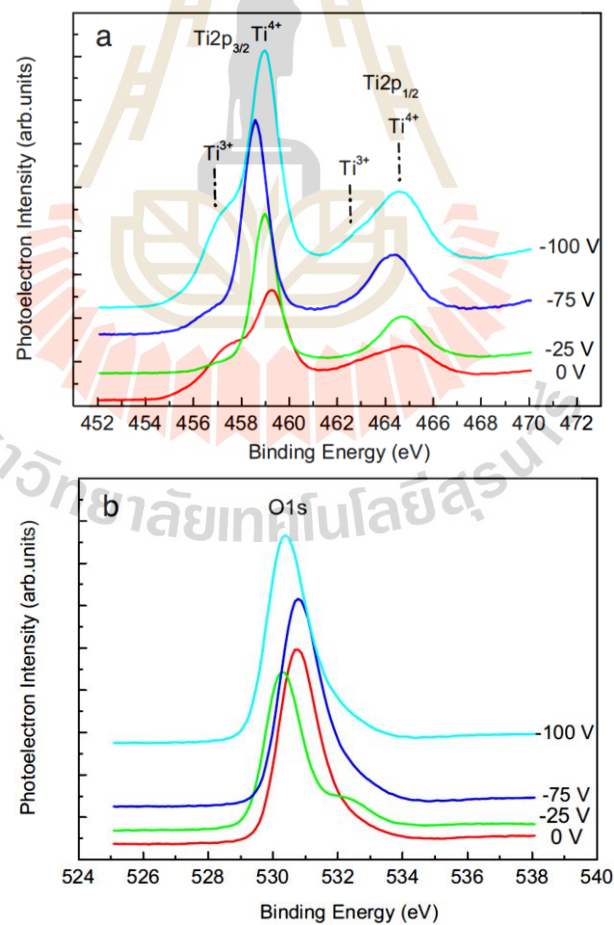


Figure 2.14 Ti2p (a) and O1s (b) XPS spectra of TiO_2 thin films (Nezar *et al.*, 2017).

Nezar *et al.* show that it is possible to deposit nanocrystalline anatase TiO_2 thin films on both biased and unbiased glass substrates by controlling the sputtering conditions. Pure metal titanium target (99.99%) was used as a sputtering target. The sputtering gas and reactive gas were pure argon (99.99990%) and pure oxygen (99.99%) respectively. The voltage applied to the substrate was varied (0, -25, -50, -75 and -100 V) whereas all other deposition parameters were constant (sputtering power = 250 W, deposition time = 60 min, working gas pressure = 2.66 Pa, 25% of oxygen flow rate, and room temperature). XPS results revealed that titanium atoms were present on the form of Ti^{4+} state corresponding to the chemical composition of TiO_2 (Figure 2.14).

2.1.3 Other Metal Oxide Thin Film

Besides SiO_2 and TiO_2 , other metal oxide such as Al_2O_3 , HfO_2 and Ta_2O_5 are common metal oxide coating materials for optical applications. HfO_2 and Ta_2O_5 films are one of the most important high refractive index materials from the ultraviolet to near-infrared region. Ta_2O_5 films are the preferred high-refractive-index materials in the field of ultra-low loss laser films, and HfO_2 films are the preferred high refractive index materials in the field of high laser damage threshold films (Wang *et al.*, 2017). Wang *et al.* studied the effects of hot-isostatic pressing and annealing post-treatment on HfO_2 and Ta_2O_5 films prepared by ion beam sputtering. In the aspect of optical properties, both post-treatment methods can increase physical thickness and reduce refractive index and extinction coefficient. Figure 2.15 shows effect of hot-isostatic pressing and annealing treatment on optical constants of HfO_2 and Ta_2O_5 films

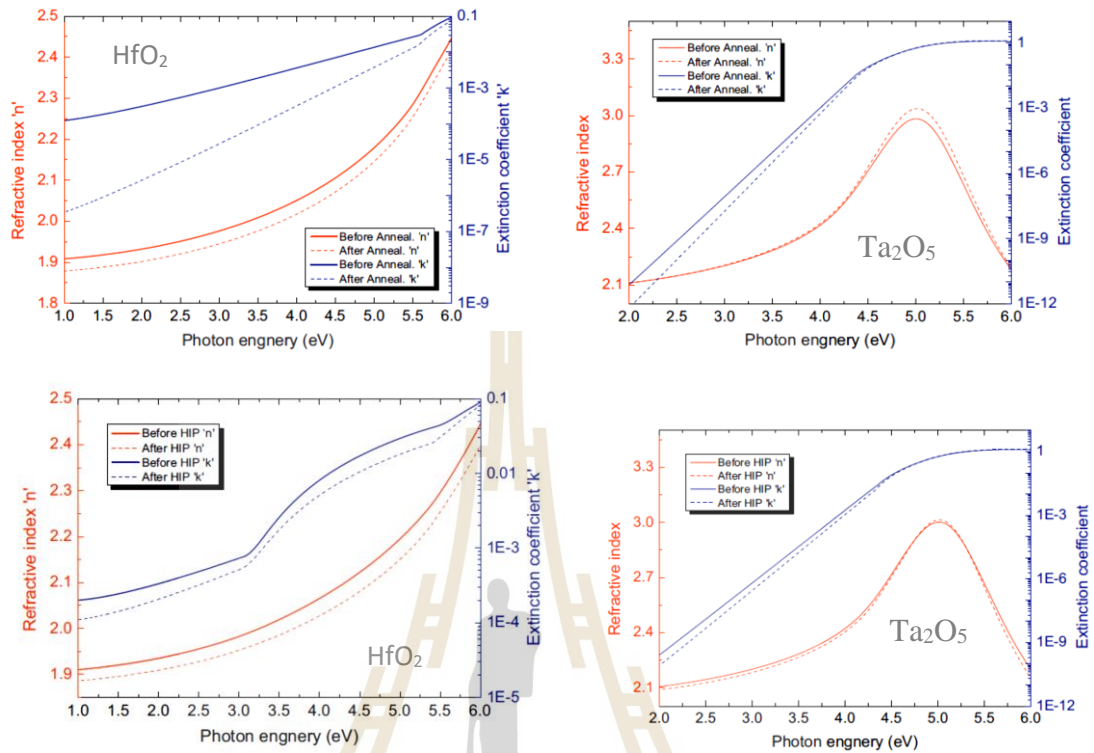


Figure 2.15 Effect of hot-isostatic pressing and annealing treatment on optical constants of HfO_2 and Ta_2O_5 films (Wang *et al.*, 2017).

Kesmez *et al.* fabricated single layer and multilayer films consisting of SnO_2 , Ta_2O_5 , SiO_2 , TiO_2 , indium tin oxide (ITO) and antimony tin oxide (ATO) by sol-gel dip coating technique. Table 2.4 indicates the light transmittance, thickness, refractive index and roughness of single layer films and light transmittance of multilayer films. Among the single layer films, porous SiO_2 film had the highest light transmittance of 95%. Figure 2.16 present the light transmittance plots of single layer films as a function of wavelength. It is obvious that the highest transmittance can be achieved in the SiO_2 film in the 300–900 nm region. All of the studied oxides except silicon dioxide resulted in a decrease in the light transmittance comparing with uncoated glass when applied in single layer form. This was expected, since the refractive indices of these oxides are higher than that of the glass.

Table 2.4 Light transmittance(Measured by Hazameter, at 550 nm), refractive indices and thickness values of single layer films and light transmittance values of multilayer films (Kesmez *et al.*, 2018).

Sample	%Light Transmittance	Reflective index	Film thickness (nm)	Roughness (rms)(nm)
Bare glass	89.5	-	-	-
SiO ₂	95	1.36	103	1.20
Ta ₂ O ₃	86.7	1.70	34	8.95
ATO	87.1	1.64	38	11.46
ITO	89	1.54	30	7.83
SnO ₂	86.9	1.67	71	2.30
TiO ₂	89.1	1.99	115	23.44
ITO-TiO ₂ -SiO ₂	97.5	-	-	-
ITO-Ta ₂ O ₅ -SiO ₂	96.2	-	-	-
SnO ₂ -TiO ₂ -SiO ₂	94.9	-	-	-
SnO ₂ -Ta ₂ O ₅ -SiO ₂	95.1	-	-	-
ATO-TiO ₂ -SiO ₂	80.4	-	-	-

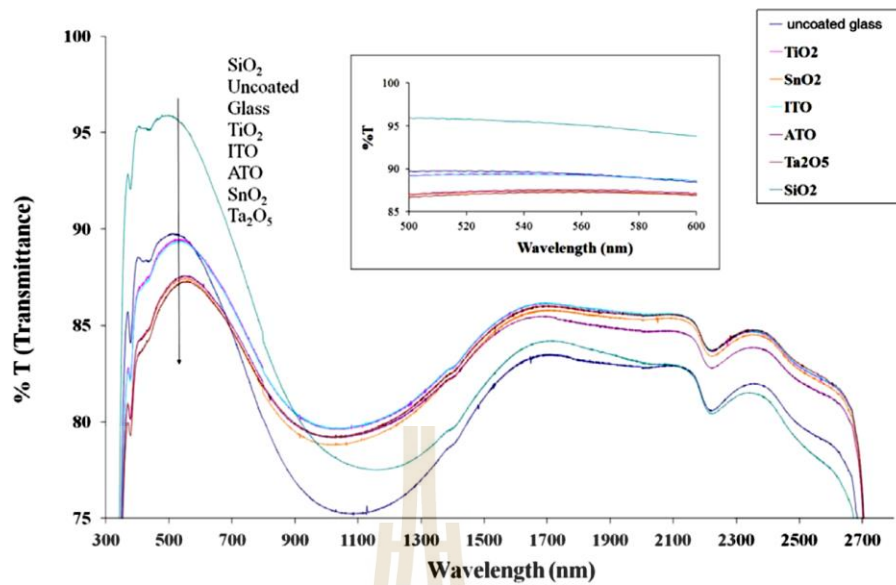


Figure 2.16 % light transmittance spectra of single layer films (Kesmez *et al.*, 2018).

2.2 Thin Films for Optical Applications

2.2.1 Interference in thin films

Basically, interference effects are commonly observed in thin films, such as thin layers of oil on water or the thin surface of a soap bubble. The varied colors observed when white light is incident on such films result from the interference of waves reflected from the two surfaces of the film. Consider a film of uniform thickness t and refraction index (RI) n . The wavelength of light λ_n in the film is

$$\lambda_n = \frac{\lambda}{n} \quad (1)$$

where λ is the wavelength of the light in free space and n is the refractive index of the film material. Let's assume light rays traveling in air are nearly normal to the two surfaces of the film as shown in Figure 2.17. Reflected ray 1, which is reflected from the upper surface (A) in Figure 17, undergoes a phase change of 180° with respect to the incident wave. Reflected ray 2, which is reflected from the lower film surface (B), undergoes 180° phase change because it is reflected from a glass that has a higher refractive index than that of film. Therefore, ray 1 is in phase with ray 2. We must also consider, however, that ray 2 travels an extra distance $2d\cos\theta_2$ before the waves recombine in the air above surface A. If $2d\cos\theta_2 = \lambda_n$, rays 1 and 2 recombine in

phase and the result is constructive interference. In general, the condition for constructive interference in thin films is (Serway *et al.*, 2014)

$$2d\cos\theta_2 = m\lambda_n \quad m = 0, 1, 2, \dots \quad (2)$$

Because $\lambda_n = \lambda/n$, Equation 2 can be written as

$$2nd\cos\theta_2 = m\lambda \quad , m = 0, 1, 2, \dots \quad (3)$$

If the extra distance $2d\cos\theta_2$ traveled by ray 2 corresponds to a multiple of λ_n , the two waves combine out of phase and the result is destructive interference. The general equation for destructive interference in thin films is

$$2nd\cos\theta_2 = \left(m + \frac{1}{2}\right)\lambda \quad , m = 0, 1, 2, \dots \quad (4)$$

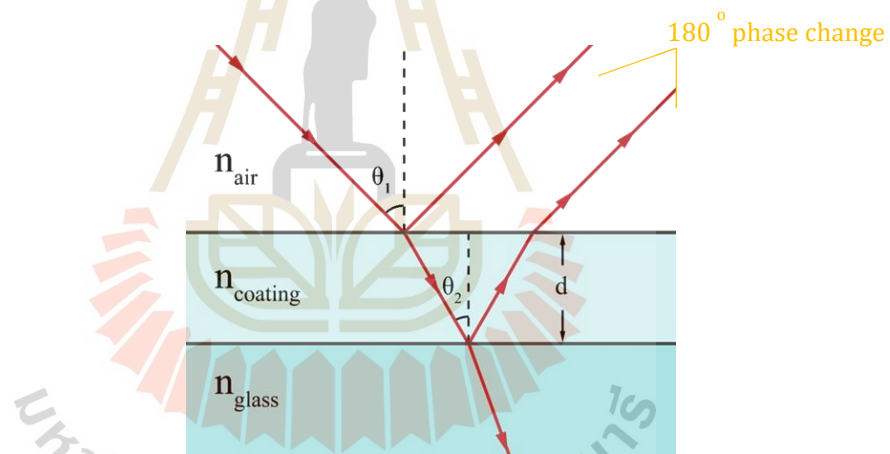


Figure 2.17 Light paths through a thin film on glass (https://en.wikipedia.org/wiki/Thin-film_interference).

2.2.2 Multilayer thin films

A multilayer coating consisting of m thin homogeneous and isotropic layers on a thick substrate is considered as shown in Figure 2.18. Normally, a film is considered to be thin in the case when full interference effects are observable in the reflected or transmitted light. At a boundary between two media, denoted by suffix 0 for the incident medium and by suffix 1 for the exit medium, the incident beam is split into a

reflected beam and a transmitted beam. For normal incidence, we have the amplitude reflection r and transmission t coefficients are: (Macleod, H.A., 2010).

$$r = \frac{\eta_o - \eta_1}{\eta_o + \eta_1} \quad (5)$$

$$t = \frac{2\eta_o}{\eta_o + \eta_1}, \quad (6)$$

where η is optical admittance.

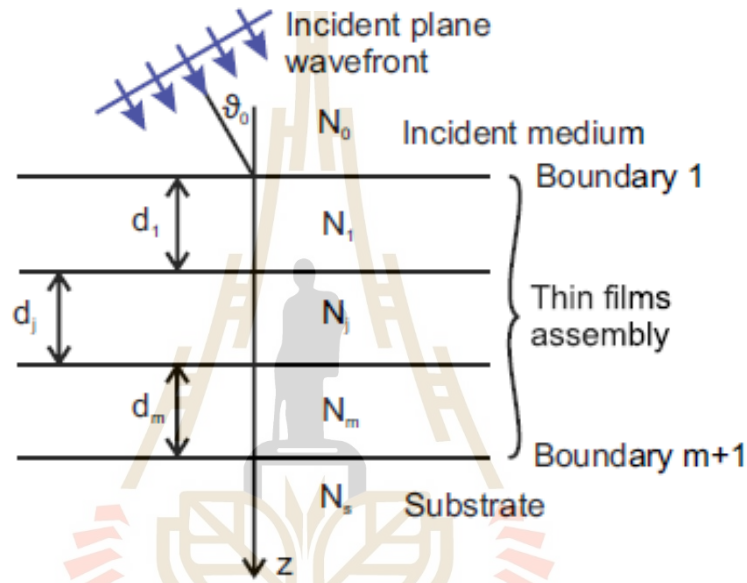


Figure 2.18 Schematic of a multilayer thin films (Fedulova et al., 2016).

In order to avoid fundamental difficulties, the incident medium is considered to be absorption-free, which means η_o is real, then the intensity transmission and reflection coefficients (transmittance T and reflectance R) are given by:

$$R = \left(\frac{\eta_o - \eta_1}{\eta_o + \eta_1} \right) \left(\frac{\eta_o - \eta_1}{\eta_o + \eta_1} \right)^* \quad (7)$$

$$T = \frac{4\eta_o \text{Re}(\eta_1)}{(\eta_o + \eta_1)(\eta_o + \eta_1)^*} \quad (8)$$

The reflectance of an assembly of thin films is calculated through the concept of optical admittance. We replace the multilayer by a single surface (Macleod, H.A., 2010), which presents an admittance Y that is the ratio of the total tangential magnetic and electric fields and is given by

$$Y = C/B \quad (9)$$

Where

$$\begin{bmatrix} B \\ C \end{bmatrix} = \left\{ \prod_{r=1}^q \begin{bmatrix} \cos \delta_r & (i \sin \delta_r) / \eta_r \\ i \eta_r \sin \delta_r & \cos \delta_r \end{bmatrix} \right\} \begin{bmatrix} 1 \\ \eta_m \end{bmatrix} \quad (10)$$

$\delta_r = 2\pi N d \cos \vartheta / \lambda$ (ϑ is the angle between the ray and normal line to film boundary) and η_m = substrate admittance.

The order of multiplication is important. If q is the layer next to the substrate, then the order is

$$\begin{bmatrix} B \\ C \end{bmatrix} = [M_1][M_2] \cdots [M_q] \begin{bmatrix} 1 \\ \eta_m \end{bmatrix} \quad (11)$$

M_1 indicates the matrix associated with layer 1, and so on. Y and η are in the same units. As in the case of a single surface, η_o must be real for reflectance and transmittance to have a valid meaning. By using the general characteristic matrix of an assembly of m thin layers, then the basic formulas for calculating spectral characteristics of a multilayer coating are given as follows:

$$R = \frac{(\eta_o B - C)(\eta_o B - C)^*}{(\eta_o B + C)(\eta_o B + C)^*} \quad (12)$$

$$T = \frac{4\eta_o \text{Re}(\eta_s)}{(\eta_o B + C)(\eta_o B + C)^*} \quad (13)$$

In order to design multilayer thin film for optical application, free or commercial software can calculate the performance of an assembly and help as a guideline before fabrication.

In 2012, Han, K. *et al.* fabricated $\text{TiO}_2/\text{SiO}_2$ multilayer film structure by the sol-gel synthesis with thermal treatment processes. Removing the hydrophobic alkoxy groups from the pre-deposited film surface is necessary to fabricate well defined multilayer film structures, as shown in Figure 2.19b. Figure 2.20 shows FE-SEM images of the 2nd TiO_2 film surfaces including the contact angle photographs on the 1st SiO_2 films for the 250nm TiO_2 film. The 1st SiO_2 surface characteristics were varied with sintering conditions which affect the amounts of the residual ethoxy groups ($\text{Si}(\text{OC}_2\text{H}_5)_4$ used as a SiO_2 precursor) on the surface (proved by FTIR spectra). The higher amounts

of the residual ethoxy groups on the surface, the lower the surface energy to overcome the surface tension of the coating solution (Figure 2.19a). The well-defined $\text{TiO}_2/\text{SiO}_2$ multilayer assembly was successfully fabricated at a sintering temperature of 300°C by forming a hydrophilic SiO_2 layer with the heating-up period (Han, K. *et al.*, 2012).

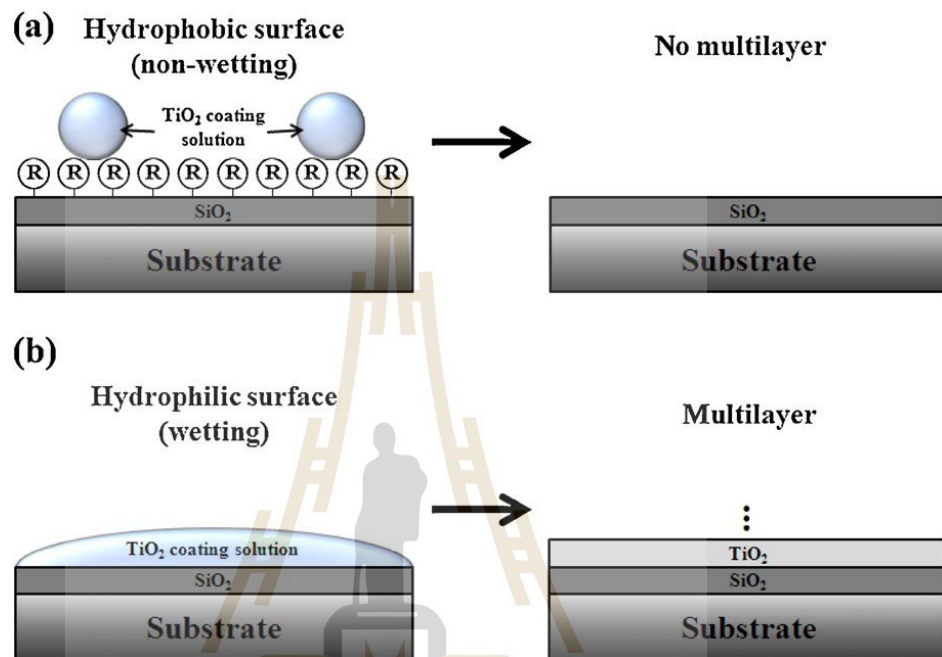


Figure 2.19 Schematics of (a) hydrophobic and (b) hydrophilic surfaces of the SiO_2 film. The R represents alkoxy group remained after sintering on the SiO_2 film surface. TiO_2 coating solution was applied to the SiO_2 film surfaces to fabricate the multilayer structure (Han, K. *et al.*, 2012).

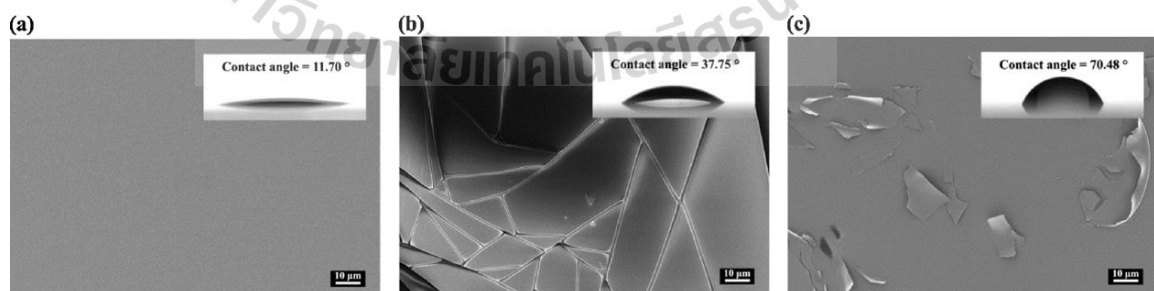


Figure 2.20 Examples of FE-SEM images of the 2nd TiO_2 250nm film surfaces for (a) clear, (b) cracks, and (c) delamination morphologies. The inserted contact angles were measured on the 1st SiO_2 films before deposition of the 2nd TiO_2 film (Han, K. *et al.*, 2012).

2.2.3 Anti - Reflective Coating

The optical phenomenon, reflection is born out of a transition in the medium in which light is travelling. The mathematical model or the vector method to deduce the condition for anti-reflection considers a single layer thin film (refractive index, n) on a glass substrate (n_s) as shown in Figure 2.19. The interference effect is considered under the two following assumptions: (1) the reflected waves have the same intensity and one reflected wave per interface and (2) other optical interactions such as scattering, absorption etc. are negligible. Therefore, from Figure 2.21, if ray 1 and ray 2, the two reflected waves, undergo a destructive interference, thereby cancelling each other, there would be no reflection. From this follow the two essential criteria for Anti-Reflection. The reflected waves are π radians out of phase or the phase difference, δ is $n\pi/2$. The thickness of the film (d) is an odd multiple of $\lambda/4$ where λ is the wavelength of the incident beam. As the equation governing phase difference is $\delta = 2\pi n d \cos\theta/\lambda$, substituting the value of δ and d , we get $\theta = 0$, that is normal incidence. The reflectance at normal incidence is given by (Raut *et al.*, 2011)

$$r = \left[\frac{n_{air}n_s - n^2}{n_{air}n_s + n^2} \right]^2 \quad (14)$$

Where, n_s , n_{air} and n are refractive index of the substrate, air and film respectively

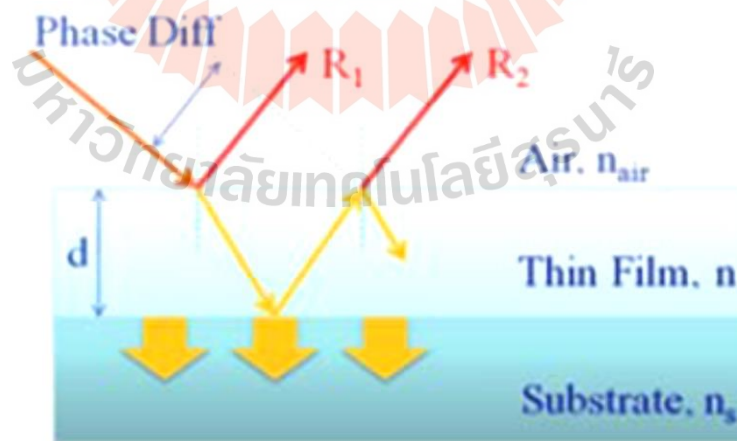


Figure 2.21 Propagation of light rays through a single layer film on substrate ($n_s > n$) (Raut *et al.*, 2011).

As the objective is to achieve zero reflectance, R is set to zero and the refractive index of the film (n) is found to be $\sqrt{n_{air}n_s}$. The fact that reflectance (R) proposed by Fresnel is dependent on the s and p-polarization of the light, the anti-reflective property is also analyzed on the basis of those parameters (Raut *et al.*, 2011).

2.2.4 High Reflection Coating

For the metal multi-dielectric mirror coatings, the basic principle, illustrated in Figure 2.22, consists in enhancing the reflectivity of a metal film at a given wavelength band by exploiting interference effects in thin films. A high reflectivity (R) metal layer (Al: $R \sim 92\%$; Ag: $R \sim 96\%$) is overcoated with one or several pairs of transparent films of high (H) and low (L) refractive index. For this purpose, dielectric films like SiO_2 , MgF_2 (L-materials) or HfO_2 , Nb_2O_5 , TiO_2 (H-materials) are used. For the selection of the coating materials, properties like residual stress, adherence, resistivity to abrasion and humidity, and coating yield are of importance. The optical thickness of the layers is usually chosen to be $\lambda/4$. The dielectric coatings lead, therefore, to a wavelength- and angle dependent modulation of the reflectivity. The larger the ratio of the refractive index of the LH pair, the higher is the peak reflectivity and width of the enhanced region. Adding LH pairs, optimized for the same wavelength, will increase the reflectivity but narrow down the useful range. The layer stack terminates usually with a H-layer (Braem *et al.*, 2005).

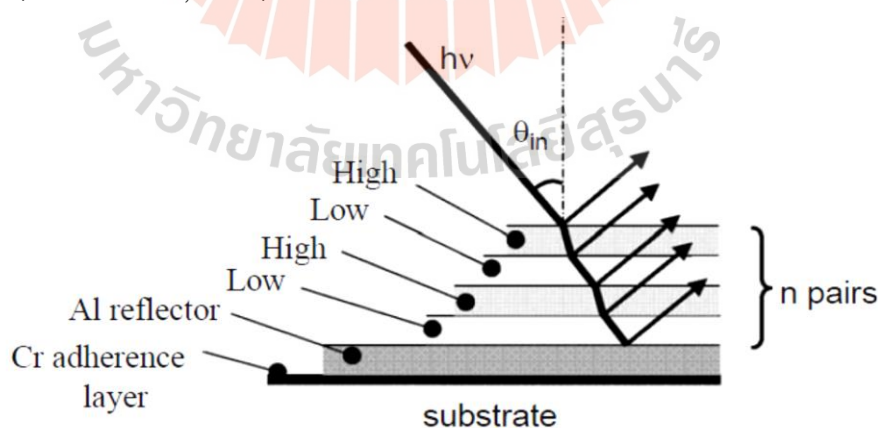


Figure 2.22 Schematic representation of a metal multi-dielectric mirror (Braem *et al.*, 2005).

Dubey, R. S. *et al.* fabricated of $\text{TiO}_2/\text{SiO}_2$ stacks based Bragg reflectors by using sol-gel spin coating technique. The prepared single-layer thin films of TiO_2 and SiO_2 onto glass substrates were characterized for their optical constants. One-seven distributed Bragg reflectors (DBR) stacks of $\text{TiO}_2/\text{SiO}_2$ were prepared by tuning the process parameters. The refractive indices (by using Filmetrics, F20) of TiO_2 and SiO_2 films are 2.2 and 1.4 respectively. By increasing of the number of DBR stacks, the reflectance increased with the shift towards higher wavelength range as shown in Figure 2.23.

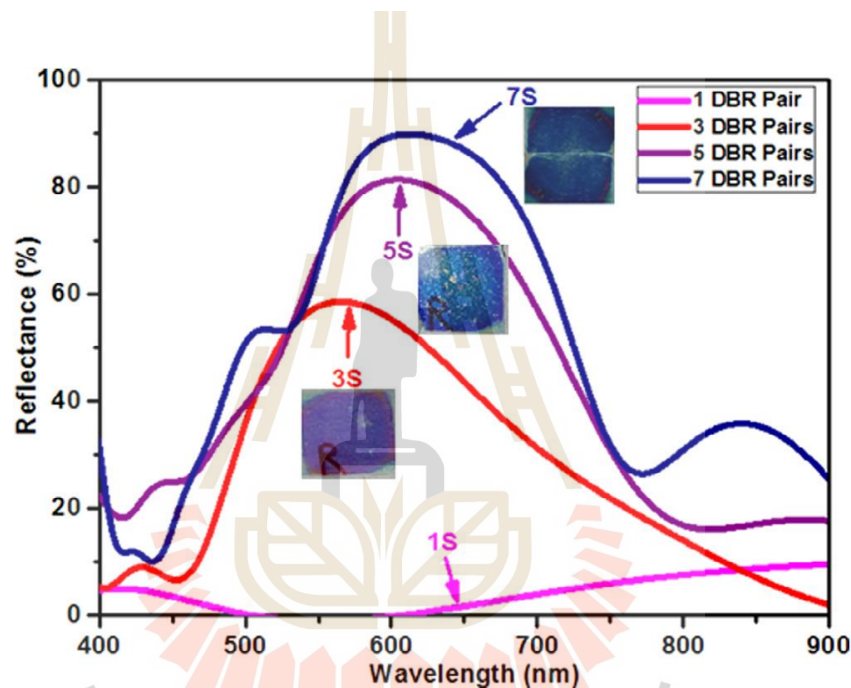


Figure 2.23 Reflectance spectra of one-, three-, five- and seven-DBR stacks with their optical images (Dubey, R. S. *et al.*, 2017).

In Han, K. *et al.*'s study in 2011, multilayer structure consisting of H/L/H ($\text{TiO}_2/\text{SiO}_2/\text{TiO}_2$) refractive index materials were prepared by sol-gel method and spin coating process (Figure 22). Film thicknesses were examined by spectroscopic ellipsometry (SE) and focused ion beam (FIB) techniques (Figure 2.24), and refractive indices of TiO_2 and SiO_2 single layer films were also measured by SE. Figure 2.25 shows the n and k values of TiO_2 and SiO_2 single layer films (Han, K. *et al.*, 2011).

Theoretical calculations and experimental data for the UV-Vis-NIR reflectance spectra from the multilayer film are shown in Figure 24. Experimental reflectance is in

good agreement with the theoretical prediction using constant refractive index for the NIR region, but it shows moderate deviation at the wavelength lower than 700 nm. It is possibly due to the large variation of the refractive index of TiO_2 , as shown in Figure 23. The highest reflectance on the NIR region was obtained with the quarter-wave condition at $\lambda=1000$ nm (Han, K. *et al.*, 2011).

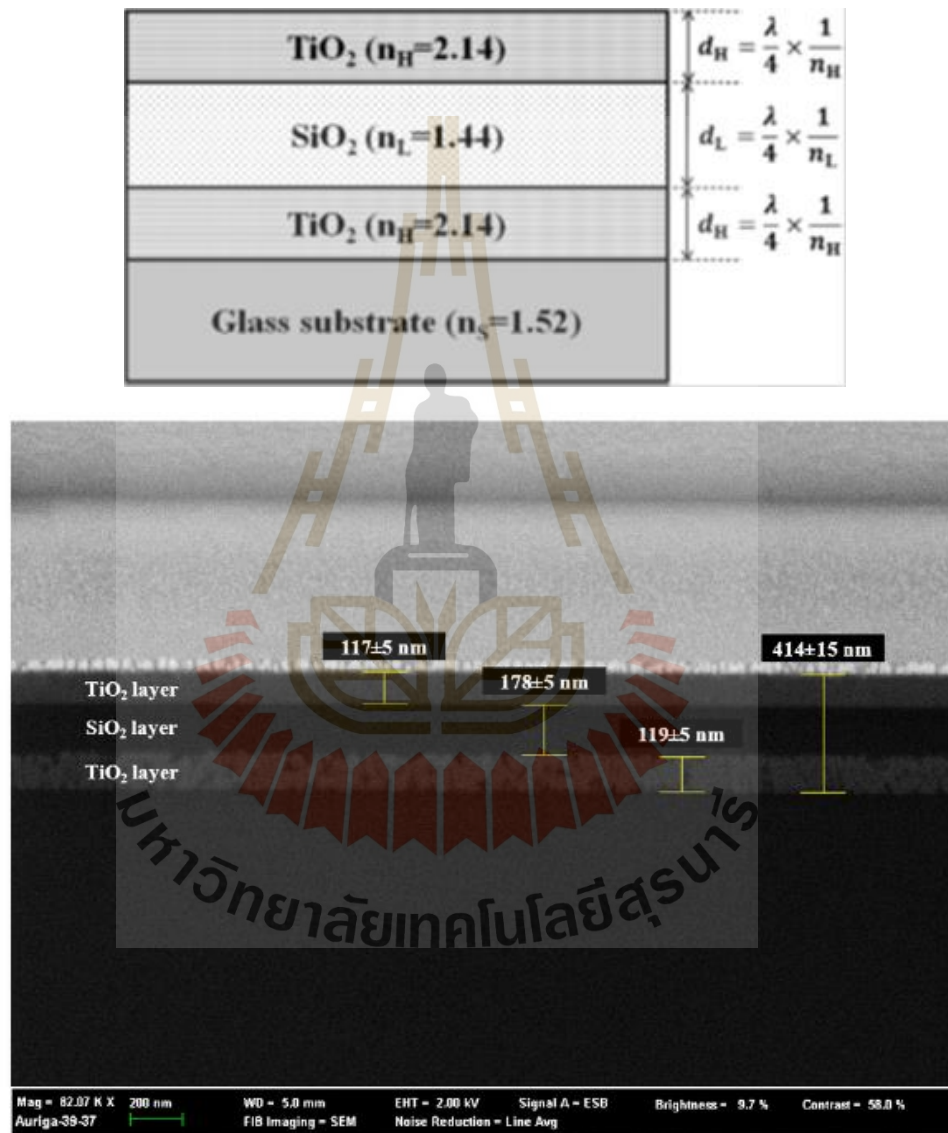


Figure 2.24 (Left) Schematic of a multilayer structure (Right) A FIB image (SEM) of a multilayer structure (Han, K. *et al.*, 2011).

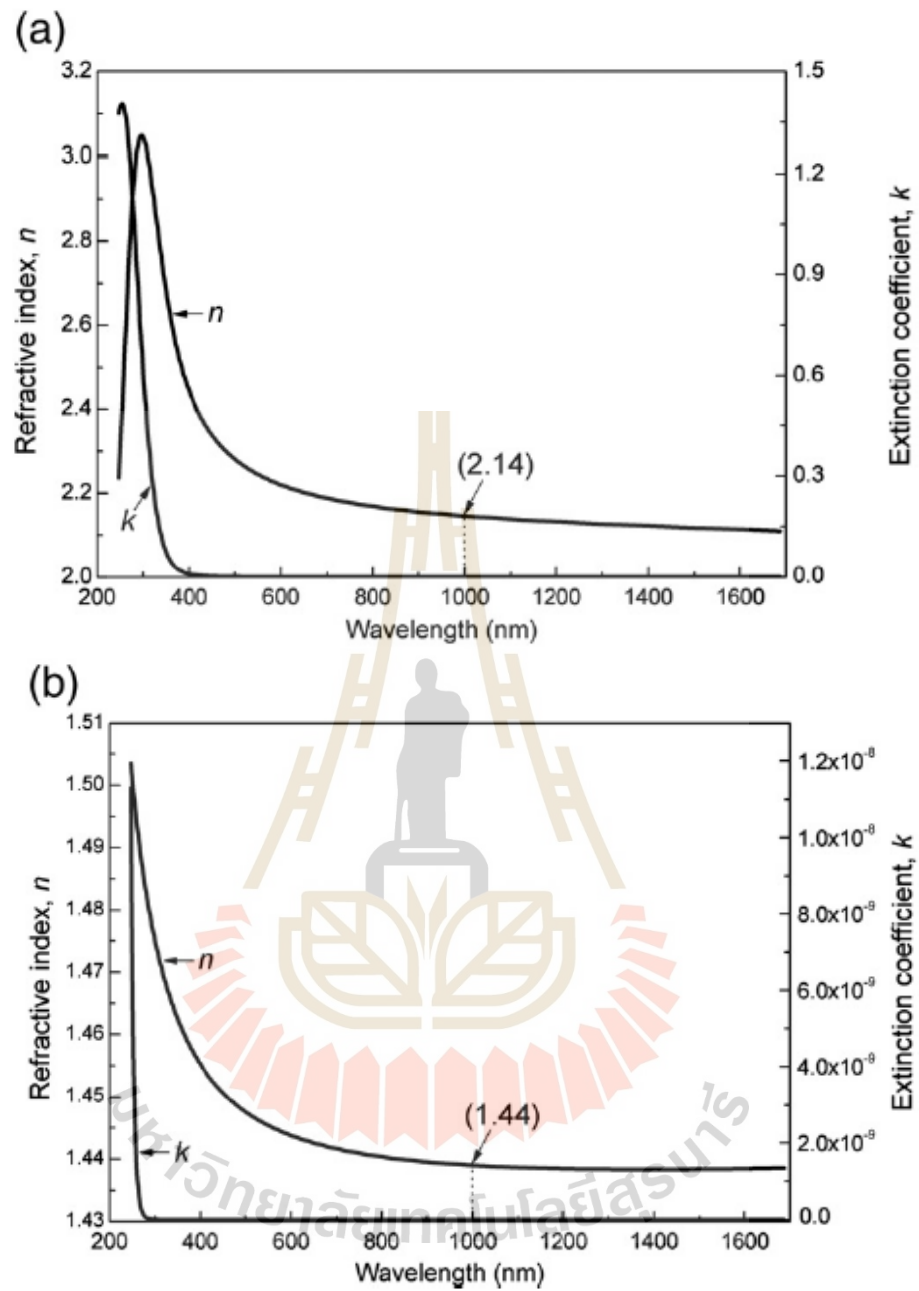


Figure 2.25 Optical constants (n and k) measured for (a) TiO₂ and (b) SiO₂ films (Han, K. *et al.*, 2011).

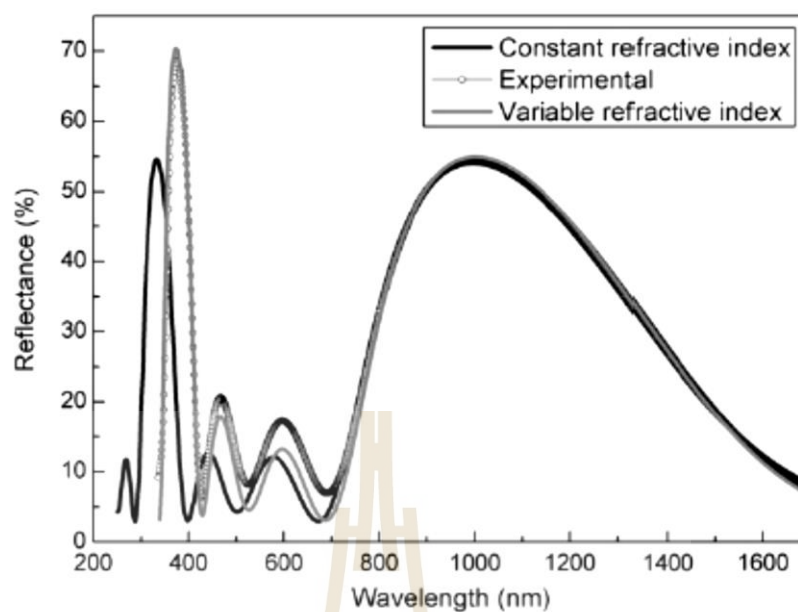
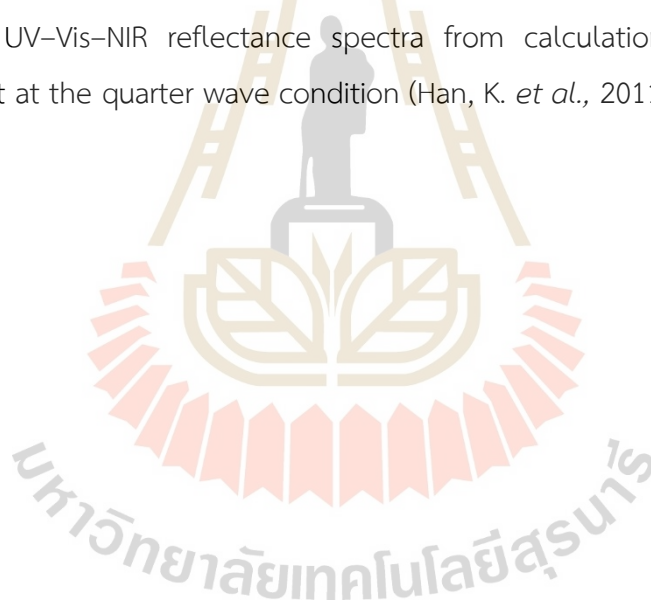


Figure 2.26 UV-Vis-NIR reflectance spectra from calculations and experimental measurement at the quarter wave condition (Han, K. *et al.*, 2011).



CHAPTER III

EXPERIMENTS AND TECHNIQUES

SiO_2 and TiO_2 single layer thin films will be deposited on glass substrates by custom-built RF magnetron sputtering of a pure SiO_2 and TiO_2 ceramic target respectively (diameter 3 inches) mm). Before each deposition, the sputtering chamber will be evacuated down to a pressure of 1×10^{-5} mbar (or lower). The film deposition carries out at room temperature. The substrate–target distance is about 15 cm. The sputtering target is continuously cooled by water. Pure argon is used as the sputtering gas and pure oxygen as the reactive gas. The effect of deposition parameters such as RF power and gas flow rate on the structural and optical properties of the samples will be studied.

The phase analysis of the prepared samples was carried out using an X-ray diffractometer. The surface morphology will be examined by SEM and AFM. XPS will be used to characterize the stoichiometry of the films and to identify the chemical state of Si and Ti atoms. The optical constants will be measured by spectroscopic ellipsometer. The optical transmittance and reflectance will be obtained by UV-Vis-NIR measurement. The local structure will be investigated by XAS. In particular, XANES gives information on oxidation state and site symmetry of Si (or Ti) and EXAFS gives detailed information on distances and coordination numbers of neighboring atom shells surrounding the Si (or Ti) atom. After getting desired optical properties of prepared single layer films and being able to control film thickness and refractive index, thin film multilayer of silicon oxide and titanium oxide materials is designed and fabricated.

3.1 Thin films preparation

3.1.1 RF Magnetron Sputter Deposition

Sputter deposition is a vacuum coating process categorized in the type of physical vapor deposition (PVD). Sputtering process is a well-known film growth technique for the coating industry.

The technique is based on ion bombardment of a source material (the target). Sputter deposition is a non-thermal vaporization process which uses a physical phenomenon to produce the microscopic spray effect. When an energetic ion strikes the surface of the target, atoms of that target material are ejected by a momentum transfer process. Sputtering working gas will be ionized and accelerated towards the target. The use of a magnetron allows trapping of the electrons by the magnetic field lines close to the sputtering target in a well-defined region. Therefore, electrons stay within the plasma for a considerably longer time, increasing the probability of ionizing the working gas. Magnetron sputtering cathodes can be run using AC or DC power supplies. The most common AC power supplies usually operate in the RF range at 13.56 MHz in order to sputter also high insulating target materials like SiO_2 or Al_2O_3 (Bräuer *et al.*, 2010).

Basically, the sputtering target is actively cooled. The cold surface minimizes the amount of radiant heat in a sputtering system and this may be an advantage over thermal evaporation in vacuums, where the radiant heat load can be appreciable. The low level of radiant heat is one factor that allows thermally sensitive surfaces to be placed near the sputtering target. Cooling also prevents diffusion in the target, which could lead to changes in the elemental composition in the surface region when alloy targets are bombarded (Mattox, Donald M., 2010).

Table 3.1 Sputtering yields by 500 eV ions (Mattox, Donald M., 2010).

	Be (9)	Al (27)	Si (28)	Cu (64)	Ag (106)	W (184)	Au (197)
He ⁺ (4amu)	0.24	0.16	0.13	0.24	0.2	0.01	0.07
Ne ⁺ (20amu)	0.42	0.73	0.48	1.8	1.7	0.28	1.08
Ar ⁺ (40amu)	0.51	1.05	0.50	2.35	2.4 – 3.1	0.57	2.4
Kr ⁺ (84amu)	0.48	0.96	0.50	2.35	3.1	0.9	3.06
Xe ⁺ (131amu)	0.35	0.82	0.42	2.05	3.3	1.0	3.01

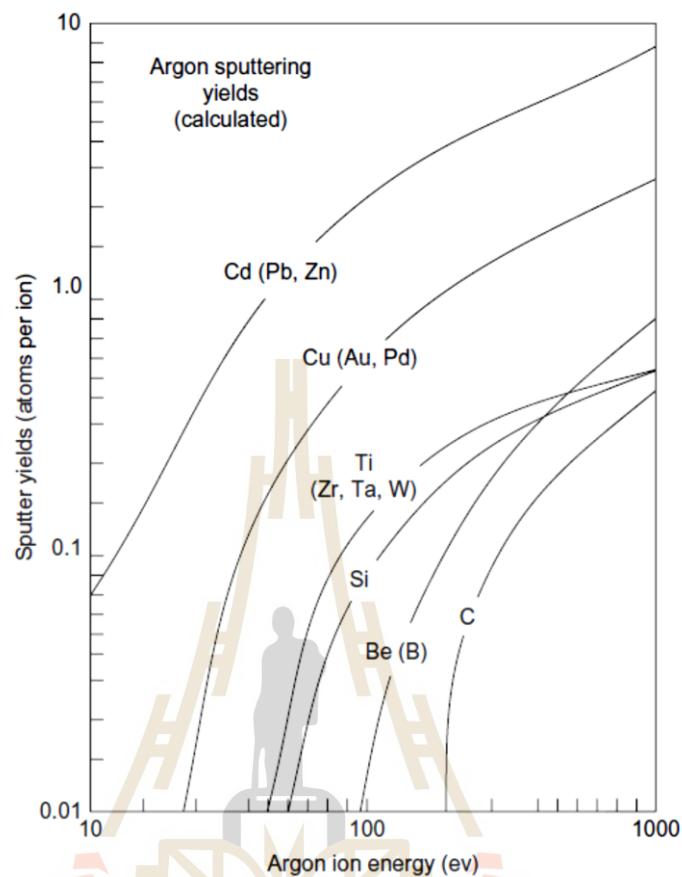


Figure 3.1 Some calculated sputtering yields (Mattox, Donald M., 2010).

The sputtering yield is the ratio of the number of atoms ejected to the number of incident bombarding particles and depends on the chemical bonding of the target atoms and the energy transferred by collision. Table 5 shows some masses of gaseous ions and target materials and the approximate sputtering yield by bombardment at the energies indicated. Figure 3.1 shows some sputtering yields by argon ion bombardment as a function of ion energy. For off-normal bombardment, the sputtering yield initially increases to a maximum then decreases rapidly as the bombarding particles are reflected from the surface; this effect is called the “angle-of-incidence effect”, as shown in Figure 3.2. The maximum sputtering yield for argon generally occurs at about 70 degrees off-normal but this varies with the relative masses of the bombarding and target species. The angle-of-incidence effect on sputtering yield, and surface mobility effects, can give rise to the development of surface features

such as cones and whiskers on the target surface. The sputtering threshold energy is a rather vague number that is the lowest energy of the bombarding particle that can cause sputtering. Generally, it is considered that incident particle energies of less than about 25 eV will not cause physical sputtering of an element. This is about the energy needed for atomic displacement in the radiation damage in solids (Mattox, 2010).

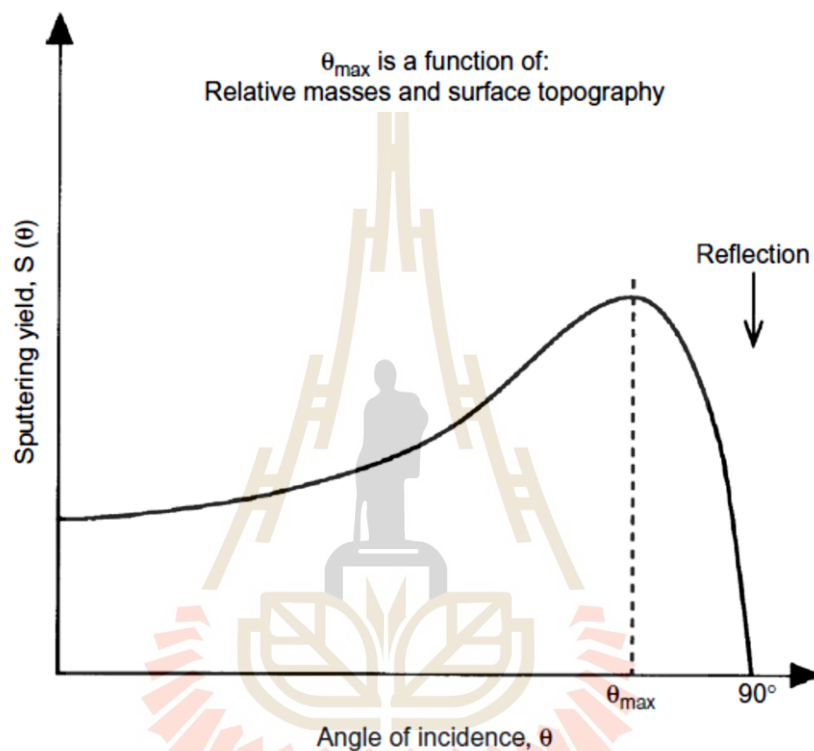


Figure 3.2 Sputtering yield as a function of angle-of-incidence of the bombarding ion (Mattox., 2010).

Magnetron sputtering emerges when a plasma is ignited in the presence of a rare gas (typically, argon) in the vicinity of the target surface. The plasma is stabilized by a magnetic field. The magnetic field thus developed traps the electrons in cycloids and keeps them circulating over the target surface in order to increase the dwell time of electrons in the gas and thereby raises the ionization probability. Magnetron sputtering sources have wide technical applications mainly in the thin film coating and processing industry. This versatile tool uses a plane solid target mounted close to an axial permanent magnet (Popok *et al.*, 2011). Schematic diagram of mechanism of magnetron sputter coating machine is shown in Figure 3.3.

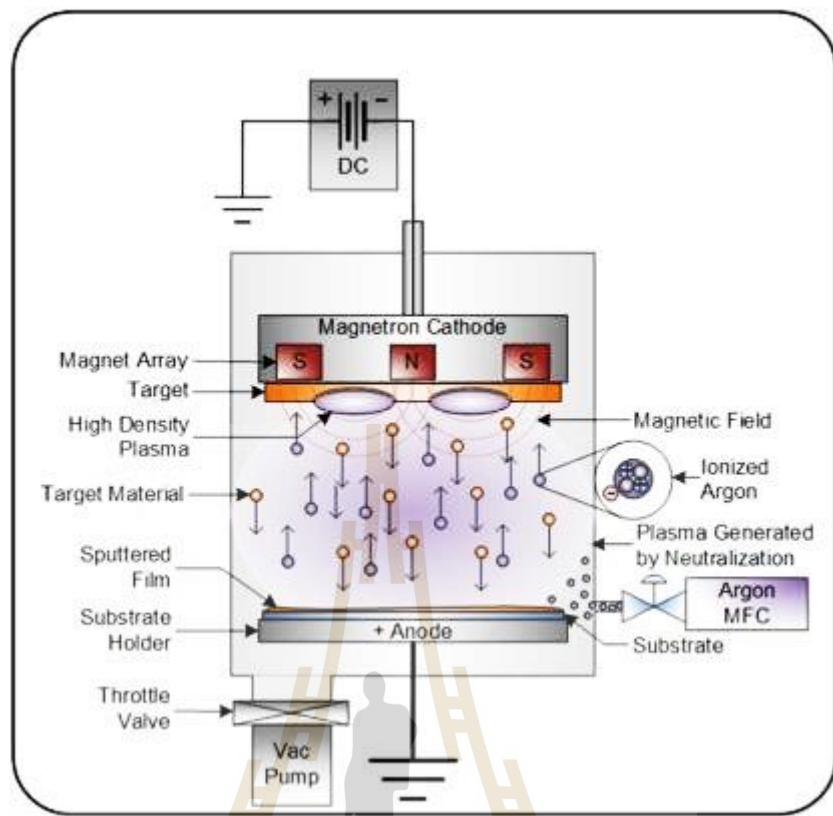


Figure 3.3 Schematic diagram of mechanism of magnetron sputter coating machine. (<https://www.sciencedirect.com/topics/materials-science/magnetron-sputtering>).

The sputtering parameters which affect the properties of the resulting films are listed below:

- The sputtering power – It influences the rate of deposition process
- The applied voltage – It determines the maximum energy of the sputtered particles ejected from the target surface and the sputtering yield.
- Sputtering gas pressure & Target- substrate distance – They control the mean free path of the sputtered particles and thereby the porosity, crystallinity and texture of the deposited thin films.
- Reactive gas mixture – It affects the film stoichiometry.
- Substrate temperature – It controls the density of the thin films and also the behavior of film growth with respect to crystallinity.
- Bias-voltage to substrate – It determines the growth of the layer.

By controlling preparation conditions, the films with desired properties can be obtained from sputtering technique and it has high potential to be tunable.



Figure 3.4 RF magnetron sputtering system at BL6, SLRI.

3.1.2 Reactive Gas Timing Sputter Deposition

In the gas-timing approach, the flow of the sputtering gas is purposefully controlled via an on-and-off sequence. This technology has been used on our sputtering machine to produce high-quality crystalline thin films at ambient temperature and low RF power. Without any annealing treatment following deposition, high-quality crystalline thin films may be produced using this method (Klaitabtim, D. *et al.*, 2008). In general, the deposition rate and film characteristics are determined by the amount of reactive gas given to the system. When a film is deposited in metallic mode, the sputtering rate is high, and the resulting film is substoichiometric and rich in metallic elements. At high O_2 reactive gas in oxide mode, the film stoichiometric and deposition rate are poor because the target is covered by an oxide or nitride layer, a phenomenon known as the poisoning of sputtering target effect. To obtain both a high deposition rate and stoichiometric film, it is desirable to optimize the O_2 flow rate in transition mode. However, it was discovered that the deposition in the transition mode was unstable owing to the "hysteresis effect." The reactive gas-timing (RGT)

approach was an alternate deposition process in which the fluxes of the sputtered or reactive gases were purposefully regulated by an on-off sequence. It has been claimed that this technology successfully enhanced the standard reactive magnetron sputtering process by enabling the control of film composition at high deposition rates at low temperatures. Figure 3.5 shows Schematic representation of argon and oxygen mass flow rate versus time used for depositing TaO thin film by the conventional reactive sputtering and RGT techniques (Chittinan, D. *et al.*, 2019). The Reactive Gas Timing magnetron sputtering system at NECTEC is shown in Figure. 3.6.

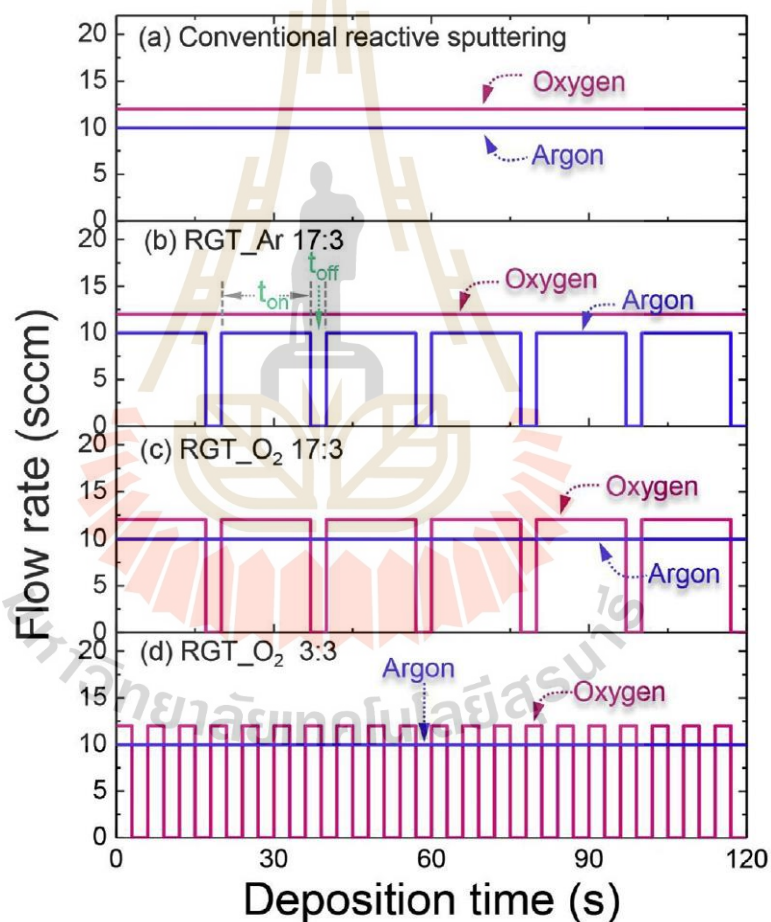


Figure 3.5 Schematic representation of argon and oxygen mass flow rate versus time used for depositing TaO thin film by the conventional reactive sputtering and RGT techniques (Chittinan, D. *et al.*, 2019).

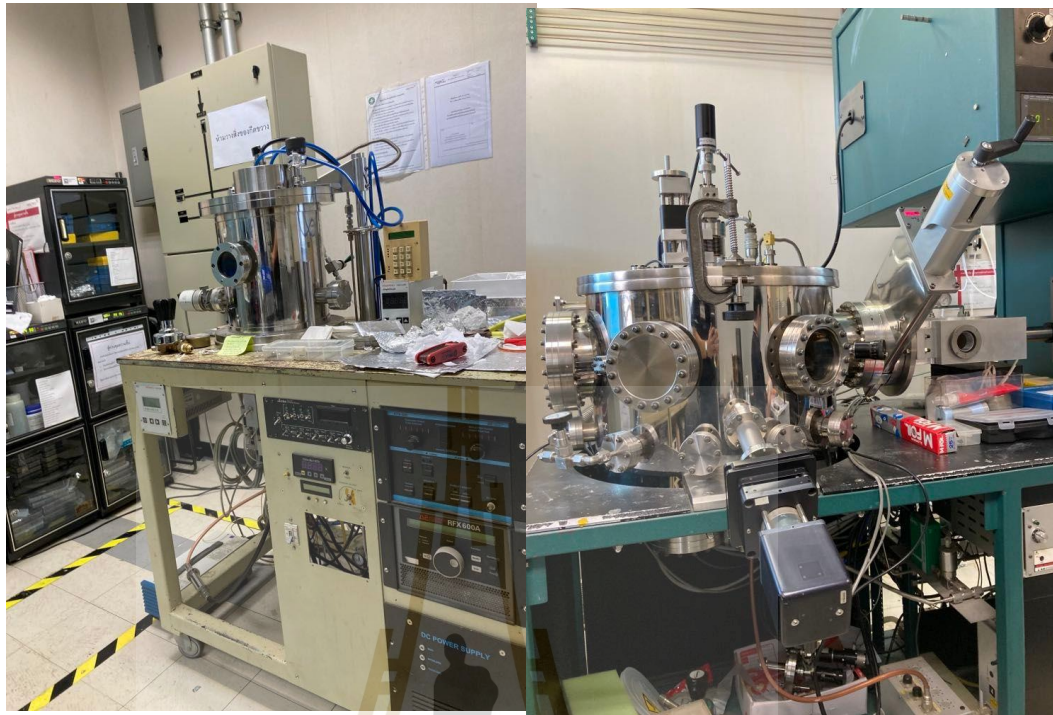


Figure 3.6 Reactive Gas Timing magnetron sputtering system at NECTEC.

3.2 Thin films characterization techniques

Several different techniques will be used to analyze or characterize the film samples fabricated in the magnetron sputtering system. It has already been established that understanding the crystallographic phase composition, surface morphology, chemistry, and lattice defect structure is important to the research purposes for which the system was made. The importance techniques used to examine these qualities will now be summarized.

3.2.1 X-ray diffraction (XRD)

X-ray diffraction is a common material characterization technique that provides detailed information about the crystallographic structure, chemical composition, and physical properties of materials. It also allows for identification of crystal orientations and interatomic spacing ($d_{(hkl)}$). Subsequently, XRD results were showed relationship between intensity of diffraction plane peak and 2θ which come from incident X-ray direction. In plane X-ray waves, are used for this technique because wavelength is on

the same length scale as interatomic spacing and lattice parameter values. X-ray diffraction data is analyzed by using Bragg's equation (3.1) as shown in following.

For explanation of XRD equations, there are incident's X-ray wave in the same plane that incident to atomic structure plane (s1, s2 etc.). Then, based on natural of EM wave, interval between ab+ bc = $n\lambda$ including de+ef = $m\lambda$ where n and m are counting number. Figure 3.4 showed this relationship for plan and adjacent plan. Moreover, useful trigonometry theory, we can show $\sin \theta = ab/d_{(hkl)}$, and $\sin \theta = bc/d_{(hkl)}$. For above, we will get this equation as shown in Equation 3.17.

$$n\lambda = 2d_{(hkl)}\sin\theta \quad (3.1)$$

and the angle of reflection for a particular set of lattice planes (hkl) is given as

$$2\theta = 2\sin^{-1}\left(\frac{n\lambda}{2d_{(hkl)}}\right) \quad (3.2)$$

where n is n is the order of reflection, λ is the wavelength of x-rays, $d_{(hkl)}$ is the characteristic spacing between the crystal planes of a given specimen, and θ is the angle between the incident beam and the normal to the reflecting lattice plane.

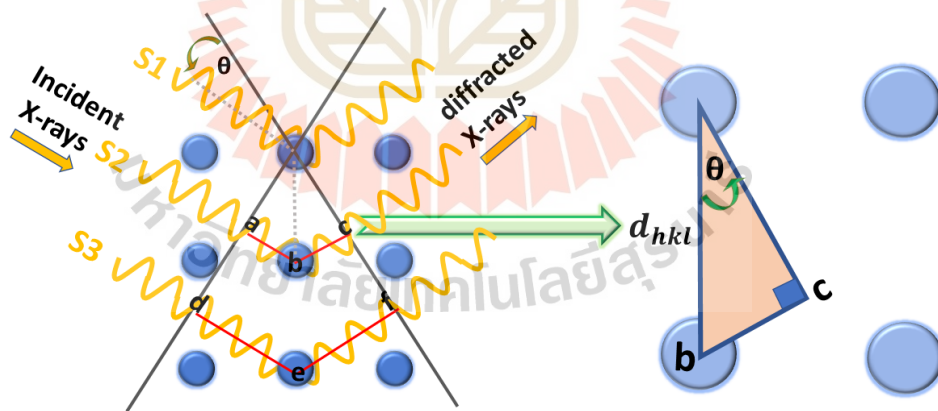


Figure 3.7 Schematic representation of Bragg's Law for XRD.

In this work, XRD measurement were performed using XRD (BRUKER, D8 ADVANCE) with Cu K_{α} radiation at a wavelength of 1.5406 Å from a generator operating at 40 kV and 40 mA.



Figure 3.8 XRD (BRUKER, D8 ADVANCE) at SUT. (<http://cste.sut.ac.th/2014/?p=1920>)

3.2.2 Scanning electron microscopy (SEM)

Scanning electron microscopy (SEM) produces images of surface sample by scanning the surface with a focused beam of electrons as shown in Figure 3.9. The principle of SEM is based on the interaction between an incident electron and the solid specimen. This interaction can produce signals that contain information about the surface topography and elemental composition of the sample. SEM images are produced by collecting two types of electrons which are backscattered electrons (BSE) and secondary electrons (SE). The secondary electrons are originated from atoms on sample surface that interact as inelastic collision with the electron beam. On the other hand, the backscattered electrons are the primary electrons which are reflected after elastic interactions between the electron beam and atoms. They are originated from deeper regions of sample surface. The BSE and SE carry different types of information. BSE image is highly sensitive to differences in atomic number such that the higher the atomic number and the brighter the material appears in the image, while SE image can provide more detailed surface information.

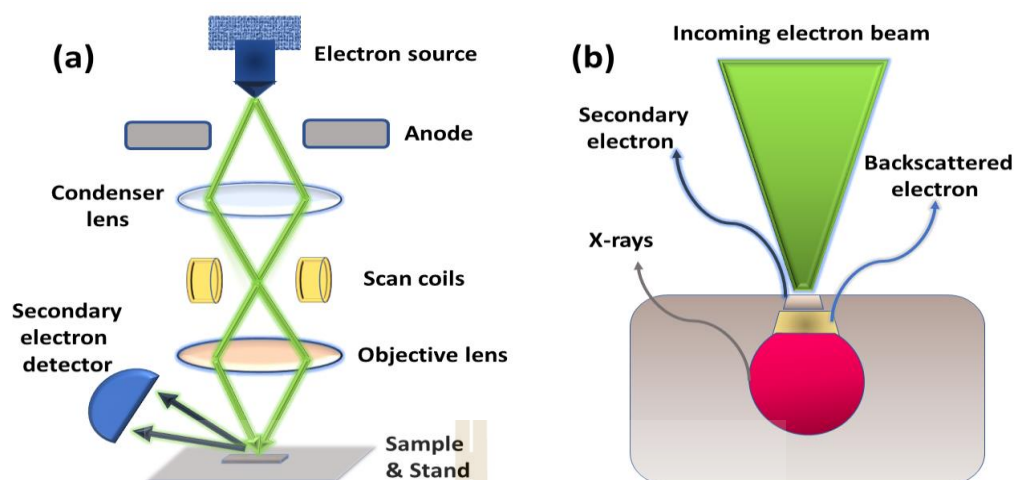


Figure 3.9 Schematic diagram of (a) basic SEM components and (b) different types of SEM signals.

In this study, SEM image were provided using SEM machine from Zeiss AURIGA FE-SEM/FIB/EDX located at SUT.



Figure 3.10 SEM machine (Zeiss AURIGA) located at SUT(<http://cste.sut.ac.th/>).

3.2.3 X-ray Absorptions Spectroscopy (XAS)

X-ray absorption spectroscopy (XAS) measures the energy-dependent fine structure of the X-ray absorption coefficient near the absorption edge of a particular element. From XAS principle, electron was ejected by x-ray source which enough energy for exciting. A typical XAS System is mainly divided into two parts simply input system and output system. Input is electron gas ionized signal at incident chamber (I_0). Output is electron ionized signal at transmitted chamber (I_t). The electron X-ray absorptions can be explaining by following equations:

$$\mu x = \ln(I_0/I_t) \quad (3.3)$$

Where: μ is transmission coefficient
 x is thickness of film
 I_0 is incident light intensity
 I_t is transmitted light intensity

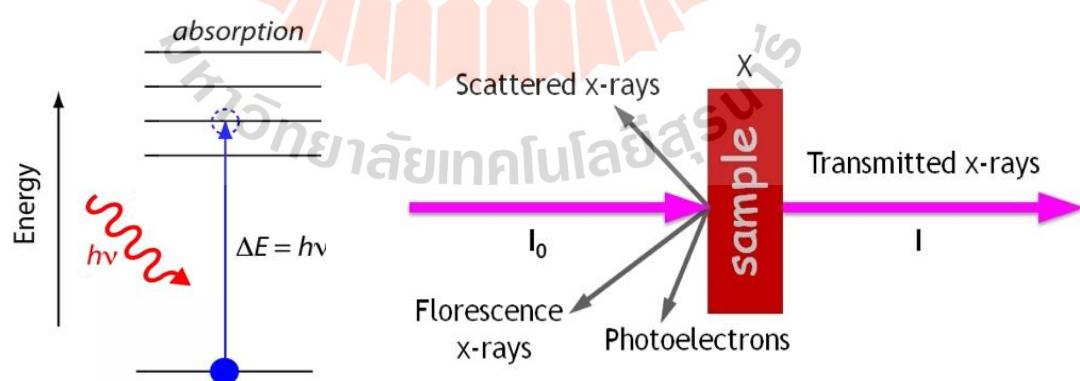


Figure 3.11 The principle for XAS spectra (BL-5.2 SLRI).

XAS with synchrotron radiation is used for studying the local structure of atomic material. This technique can be analysis chemical state, structure of considering atom, bond length, pattern of atom or type of neighboring atoms etc. XAS technique does not destroy the sample and can be applied in many researcher types. The XANES region can be explain the oxidations from edge-shift position and EXAFS explain the local structure.

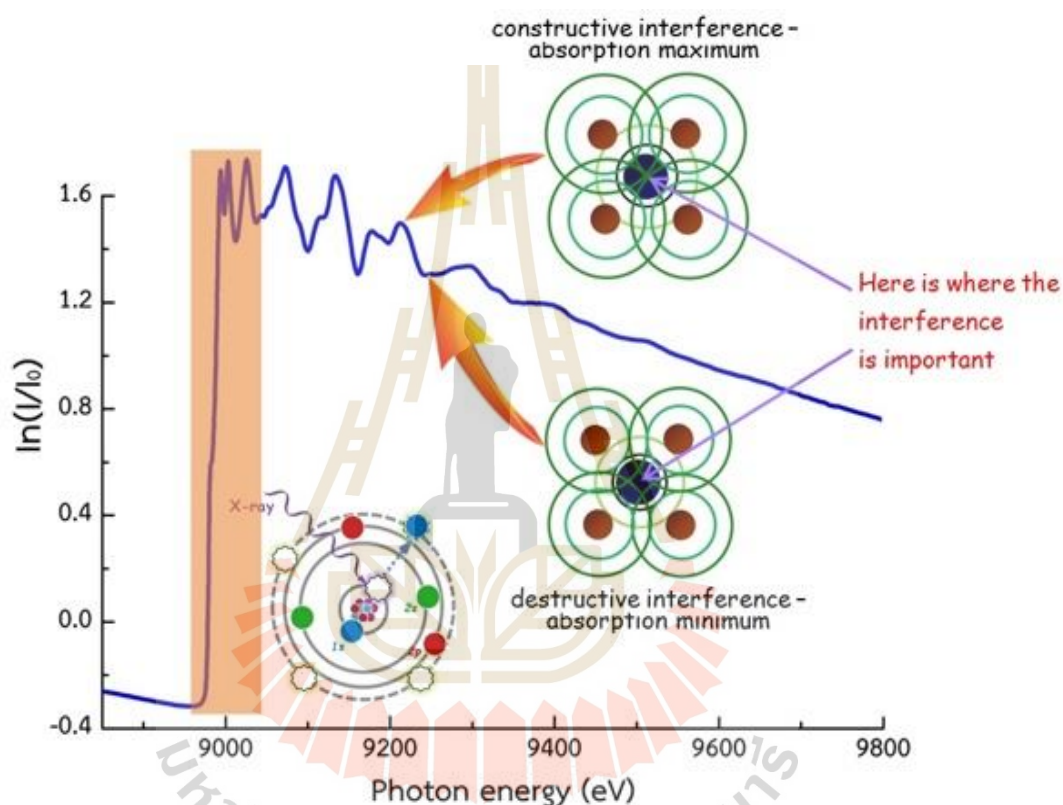


Figure 3.12 Theoretical and algorithm for XANES and EXAFS spectra (BL-5.2 SLRI).

The region very close to the absorption edge is characterized by transitions of the photoelectron to unoccupied bound states. XANES is therefore sensitive to the chemical bonding, exhibiting for example characteristic features for different oxidation states of the absorbing atom. The XANES features are also influenced by strong multiple scattering effects which depend on the three-dimensional geometry of the crystal structure. This provides a means of distinguishing between different crystal phases. Theoretical calculations of the fine structure in this region are complex and the accuracy of such simulations is still limited although significant progress has been made over recent years. Therefore, analysis typically compares the measured spectra

to those of known standards and quantifies the ratios by which these standards are present in the sample using linear combination fitting. Often, the XANES region is also referred to as the near edge X-ray absorption fine structure (NEXAFS) (Schnohr *et al.*, 2015).

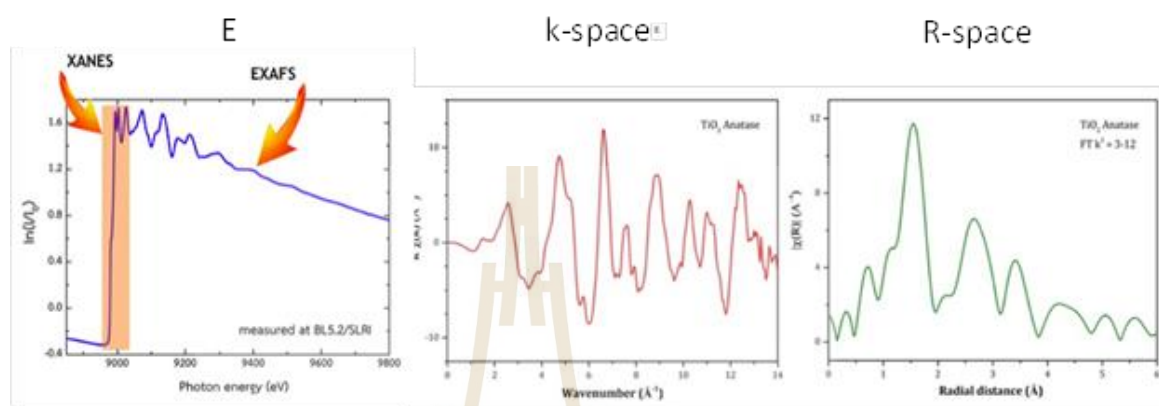


Figure 3.13 Energy range of (a) XANES and EXAFS spectra (b) K-space spectra and (c) R-space spectra (BL-5.2 SLRI).

For photon energies higher than $\sim 30\text{eV}$ above the edge, the photoelectron is promoted to a free or continuum state. EXAFS is thus independent of chemical bonding and depends on the atomic arrangement around the absorber. It contains information about the coordination number, interatomic distances and structural and thermal disorder around a particular atomic species. EXAFS does not require long-range order and is applicable to a wide range of ordered and disordered materials therefore providing a powerful tool for structural analysis. Theoretical calculations of the fine structure in the EXAFS region have also improved enormously during the last two decades and simulations with sufficient accuracy are now available. Nevertheless, the measurement of suitable standards still constitutes an important part of the experimental procedure (Schnohr *et al.*, 2015).

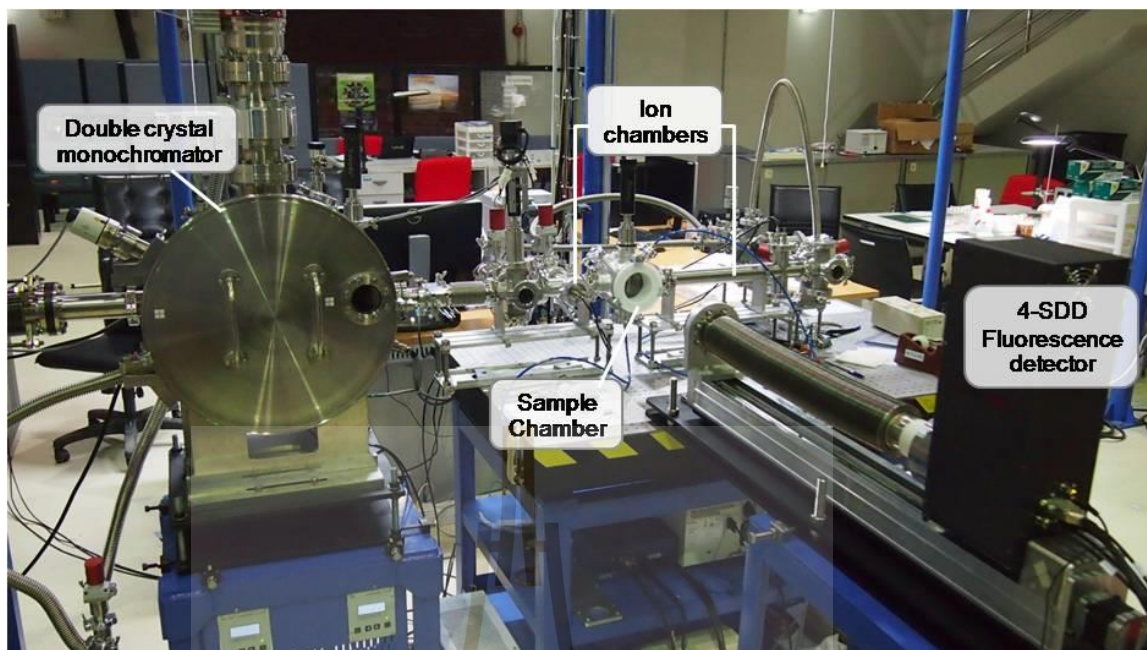


Figure 3.14 SUT-NANOTEC-SLRI beamline setup (BL5.2), SLRI.

3.2.4 UV-Vis-NIR spectroscopy

UV-Vis-NIR spectroscopy is a common, quantitative optical spectroscopic analysis technique which utilizes the absorption of optical radiation for studying the electronic transitions in molecules and solids. When electromagnetic radiations emitted by a light source in ultraviolet ($\lambda = 200\text{-}400\text{ nm}$), visible ($\lambda = 400\text{-}800\text{ nm}$) and near infrared ($\lambda = 800\text{-}2500\text{ nm}$) regions are absorbed by electrons in molecules, they undergo electronic transitions from valance energy level to higher energy levels in which process, the photons are destroyed. This results in optical absorption which depends upon the wavelength of the incident photon. The basic condition for absorption to occur is that the energy of the incident photon should be equal to or greater than the energy bandgap which obeys allowed transition. The absorbance (A) is given by the Beer- Lambert law as

$$A = -\log(I/I_0) = -\log(\%T) \quad (3.4)$$

Where I_0 and I are the intensities of light rays before and after passing through the sample, then the ratio (I / I_0) is called as transmittance.



Figure 3.15 UV-vis spectrophotometer at SUT (<http://cste.sut.ac.th/2014/?p=945>).

3.2.5 Spectroscopic ellipsometry

Spectroscopic ellipsometry, a nondestructive and noncontact optical technique, is an effective method for evaluating the thickness and optical constants of barrier layers during and after deposition. Ellipsometry studies the variations in the state of polarization of light resulting from its reflection off a surface. ellipsometry is sensitive to submonolayer surface covering due to the fact that variations are monitored rather than the absolute intensity of light. As a non-invasive and non-destructive technique, ellipsometry requires just a low-power light source and, as a result, does not interfere with the majority of processes, making it a useful instrument for in situ investigations (Gonçalves, D. *et al.*, 2002). Configuration in spectroscopic ellipsometry and schematic diagram of a polarizer-sample-rotating analyzer ellipsometer are shown in Figure 3.13 and 3.14 respectively. Spectroscopic ellipsometry detects the change in the polarization state of light when it is obliquely reflected off of a thin-film sample, as seen in Figure 3.13. This shift in polarization is represented at every wavelength by two parameters: Δ (phase difference), and Ψ (amplitude ratio). These two parameters are connected to the Fresnel reflection coefficients (r_p and r_s) for the sample according to the formula

$$\rho = \tan \Psi e^{i\Delta} = r_p / r_s \quad (3.5)$$

where r_p and r_s offer information about the optical constants of the sample.

In the case of a phase-modulated ellipsometer, which is the device used to gather the raw data presented below, the observed parameters I_s and I_c are linked to and as follows: $I_s = \sin 2\Psi \sin\Delta$ and $I_c = \sin 2\Psi \cos\Delta$. In order to examine and, or I_s and I_c data, a film structure-representative model must be developed. The sample's attributes, such as thickness and optical constants, may then be determined by using regression analysis to a model of the sample. Spectroscopic ellipsometry is useful for a variety of applications due to the fact that extra study of the optical constants can provide additional information about the sample, such as its composition, crystallinity, band gap, and roughness. Spectroscopic ellipsometry can be conducted either in situ or ex situ, depending on the sample or substance being investigated.

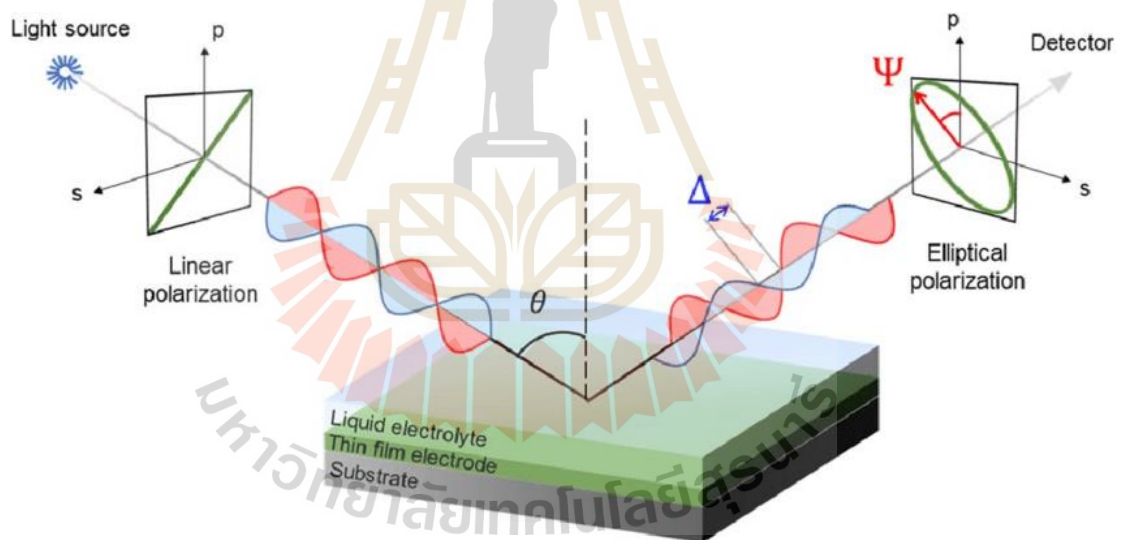


Figure 3.16 Configuration in spectroscopic ellipsometry for a determined incidence angle (θ , degrees). The changes of amplitude (Ψ , degrees) and phase (Δ , degrees) of the reflected elliptically polarized light are measured by the detector (Soult, M.C. *et al.*, 2022).

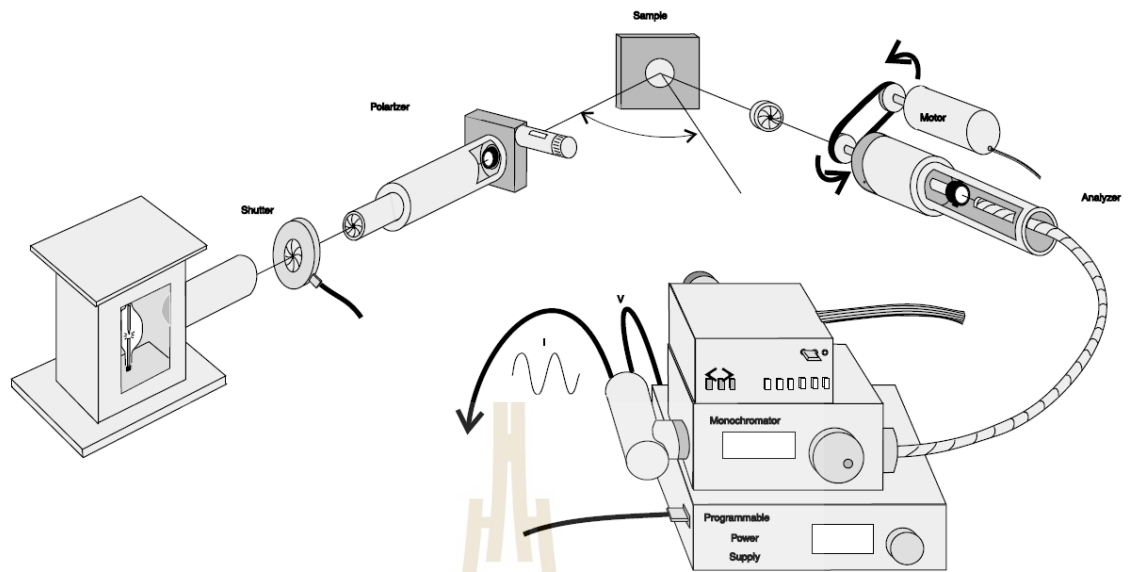


Figure 3.17 Schematic diagram of a polarizer-sample-rotating analyzer ellipsometer (Gonçalves, D. *et al.*, 2002).

CHAPTER IV

RESULTS AND DISCUSSION

4.1 TiO₂ thin films prepared by RF magnetron sputtering

Titanium oxide thin films were deposited on n-type Si (100) and glass substrates with using 99.9% pure TiO₂ ceramic target (diameter of 3 inches) by rf magnetron sputtering at BL 6, Synchrotron Light Research Institute (Public Organization); SLRI. The film deposition carries out at room temperature and the substrate–target distance is about 8 cm. Pure argon was used as the sputtering gas. Before each deposition, the sputtering chamber will be evacuated down to a pressure of 8.0×10^{-5} Pa (or lower). The 1.5 cm×1.5 cm substrates were firstly cleaned by plasma cleaner (diener electronic, Pico 300w) with O₂ gas for 20 min and then dried by pure N₂. The pre-sputtering process was done for 5 min to remove the unwanted oxide of the target surface. Firstly, in order to choose the operating power, the RF power was varied from 40 to 100 Watt with fixed working pressure.

The crystal structure was determined using the X-ray diffraction technique. An analytical method is X-ray diffraction. approach based on crystallized crystals and X-ray diffraction. It is employed to characterize the structural properties of various materials. The X-rays are diffracted by the orderly arrangement of atoms in crystals. A detector will record the diffraction patterns that are produced as a consequence. The refraction pattern is caused by the structural arrangement of atoms. The relationship between pattern and the atomic structure causes the scattering providing data on the crystal and chemical composition the physical characteristics and makeup of various materials. It might be also utilized for quantitative investigation of mineral and other combinations Crystallization stages. (Stabrawa, I. *et al.*, 2019)

In the case of thin layers with thicknesses in the nanoscale range, unfortunately, the XRD method has a limited sensitivity to the layer structure, hence this measurement technique provides insignificant information. This is due to the X-ray beam's passage within the object. This is due to the X-ray beam's passage within the object too short for conventional Bragg angles to produce X-ray reflections from the sample. An insufficient layer-to-substrate signal ratio is the issue.

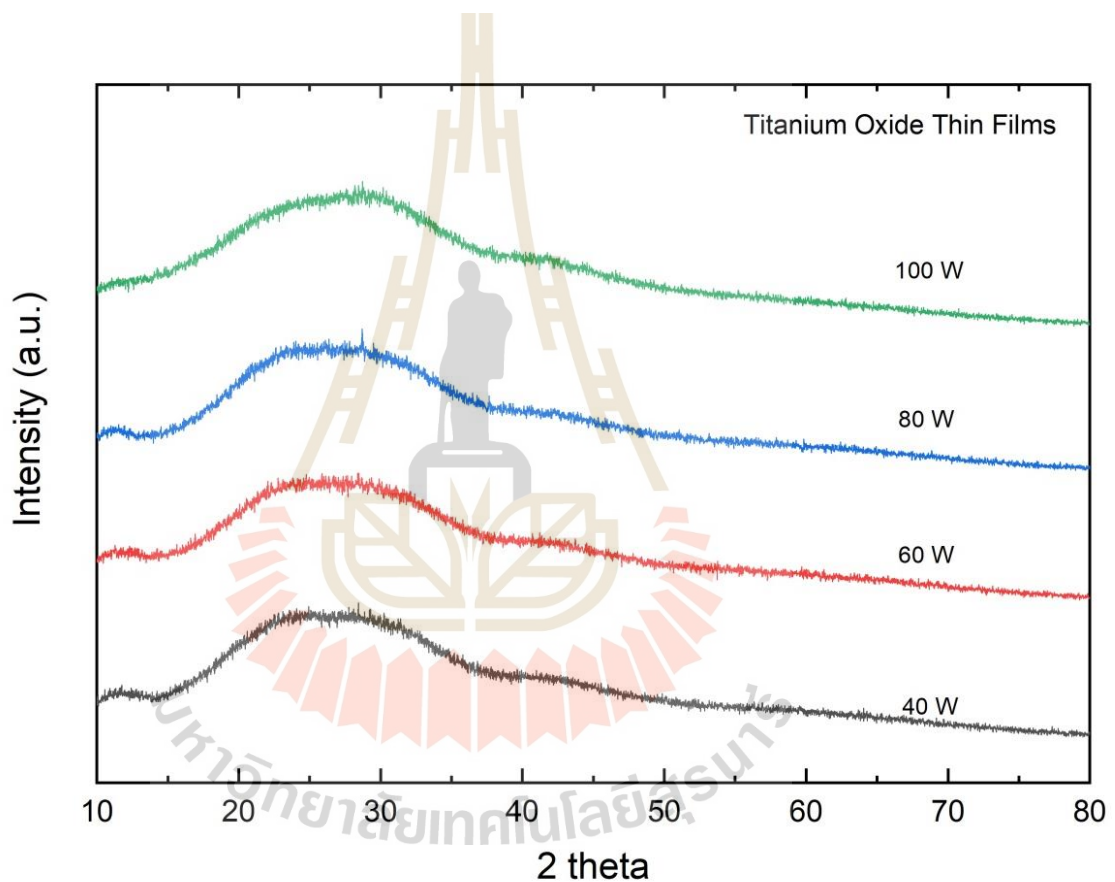


Figure 4.1 XRD results of the titanium oxide thin films with different power.

The XRD pattern of TiO_2 deposited by RF magnetron sputtering with different RF power shown in Figure 4.1 reveals the presence of amorphous structure in all samples. It is due to there is no peak indicating to TiO_2 structure. In Figure 4.1, the broad peak at 2θ around 26° was found which is the signal from substrate (glass slide).

After fabricating with various RF power, the power 60 W was chosen and working pressure is the subsequent variable preparation condition. The RF power was fixed at 60 watt and the deposition time for all condition was 4 h. During the sputtering process, the substrate holder was rotated with an unchanged speed. The working pressure was varied from 2.2 to 16.8 Pa. The prepared thin film microstructure has examined by x-ray diffraction (XRD, Bruker D2 Phaser) with scanning range from 20° to 80° . The surface morphology of the film samples was measured by FESEM (Zeiss, AURIGA). AFM (Park Systems, AFM XE-120) was used to analyze the surface topography of the samples at room temperature. Optical properties were investigated by UV-visible spectrophotometer at room temperature and spectroscopic ellipsometry. The XRD, AFM, UV-Vis measurements were done at The Center for Scientific and Technological Equipment (CSTE), Suranaree university of technology and spectroscopic ellipsometry at Thailand's National Electronics and Computer Technology Center (NECTEC). Moreover, the local structure was measured at Ti K-edge by XANES and EXAFS in fluorescence mode at SUT-NANOTEC-SLRI beamline (BL5.2), SLRI. XANES data was analyzed by ATHENA software package.

SEM and AFM images of the titanium oxide thin films with different working pressure are shown shown in Figure 4.2. The SEM images of all samples except 2.2 Pa reveal the smooth surface which is confirmed by AFM results (Figure. 4.2 right). For 2.2 Pa sample, the particles with a size smaller than 5 nm were distributed across the surface.

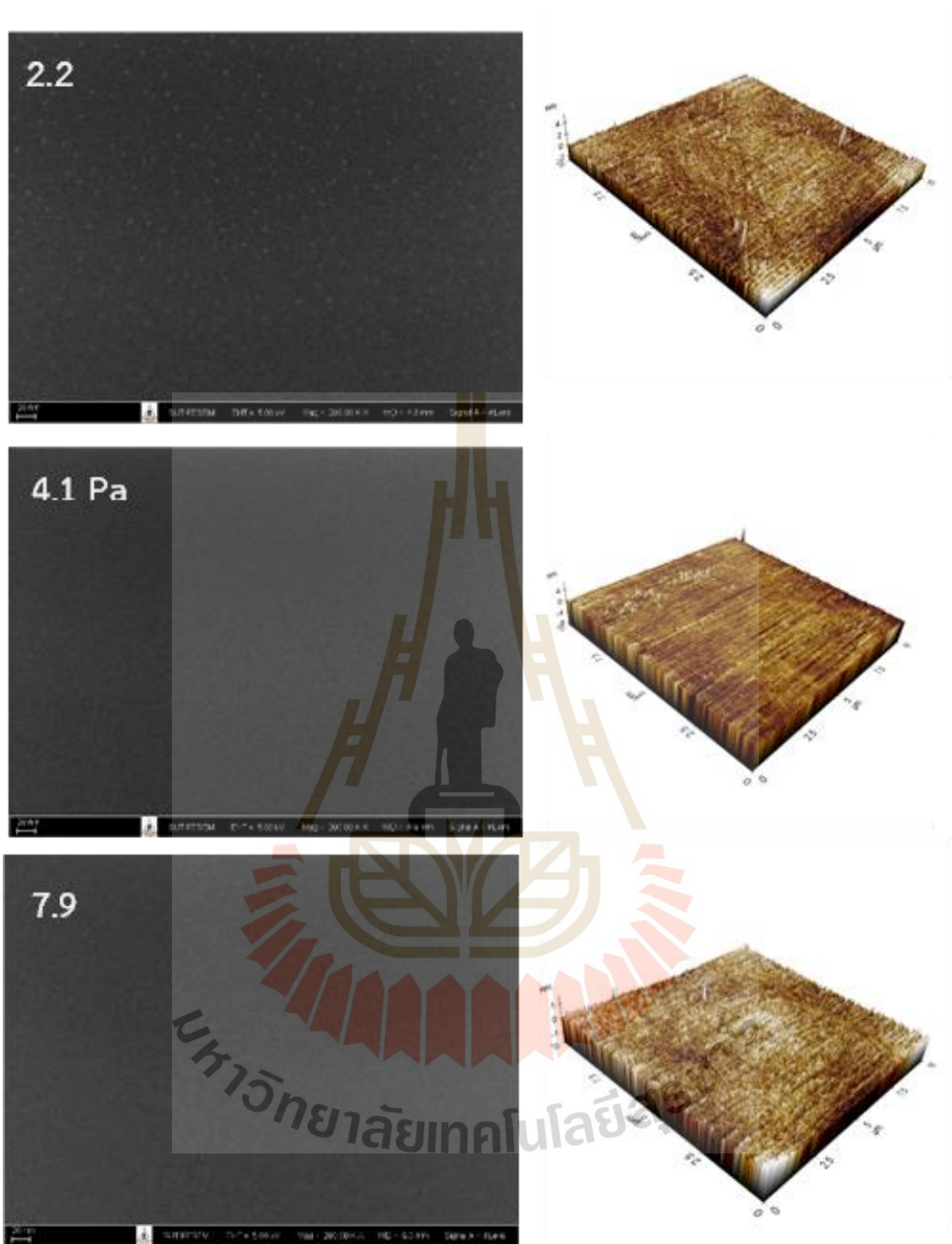


Figure 4.2 SEM (left) and AFM (right) images of the titanium oxide thin films with different working pressure.

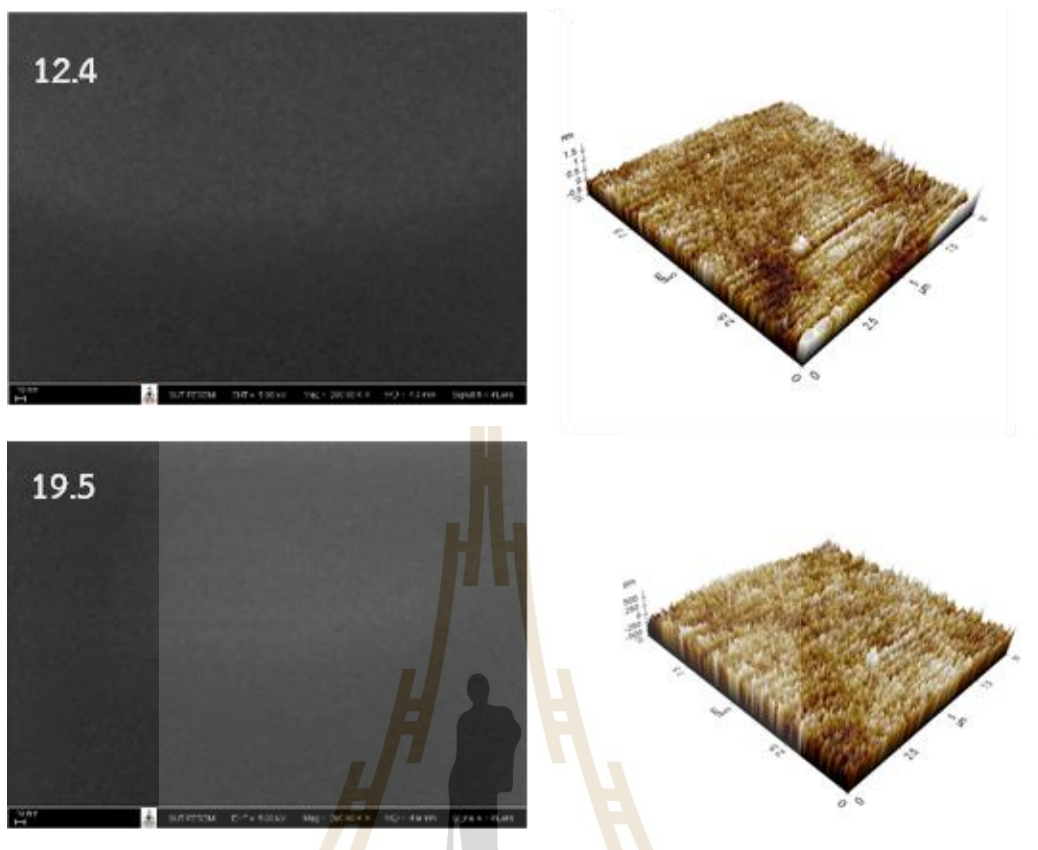


Figure 4.2 (Continued) SEM (left) and AFM (right) images of the titanium oxide thin films with different working pressure.

Measurements of spectral transmittance and ellipsometry were made to associate the variations in the films' stoichiometry and crystallinity with their optical characteristics. For samples from the various sputtering pressure, Figure 4.3 displays the transmittance spectra of the films that were deposited on glass substrates. All samples exhibit a high transmittance ($> 85\%$ T) in the visible and near IR region. The transmittance tended to decrease as the working pressure increases except for 2.2 Pa sample.

Generally, amorphous films have a lower index of refraction than crystalline films. Rutile structure has the greatest refractive index among all TiO_2 phases due to its greater density. In Figure 4.4, the spectral refractive indexes of all samples obtained from ellipsometry measurement are presented. Besides, the refractive indices at 550

nm wavelength were 1.64, 2.00, 1.95, 1.54 and 1.50 for the samples with sputtering pressure at 2.2, 4.1, 7.9, 12.4 and 19.5 respectively.

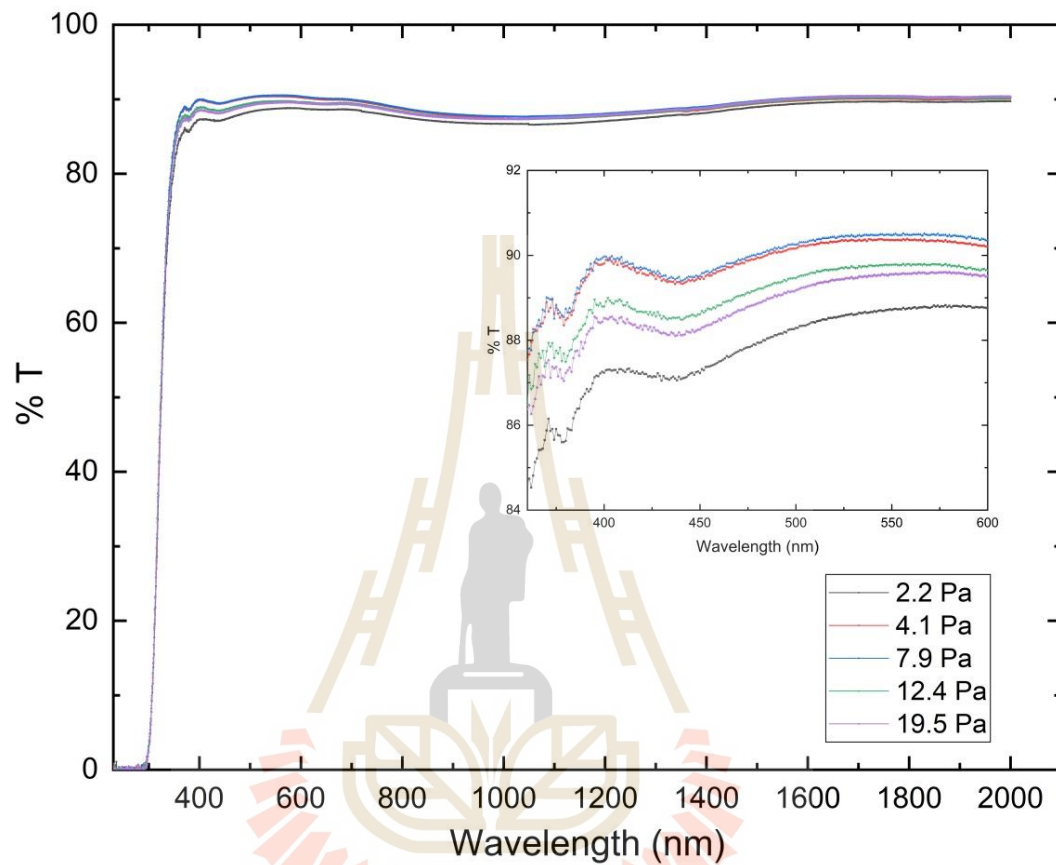


Figure 4.3 Optical transmittance of the titanium oxide thin films deposited on glass with different working pressure.

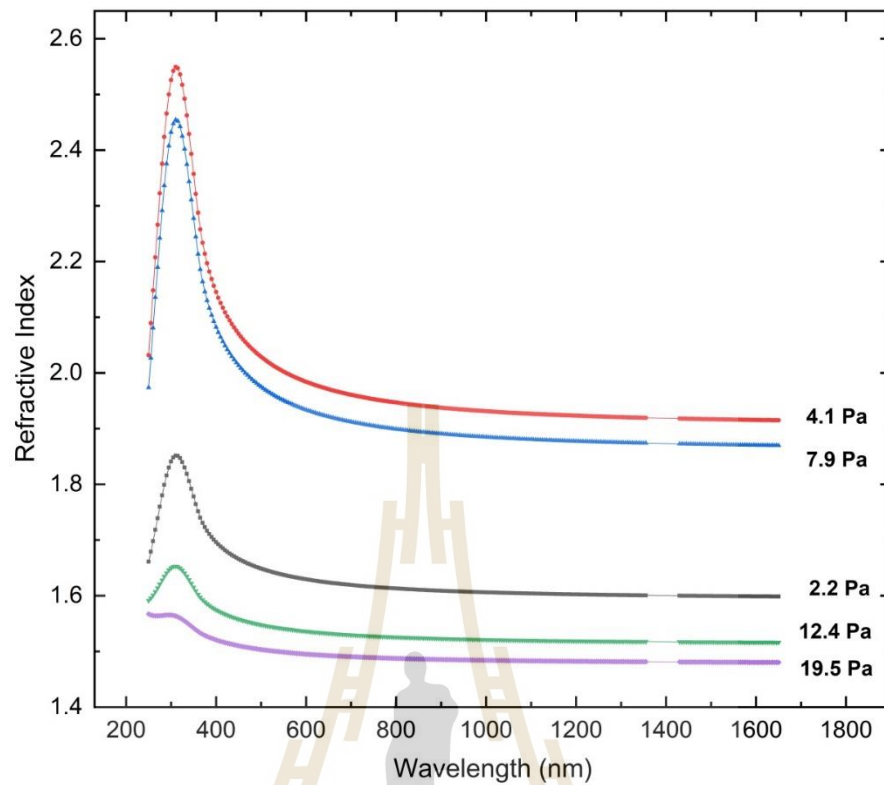


Figure 4.4 Refractive index in the 250–1650 nm wavelength range for the titanium oxide thin films with different working pressure.

Table 4.1 Thickness of TiO₂ thin films prepared by RF magnetron sputtering at different working pressure.

sample	thickness (nm)
sample1_60W_2.2	3.15
sample2_60W_4.1	2.78
sample3_60W_7.9	2.22
sample4_60W_12.4	2.86
sample5_60W_19.5	2.83

The thickness of a single-layer film can be examined by using spectroscopic ellipsometry. The thickness of TiO₂ thin films prepared by RF magnetron sputtering at different working pressure is shown in table 4.1. The thickness of all films is less than 5 nm. Therefore, the greatest deposition rate (for the condition with 2.2 Pa) is only about 0.013 nm/min. To produce TiO₂ thin films with this technique and condition, it is not suitable due to the limitation of the deposition rate. Since the thickness of all films is extremely small, so, the XRD spectra in Figure 4.1 shows only the signal from substrate.

The Ti K-edge XANES spectra of the titanium oxide thin films with different working pressure is presented in Figure 4.5. The XANES features of the above prepared thin films were compared with the standard spectra of Ti foil, rutile and anatase TiO₂. In principle, X-ray absorption spectrum is widely divided into three different regions: pre-edge, edge, and post-edge. Basically, it has been known that thinner samples create a sharper absorption step and a fast-declining tail (Sahoo, M. *et al.*, 2015). In Figure 4.5, the sharp absorption step and a rapidly decaying tail are observed for all samples indicating that all specimen is thin layer. It is known that XANES carry information on the local symmetry and co-ordination number surrounding the core metal atom whose K-edge is being investigated. Since X-ray absorption spectra are frequently defined in terms of scattering events, it has been conclusively shown in the scientific literature that multi scattering events dominate the pre-edge area and single scattering events dominate the extended region of X-ray absorption spectra. In the review of Takashi Yamamoto, the influence of local symmetry on the assignment of pre-edge peaks has thoroughly described (Takashi Yamamoto, 2008). The spectra of Ti foil, anatase and rutile are obviously different. For the anatase structure, the three pre-edge peaks transitions but only two pre-edge peaks are noticed. Anatase's spectrum has two prominent peaks at around 4984 and 5004 eV, while rutile's spectrum has three prominent peaks at 4987, 4992, and 5004 eV. This is well consistent with the literatures (Zhang, H. *et al.*, 2008 and Kurenkova, A. Y. *et al.*, 2020). The white line seen above the edge in this investigation is indicative of the mixed phase between rutile and anatase phase.

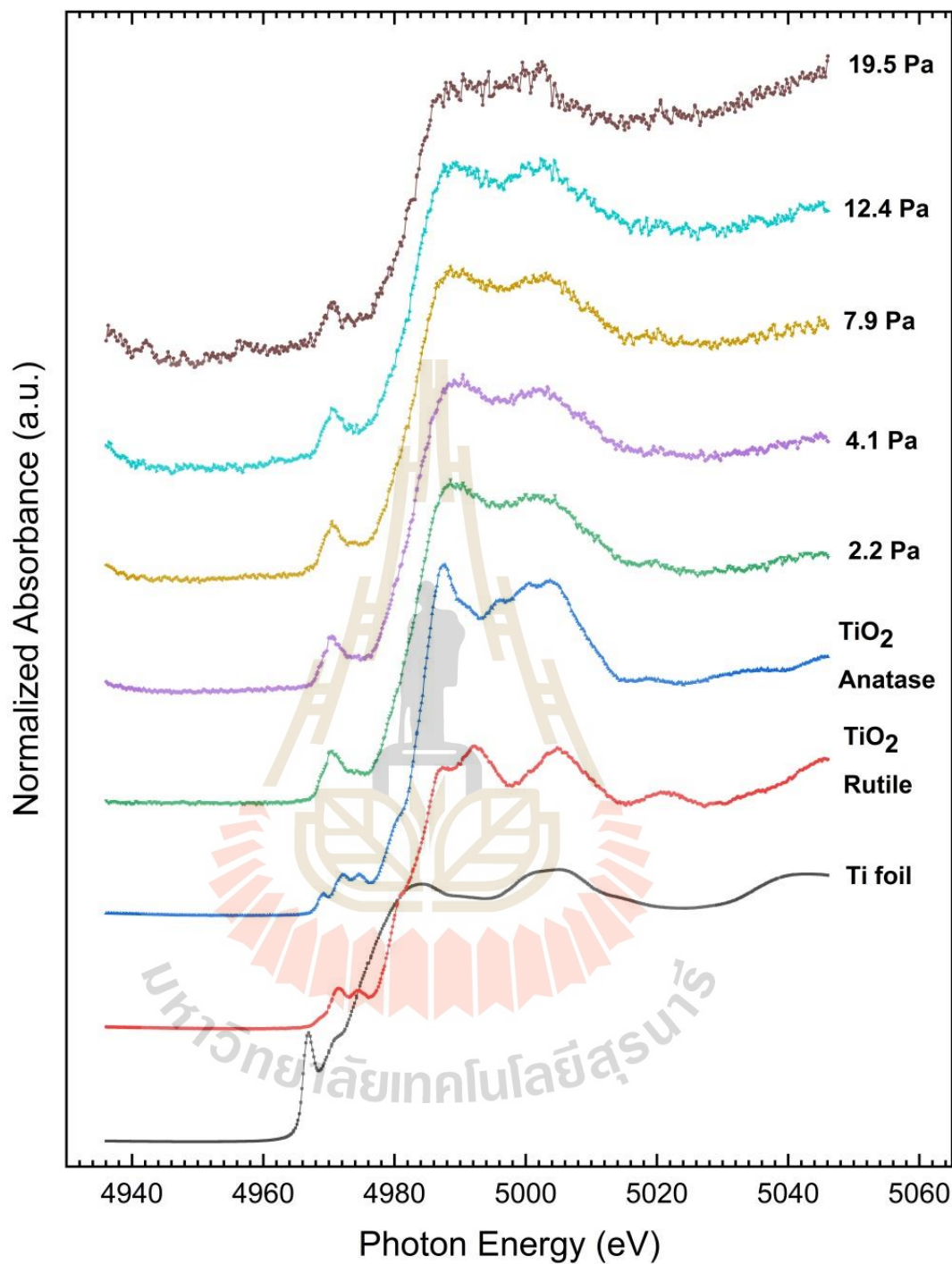


Figure 4.5 XANES spectra of the titanium oxide thin films with different working pressure compared with the standard spectra of Ti foil, rutile and anatase TiO_2 .

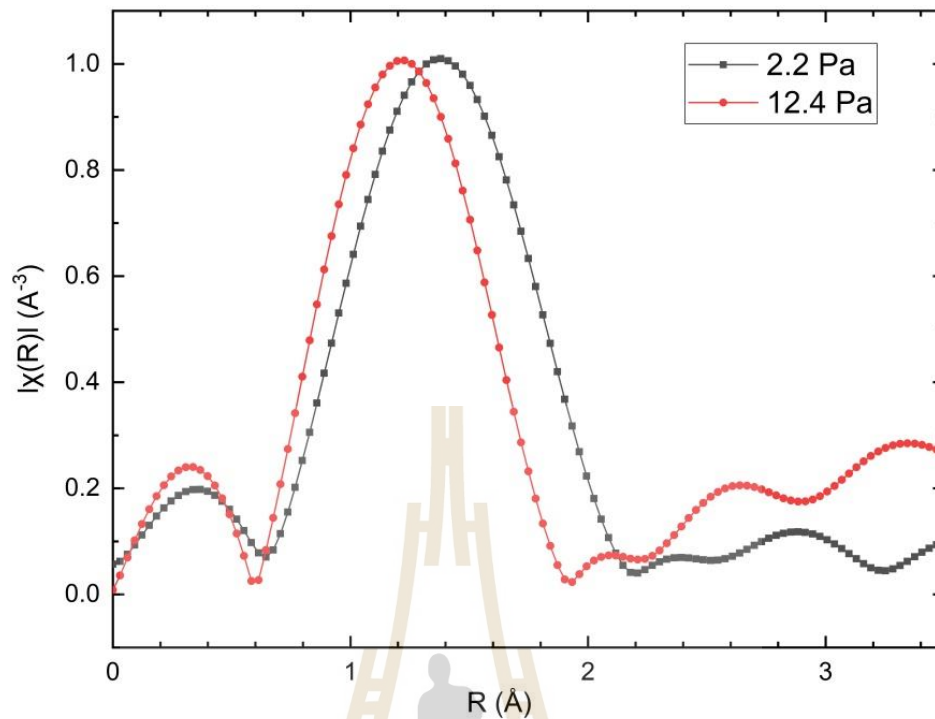


Figure 4.6 EXAFS spectra fitted using ARTEMIS in R-space of the titanium oxide thin films with working pressure of 2.2 and 12.4 Pa.

The co-ordination number and radial distances of the atoms in various co-ordination spheres are then calculated using (R) versus R (radial distances) plots. The fitted plots of EXAFS data in the R-space fitted using ARTEMIS of the titanium oxide thin films with working pressure of 2.2 and 12.4 Pa are present in Figure 4.6. The real space fittings were carried out between 0 and 3.5 Å. Ti-O coordination is responsible for the first peak at 1.22 and 1.37 (for 2.2 Pa and 12.4 Pa respectively) in the Fourier transform spectrum is shown in Figure 4.6. Additionally, it indicates that the bond length of the lower working pressure sample is greater than that of higher.

Due to the restriction of the deposition rate, this sputtering system and these conditions are unsuitable for the production of TiO_2 thin films. New technique is need to be used to fabricate thin layer with good deposition rate. The reactive gas-timing (RGT) approach has been introduced as an appropriate technique for metal oxide thin film deposition using an RF-reactive sputtering system. During deposition, the energy per atom and reactivity of reactive gases such as O_2 can be increased by halting the gas supply for a sequence period. By adjusting the pause period, the film's composition

may be fine-tuned (Lertvanithphol, T. *et al.*, 2019). It has been added to traditional reactive sputtering deposition to enhance the capacity to regulate structural and optical characteristics in certain metal oxynitride compounds and to facilitate crystalline development at low substrate temperature (Boonkoom, T. *et al.*, 2015).

4.2 TiO₂ thin films fabricated by Reactive Gas Timing (RGT) magnetron sputtering

TiO₂ single layer thin film samples were deposited on a silicon wafer (100) and glass substrate using Reactive Gas Timing (RGT) DC magnetron sputtering equipment (AJA international, Inc.; ATC 2000-F). Argon with a high level of purity (99.999 percent) and oxygen (99.999 percent) were added to the chamber as sputtering and reacting gases, respectively, into the chamber. Two inches of diameter Titanium metal target (Kert J. Lesker) was placed at a distance of 90 mm from the substrate. Before deposition, the pressure in the deposition chamber was reduced to 1×10^{-6} Pa using mechanical pump (ALCATEL) and then turbomolecular pump (Shimazu, TMP-803-LM). Furthermore, the silicon substrate underwent a 10-minute cleaning process using argon plasma to eradicate any surface impurities. Additionally, the Ta target was pre-sputtered in an argon plasma environment to erase an excessive coating of oxide on its surface. The power employed during the deposition process remained constant at 100 watts. Furthermore, the partial pressures of all gases were around 1.25 millitorr. Titanium dioxide (TiO₂) thin films were fabricated utilizing two different methods: reactive gas-timing (RGT) and standard reactive sputtering. The procedures for creating these films are given below. By employing the RGT approach, the influx of O₂ into the chamber oscillated during the deposition process, but the flow rate of Ar remained consistent. The oxygen flow timing was adjusted at intervals of 3, 27, and 57 seconds, while the pause duration for oxygen flow remained constant at 3 seconds. During the deposition process, the working pressure consistently maintained a nearly constant value of 0.3 Pa. The name "CONV" sample denotes thin films of TiO₂ that are fabricated using typical reactive sputtering deposition technique. The GT 57-3s sample pertains to the films that were created by depositing them with an oxygen flow length of 57

seconds and a switching stop oxygen flow duration of 3 seconds. The crystallinity of the produced films was assessed by employing grazing-incidence X-ray diffraction (GIXRD) with a Rigaku Ttrax III instrument. The analysis was conducted within the 2θ range of 20° – 70° , with intervals of 0.02° . The structural property was investigated using Raman spectroscopy (the Thermo Scientific DXR Smart Raman). The X-ray absorption near-edge structure (XANES) and extended X-ray absorption fine structure (EXAFS) measurements were conducted in fluorescence mode at the SUT-NANOTEC-SLRI XAS Beamline (BL5.2) at the Synchrotron Light Research Institute (Public Organization) in Thailand. The Ti K-edge XAS data were normalized, processed, and analyzed by eliminating the background using the ATHENA and ARTEMIS tool, which is part of the IFEFFIT package. The EXAFS data was used to fit models developed from the FEFF program in order to obtain detailed information about the local structure around the titanium atoms.

Figure 4.7 shows cross-sectional SEM images of TiO_2 thin films deposited using conventional and RGT technique with different oxygen flow timing. The thickness of all sample is around 100 nm. As shown in Figure 4.7, the morphology of all films is noticeably nano-column shape. The untill column structure for conv samples is well arranged and perpendicular but the others have not well columnar arrangement. It means that RGT technique affect to structural formation of thin films.

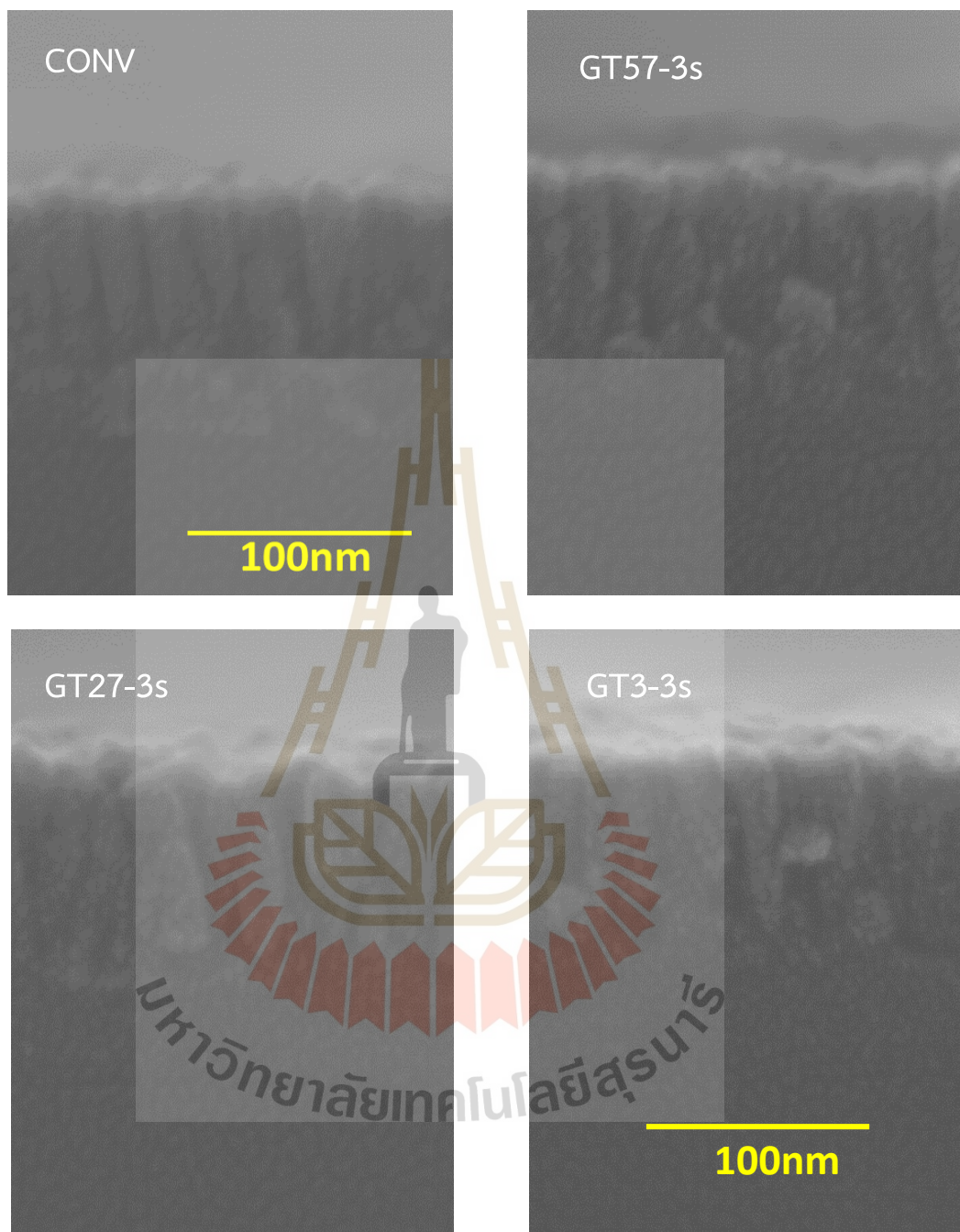


Figure 4.7 Cross-sectional and Top-view SEM images of the titanium oxide thin films with oxygen flow timing.

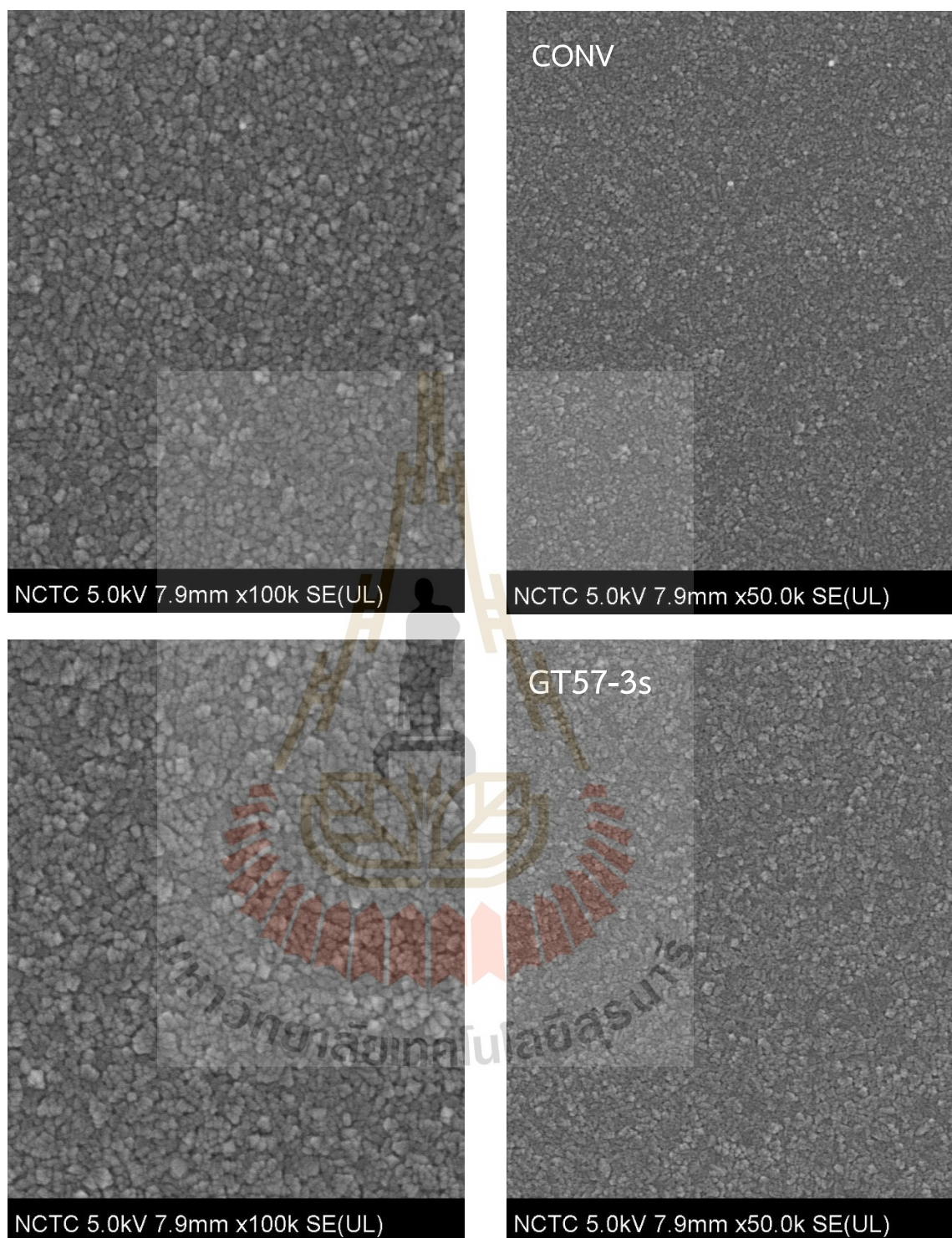


Figure 4.7 (Continued) Cross-sectional and Top-view SEM images of the titanium oxide thin films with oxygen flow timing.

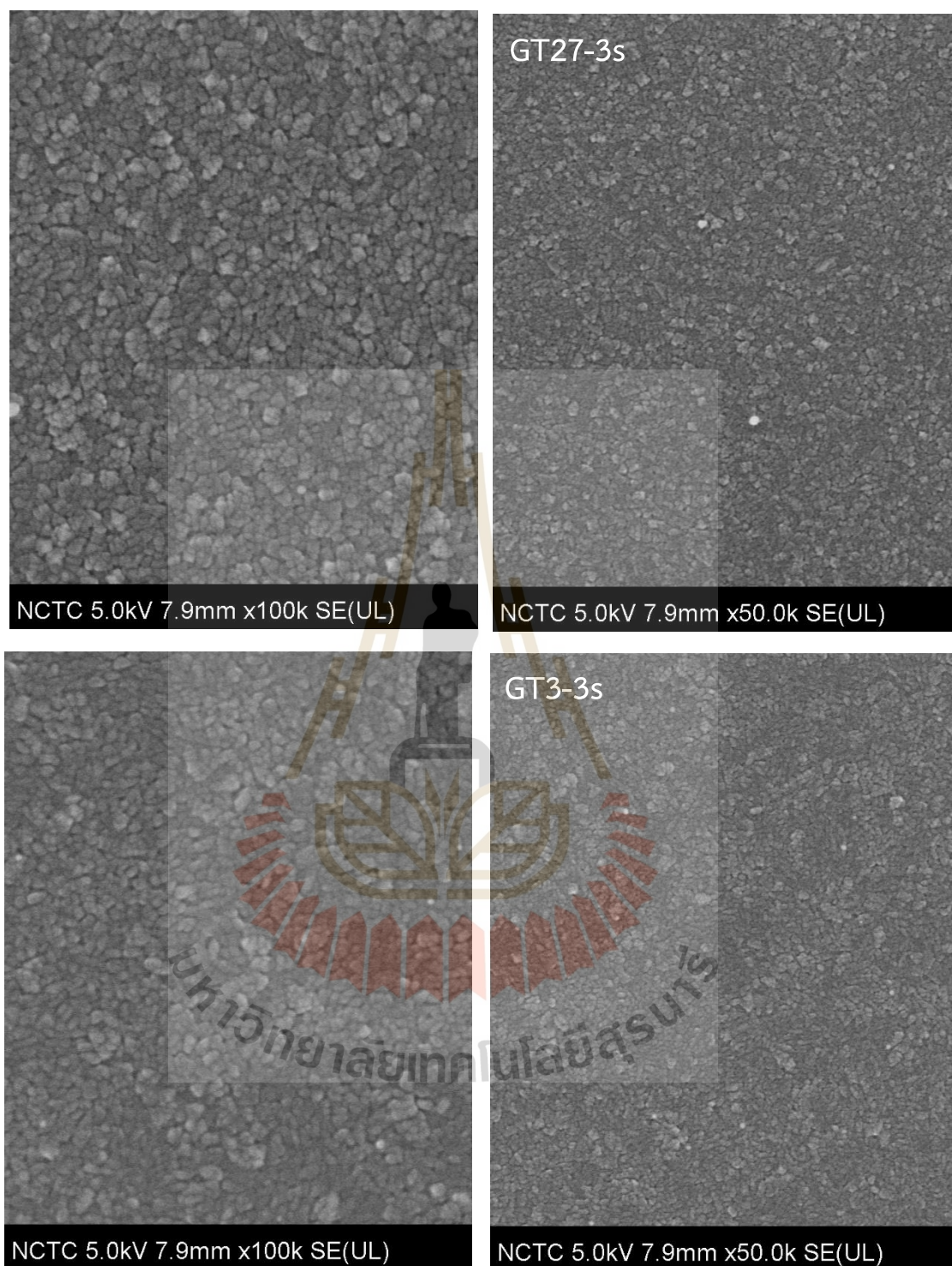


Figure 4.7 (Continued) Cross-sectional and Top-view SEM images of the titanium oxide thin films with oxygen flow timing.

Figure 4.8 is a plot of %T as a function of wavelength. The deposited thin films are highly transparent and colorless. The blank glass slide was used as a reference, having the highest average transmittance percentage (90%) throughout visible range. The transmittance spectra of the RGT samples are obviously different from the spectrum of uncoated glass slide in term of edge position and feature of transmittance spectrum. The oscillations in the transmittance spectra are present in all RGT samples. The transmittance spectra over the entire visible range for all RGT films have good agreement with the published literature (Kang, M. *et al.*, 2018). The maximum transmittance spectra of the shorter oxygen flow timing show a red shift. The highest transmission band edge can be estimated to be 330 nm approximately. The maximum transmittance peaks of conventional, GT 57-3s, GT 27-3s and GT 3-3s films are around 475, 530, 560 and 596 nm respectively and the highest light transmittance value is \sim %96. When placed as a single layer of TiO_2 , all of the examined metal oxides reduced the optical transmittance of undeposited glass. This was expected given that the refractive indices of these oxides are greater than that of the glass.

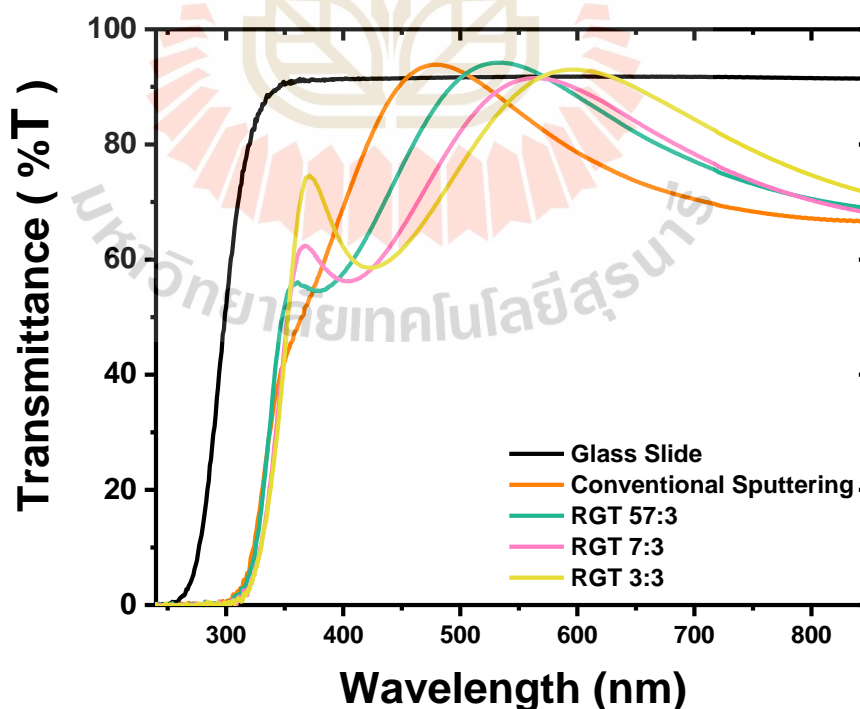


Figure 4.8 Optical transmittance of the titanium oxide thin films with different oxygen duty cycle.

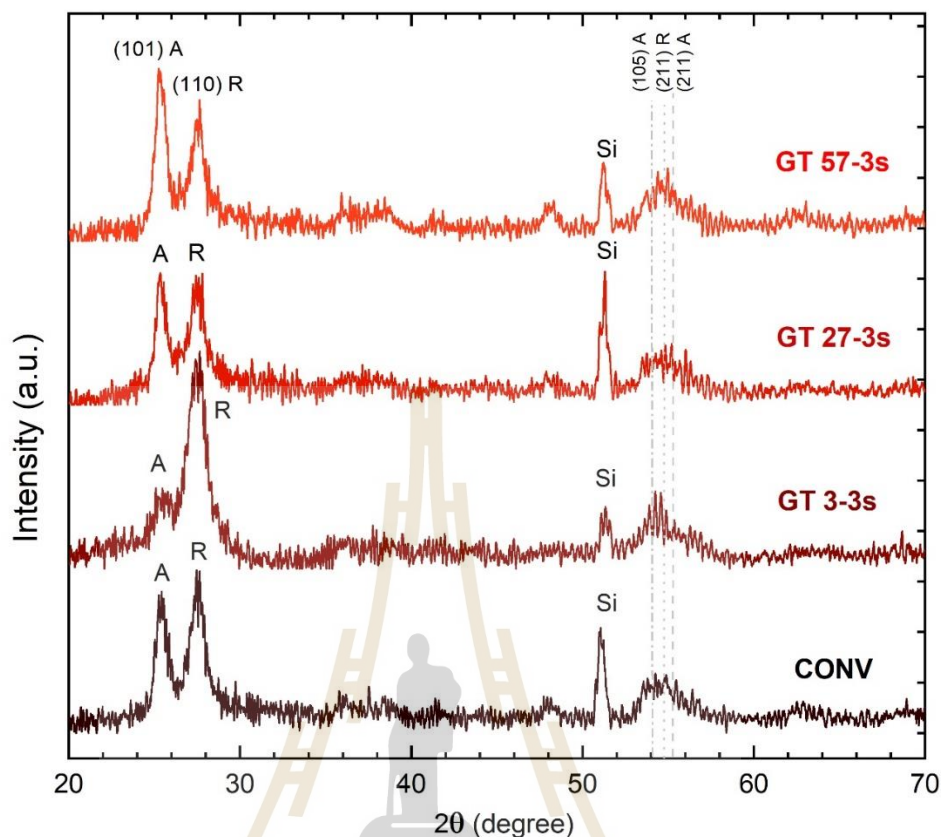


Figure 4.9 GIXRD results of the Titanium Oxide thin films shows the variation of anatase/rutile ratio depending with different duty cycle of oxygen gas.

Figure 4.9 illustrates the GIXRD patterns of the Titanium Oxide thin films fabricated by conventional and RGT technique with different gas-timing sequence conditions. Two prominent peaks corresponding to the rutile and anatase crystalline phases of TiO_2 are seen. The diffraction pattern of all films exhibits a composite structure consisting of both anatase and rutile phases. The intensity of the anatase and rutile peaks is found to be dependent on the preparation condition. The rutile phase is the predominant phase in the conv., GT27-3s, and GT 3-3s films. For only GT 57-3s sample, the structure has anatase phase being dominant with a preferred orientation along (101) direction. Considering with the aforementioned UV-vis result, the transmittance of TiO_2 thin films is sensitive to slight variation in the stoichiometry of films. In addition, Raman spectroscopy was employed to further analyze the phase distribution of anatase and rutile on the surface of the film. According to the data

presented in Figure 4.10, all samples showed the presence of Raman bands associated with both the rutile and anatase phases. The Raman analysis supports the XRD analysis, indicating that the films that were created consist of a combination of rutile and anatase phases. The Raman-active modes of the anatase phase may be observed at a frequency of 140 cm^{-1} , which corresponds to the E_g vibration mode (Wang *et al.*, 2008, Choi *et al.*, 2005). Furthermore, Figure 4.10 displays the presence of rutile bands at around 435 and 616 cm^{-1} (Savio *et al.*, 2012). As seen in Figure 4.10, the Raman spectra of the film exhibit a significant peak at 520 cm^{-1} , accompanied by a smaller feature at 300 cm^{-1} , both of which suggest the presence of the silicon substrate (Carta *et al.*, 2015).

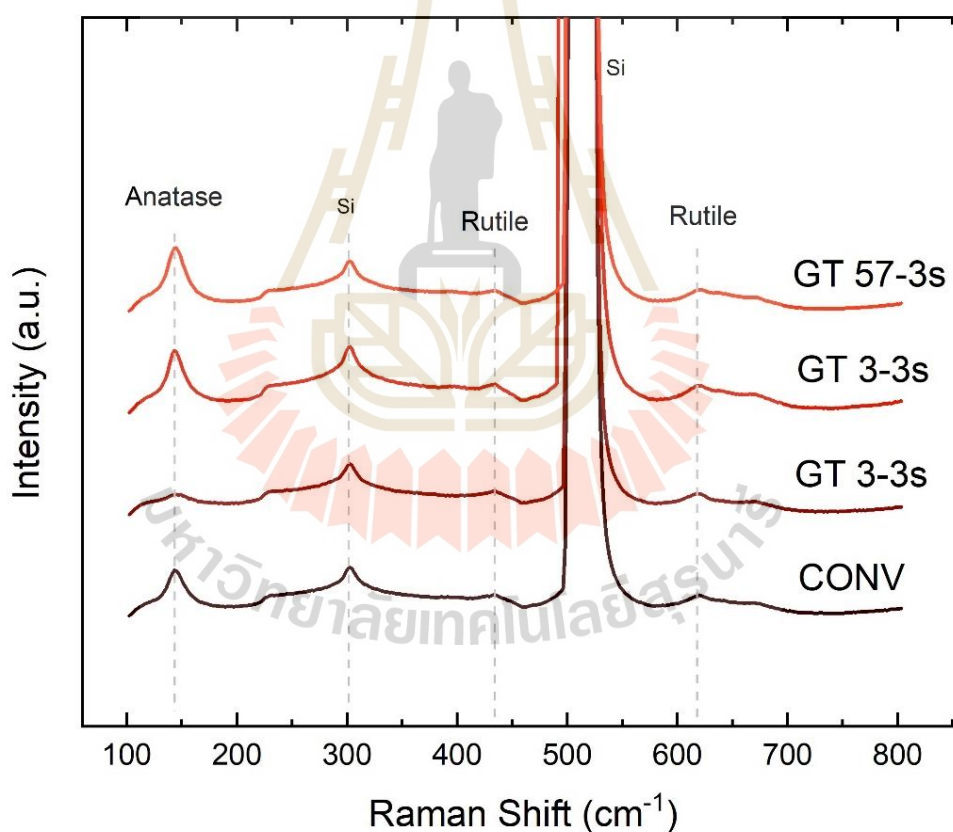


Figure 4.10 Raman results of the Titanium Oxide thin films with different oxygen timing sequence.

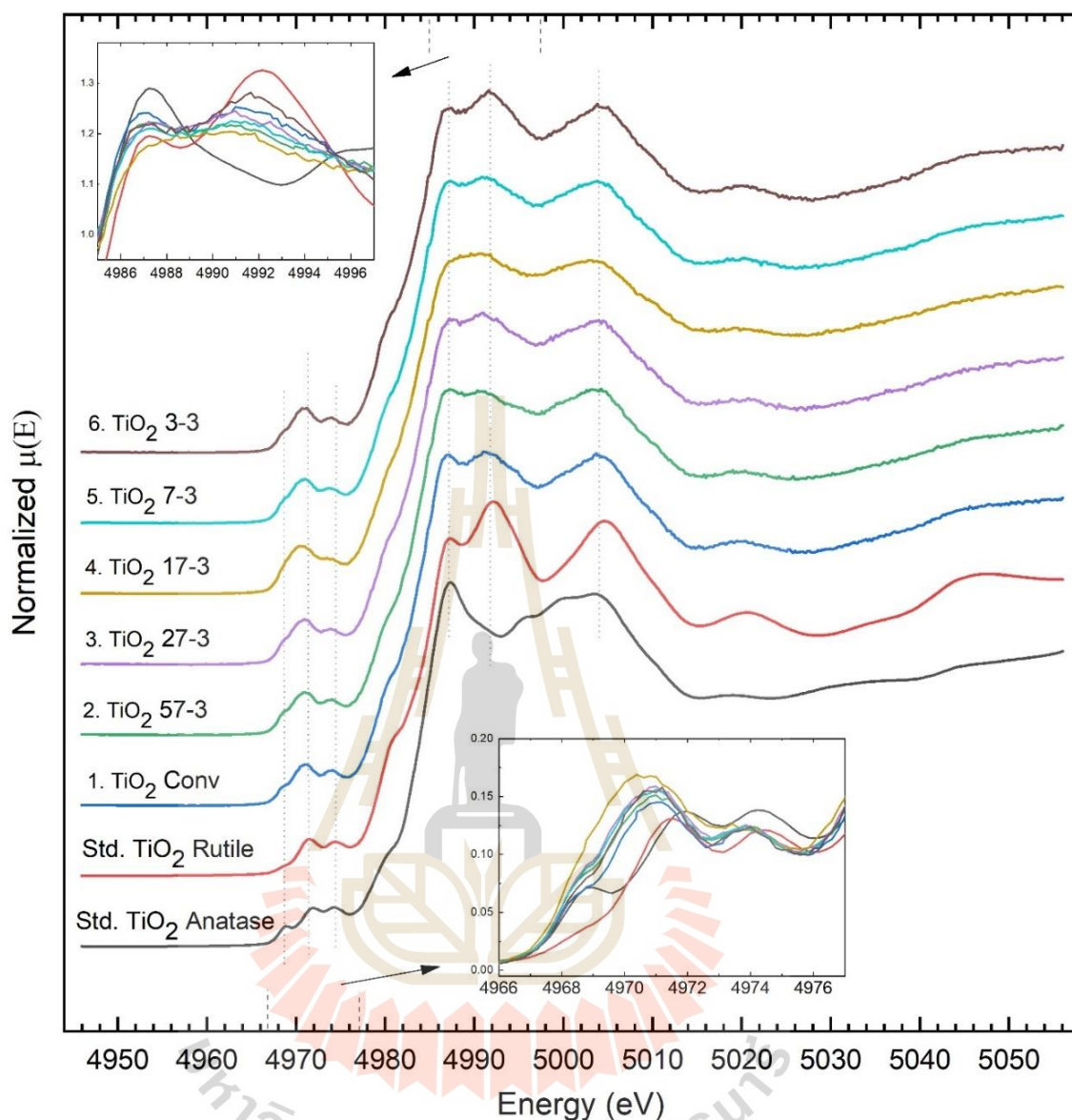


Figure 4.11 The normalized Ti K-edge XANES spectra of TiO_2 thin films prepared by conventional reactive and RGT technique at different oxygen flow timing (the enlarged view of spectra in pre-edge and white line regions showed in inset).

Figure 4.11 displays the normalized Ti K-edge XANES spectra obtained from TiO_2 thin films made using both traditional reactive and RGT techniques. The spectra were taken at room temperature and include varied oxygen timing sequences, as well as reference samples of standard rutile and anatase TiO_2 . X-ray Absorption Near Edge Structure (XANES) is not only sensitive to the oxidation state of individual atoms, but

also to the immediate chemical environment around these atoms. The distinction between the spectra of anatase and rutile is widely recognized. The XANES analysis validates that the anatase spectrum exhibits two distinct peaks, while the rutile spectrum displays three distinct peaks. Figure 4.11 has an inset that shows a magnified picture of the spectra in the pre-edge and white line areas. The XANES spectral feature is regarded as an intermediary characteristic situated between anatase and rutile. The presence of both the pre-edge and white line in the XANES spectra of all samples indicates a mixing of the rutile-anatase phase. This finding is consistent with previous XRD and Raman analyses (Kim *et al.*, 2000, Matsuo *et al.*, 2005). The features and placement of the shoulder's rising edge for all samples are nearly indistinguishable. The characteristics appear to resemble rutile more than anatase. However, all spectra exhibit very similar features, making it challenging to assess them based on their spectral properties. This suggests that titanium has a relatively comparable electronic state in all compounds. Linear combination fitting (LCF) is the most straightforward and effective approach for processing XANES data. The LCF technique involves creating unknown spectra by modeling the X-ray absorption spectrum using a linear combination of known species. The ratios of anatase to rutile, determined using the LCF approach, are presented in Table 4.2. The Ti K-edge XANES spectra of TiO₂ thin films in this investigation were accurately represented by a linear combination of anatase and rutile spectra. The weight percentage of the anatase phase ranges from 28% for the TiO₂ GT3-3s sample to 55% for the TiO₂ GT57-3s sample. In contrast, the percentage of rutile phase varies from 45% for the TiO₂ GT57-3s sample to 72% for the TiO₂ GT3-3s sample. The findings indicate that only the GT 57-3s condition exhibits a structure mostly composed of the anatase phase, whereas the other conditions have a greater proportion of rutile content. The XANES result is consistent with the previously described XRD finding for the proportion of anatase and rutile. When the gas-timing ratio is altered, there is a considerable shift in the phase composition of TiO₂ films (Boonkoom *et al.*, 2015).

Table 4.2 Weight of TiO₂ Anatase and Rutile in TiO₂ thin films with different oxygen flow timing and R-factor obtained from the linear combination fitting of XANES data.

Sample	R-factor	Weight of TiO ₂ Anatase	Weight of TiO ₂ Rutile
TiO ₂ conv	0.004065	0.4389	0.5611
TiO ₂ 57-3	0.004573	0.5492	0.4508
TiO ₂ 27-3	0.005902	0.4495	0.5505
TiO ₂ 17-3	0.009895	0.4809	0.5191
TiO ₂ 7-3	0.005327	0.4603	0.5397
TiO ₂ 3-3	0.005775	0.2823	0.7177

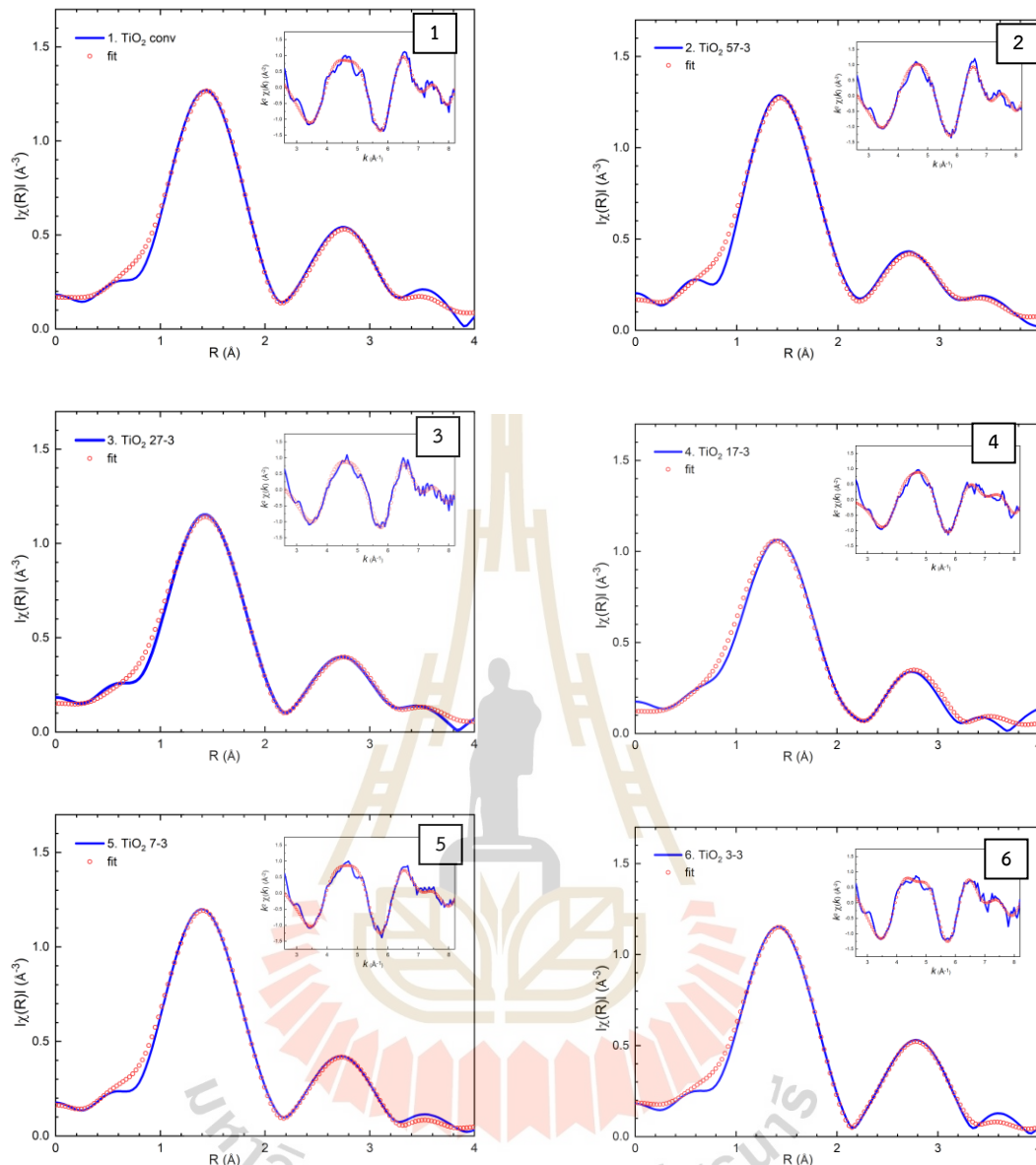


Figure 4.12 (1-6) Ti K-edge EXAFS (weighted by k^2) from experiment (blue line) and fitting (red circle) of TiO_2 thin films prepared by conventional reactive and RGT technique at different oxygen flow timing. Model fits to the experimental filtered EXAFS in the k -space are also shown (insets).

Figure 4.12 displays the normalized absorption spectra of Ti K-edge EXAFS. An analysis of the X-ray absorption spectroscopy (XAS) spectra of undoped TiO_2 thin films can provide insights into the specific arrangement of neighboring atoms around a

titanium (Ti) atom. This investigation focuses on the detailed oscillation patterns seen above the absorption edge energy, specifically around the Ti K-edge, and is conducted using fluorescence mode at room temperature. The background in the x-ray absorption data was subtracted, and the EXAFS spectrum was extracted as a function of the wave vector (k). The Figure 4.12 (insets) displays the k^2 weighted (k) of TiO_2 thin films in the EXAFS analysis.

The EXAFS data at $k^2(k)$ were subjected to Fourier transformation to get the radial distance, $\chi(R)$, for the purpose of making a quantitative comparison. The initial prominent peak in the $|\chi(R)|$ spectra relate to the oxygen atoms that are closest in proximity, while the subsequent peak belongs to the titanium atoms that are the next closest in proximity. The data fitting process considered the alternating routes of single and multiple scattering within a radius of 4 Å from the Ti core atom. The atomic distance, denoted as d , and its variance, σ^2 , which represents structural disorder, are adjusted significantly to provide the best match within the R -range of 0.8 to 3.4. Table 4.3 presents a concise overview of the fit results. The text presents the structural parameters, Debye-Waller factors; σ^2 , R -factor and amplitude reduction of the best EXAFS fit, which were calculated using non-linear least-squares fitting. The calculations and fitting indicate that the TiO_2 coating exhibits a combination of anatase and rutile structures. The initial peak, observed at approximately 1.4 Å, is attributed to the scattering of Ti–O due to the presence of oxygen atoms coordinated with six nearest neighbors around the Ti atom. The second peak, located at around 2.7 Å, is a result of the scattering of Ti–Ti, corresponding to the cations in the second nearest neighbor position. These data are consistent with a prior X-ray absorption spectroscopy (XAS) research of nanomaterials based on TiO_2 (Schneider *et al.*, 2015). It is important to observe that the anatase structure contains four neighboring cations in this particular shell, whereas the rutile structure only has two. Hence, the proportion of rutile and anatase phases has an impact on the bond lengths within the film structure. An analysis of the local structure using EXAFS indicates that the gas timing method can cause steric strain, leading to changes in the lengths of Ti–O and Ti–Ti bonds and an increase in structural disorder (Carta *et al.*, 2015, Schneider *et al.*, 2015).

Table 4.3 EXAFS-derived structural parameters for TiO₂ thin films.

Sample	Shell	N	R(Å)	σ^2	S _o ²	R-factor
1. TiO ₂ conv						
Anatase	Ti – O	4	1.92207	0.01616	0.76	1.6054 %
	Ti – O	2	1.98204	0.01667	0.76	
	Ti – Ti	4	3.04851	0.00626	0.76	
	Ti – Ti	4	3.75054	0.00770	0.76	
Rutile	Ti – O	4	1.96807	0.00085	0.294	
	Ti – O	2	2.00845	0.00087	0.294	
	Ti – Ti	2	2.97519	0.00083	0.294	
	Ti – Ti	8	3.61709	0.00101	0.294	
2. TiO ₂ 57-3						
Anatase	Ti – O	4	1.90993	0.01538	0.673	1.2795 %
	Ti – O	2	1.96952	0.01586	0.673	
	Ti – Ti	4	3.02926	0.00567	0.673	
	Ti – Ti	4	3.72686	0.00698	0.673	
Rutile	Ti – O	4	1.96726	0.00174	0.327	
	Ti – O	2	2.00763	0.00178	0.327	
	Ti – Ti	2	2.97398	0.00389	0.327	
	Ti – Ti	8	3.61561	0.00473	0.327	

Table 4.3 (Continued) EXAFS-derived structural parameters for TiO₂ thin films.

Sample	Shell	N	R(Å)	σ^2	S _o ²	R-factor
3. TiO ₂ 27-3						
Anatase	Ti – O	4	1.91600	0.01159	0.640	2.0797 %
	Ti – O	2	1.97577	0.01196	0.640	
	Ti – Ti	4	3.03888	0.00749	0.640	
	Ti – Ti	4	3.73869	0.00922	0.640	
Rutile	Ti – O	4	1.98005	0.01034	0.360	
	Ti – O	2	2.02068	0.01055	0.360	
	Ti – Ti	2	2.99332	0.00617	0.360	
	Ti – Ti	8	3.63912	0.00751	0.360	
5. TiO ₂ 7-3						
Anatase	Ti – O	4	1.91415	0.01592	0.686	2.0924 %
	Ti – O	2	1.97387	0.01642	0.686	
	Ti – Ti	4	3.03594	0.00817	0.686	
	Ti – Ti	4	3.73508	0.01005	0.686	
Rutile	Ti – O	4	1.96971	0.00382	0.314	
	Ti – O	2	2.01012	0.00390	0.314	
	Ti – Ti	2	2.97768	0.00523	0.314	
	Ti – Ti	8	3.62011	0.00636	0.314	

Table 4.3 (Continued) EXAFS-derived structural parameters for TiO₂ thin films.

Sample	Shell	N	R(Å)	σ^2	S_o^2	R-factor
6. TiO₂ 3-3						
Anatase	Ti – O	4	1.93753	0.01526	0.652	2.8508 %
	Ti – O	2	1.99797	0.01574	0.652	
	Ti – Ti	4	3.07302	0.00741	0.652	
	Ti – Ti	4	3.78070	0.00912	0.652	
Rutile	Ti – O	4	1.98094	0.00770	0.348	
	Ti – O	2	2.02159	0.00786	0.348	
	Ti – Ti	2	2.99466	0.00447	0.348	
	Ti – Ti	8	3.64076	0.00543	0.348	

4.3 SiO₂ films fabricated by custom-built RF magnetron sputtering

In order to prepare the metal oxide thin films, RF magnetron sputtering system locating at SLRI are designed and constructed (Figure 4.13). First of all, the basic need is trying to make the system as clean, or free of contaminants, as possible for maintaining a good vacuum. The work included the procurement of standard and custom-order components which the team used in the construction. In the actual construction of the custom-built system, it is necessary to get professional help and supports from multiple people from SLRI.

The works already done in the sputtering system construction are listed below:

- Installed additional turbomolecular and roughing pumps and compact full range gauge (Pfeiffer Vacuum PKR 251).
- Placed sputtering magnetron gun with ceramic target.
- Installed the cooling system for magnetron gun.
- Set and tested RF power supply connected with matching box.
- Optimize the parameter of the sputtering system

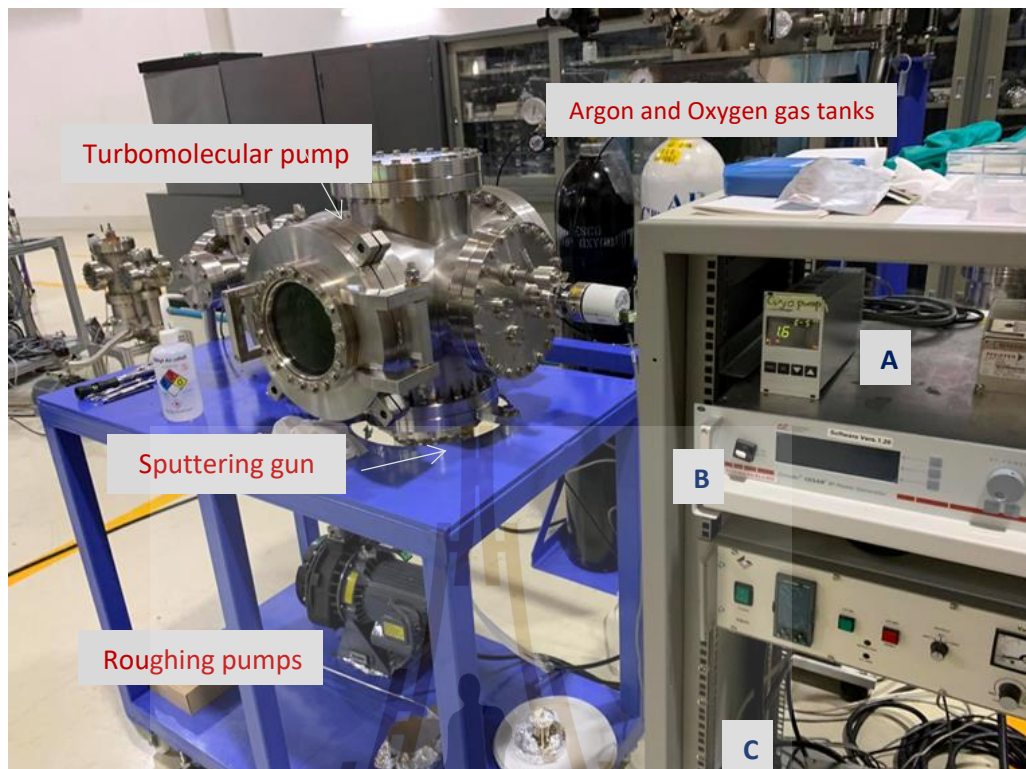


Figure 4.13 View of entire sputtering system (In the rack, A = Turbopump Controller, B = RF Power Supply (600 W) and C = Matching Box.

The custom-built RF magnetron sputtering was used for preparing SiO_2 thin films by using 3-inches SiO_2 target without substrate heating. Figure 4.14 presents transmittance of the Silicon Oxide thin films prepared by custom-built RF magnetron sputtering with different sputtering pressure. The result reveal that lower pressure causes lower %T which are colored. Working pressure was varied between 1.0 -3.0 pascal. The sample with working pressure of 3.0 Pascal have the highest average transmittance percentage ($\sim 82\%$) in entire visible range. The average transmittance percentage that less than 80 are found in case of 1.0, 1.5 and 2.0 Pa (50 W). For the samples with different RF power (50, 100 and 150 W), it is found that higher power introduces lower transmittance, as shown in Figure 4.15.

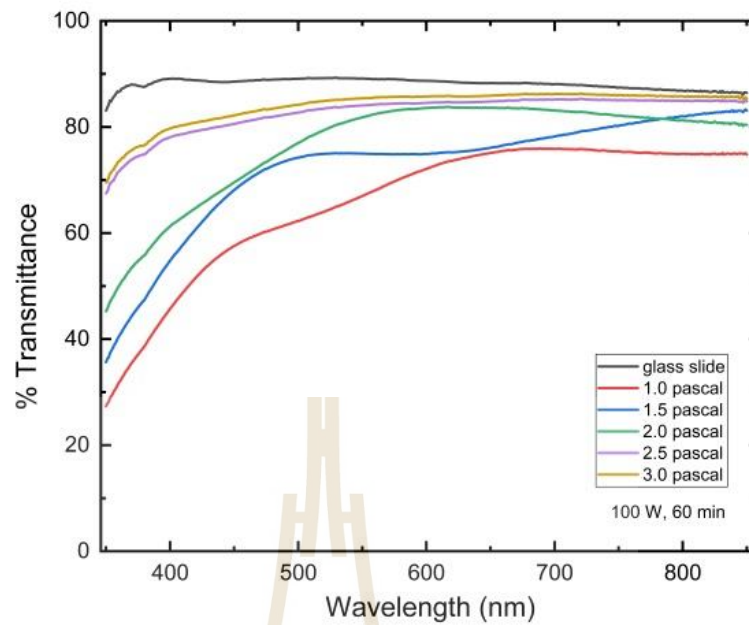


Figure 4.14 Transmittance of the Silicon Oxide thin films prepared by custom-built RF magnetron sputtering with different sputtering pressure.

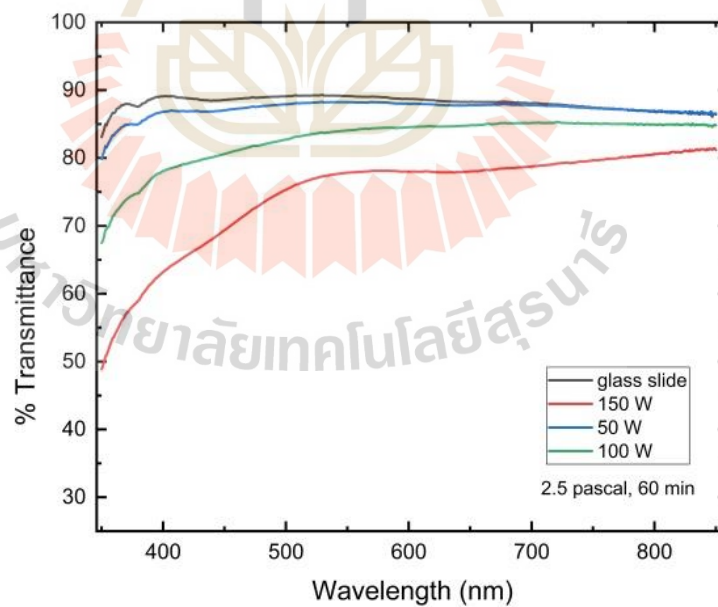


Figure 4.15 Transmittance of the Silicon Oxide thin films with different sputtering power.

Figure 4.16 presents XRD Spectrum of the Silicon Oxide thin films deposited at 50W, 0.8 Pa for 90 min. XRD spectrum from the Figure 4.16 exhibits an amorphous-like nature. Top-view SEM micrographs of the Silicon Oxide thin films deposited at 100 and 150 W is shown in Figure 4.17. The result show that higher power exhibits bigger size of particle on the film surface. SEM micrographs of the Silicon Oxide thin films with different sputtering pressure and time are respectively present in Figure 4.18 and 4.19. Unsmooth surface is observed in almost samples because of unstable plasma. There are dust-like deposited on surface as shown in Figure 4.18 and 4.19.

Since the optical property (%T) and deposition rate is not appropriate and plasma during deposition is unstable. Therefore, another technique is introduced to produce SiO₂ layer. RGT technique was chosen for this study due to high deposition rate (1 nm/min approximately).

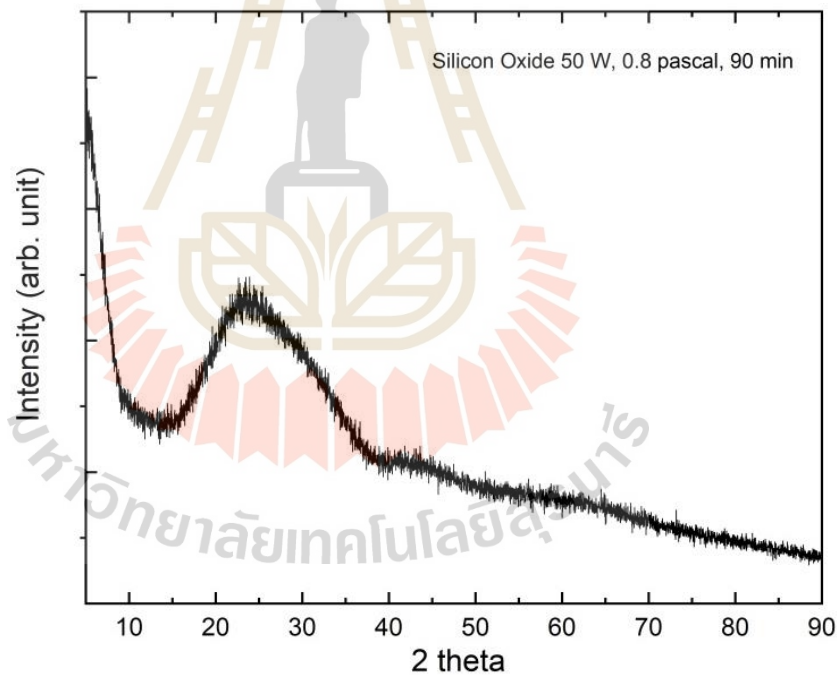


Figure 4.16 XRD Spectrum of the Silicon Oxide thin films deposited at 50W, 0.8 Pa for 90 min.

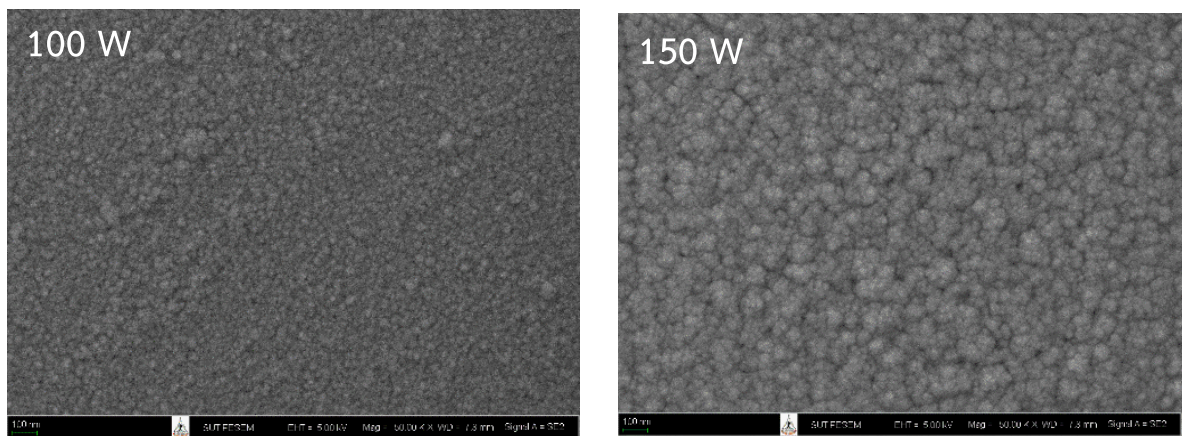


Figure 4.17 Top-view SEM micrographs of the Silicon Oxide thin films deposited at 100 and 150 W.

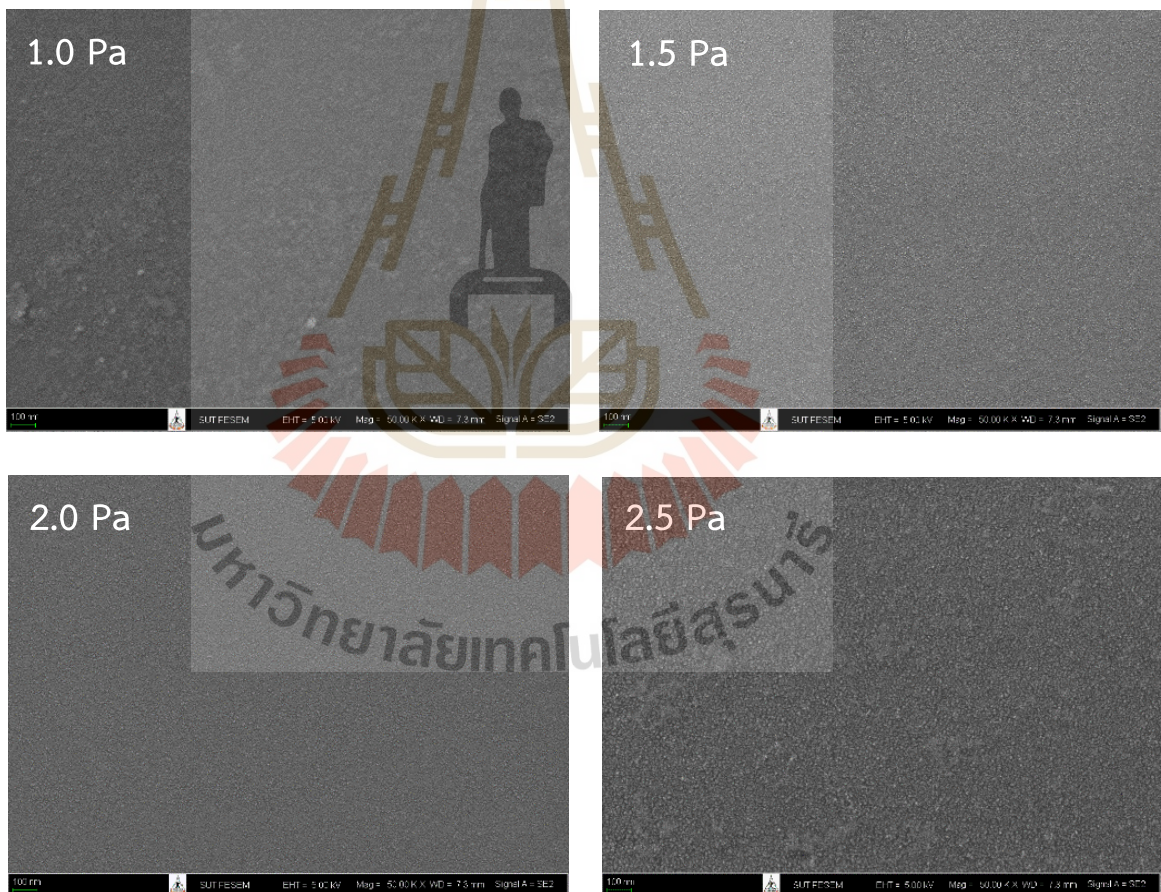


Figure 4.18 SEM micrographs of the Silicon Oxide thin films with different sputtering pressure.

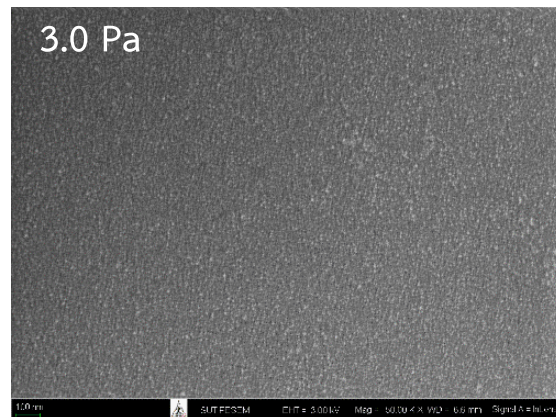


Figure 4.18 (Continued) SEM micrographs of the Silicon Oxide thin films with different sputtering pressure.



Figure 4.19 SEM micrographs of the Silicon Oxide thin films with different sputtering time.

4.4 TiO₂+SiO₂ Multilayer Thin Films

SiO₂ layers were deposited on Si wafer, glass slide and TiO₂ thin film using reactive RF magnetron sputtering technique in combination with gas timing method. Sputtering target was a 2- inch Si metal target (Kert J. Lesker, 99.99%). Argon (Ar) and Oxygen (O₂) with 99.999% purity were used as sputtering and reactive gases respectively. Deposition was performed at room temperature with the base pressure of 5×10^{-6} Torr and working pressure of 3×10^{-3} Torr. RF power was fixed at 120 W. Ar and O₂ flow rate of 20 and 10 were used during deposition process. Argon plasma cleaning of 10 min was perform before every deposition. Deposition time was varied. (15, 30, 45 and 60 min). SiO₂ layer coated on pre-deposited TO₂ film with different conditions (conv, 3-3, 7-3 and 57-3). Cross- section SEM micrograph of the Silicon Oxide thin films deposited on Si wafer shows the thickness of 100 nm (Figure 4.20).

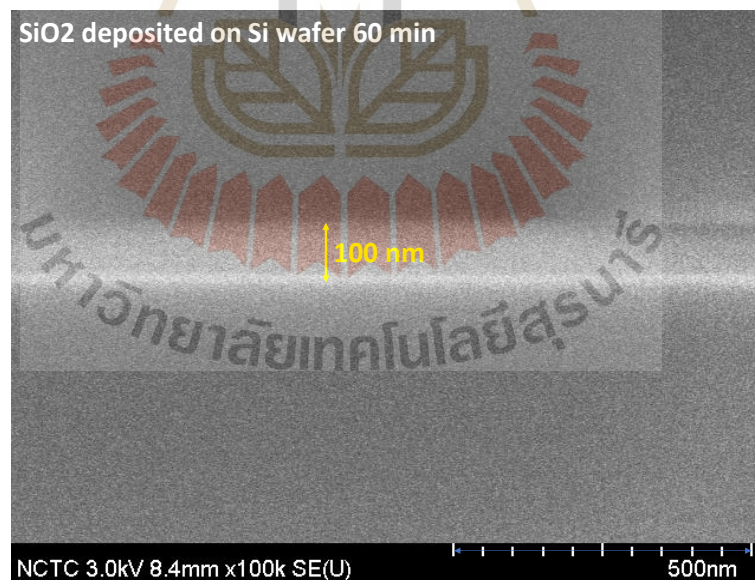


Figure 4.20 Cross- section SEM micrograph of the Silicon Oxide thin films deposited on Si wafer shows the thickness of 100 nm.

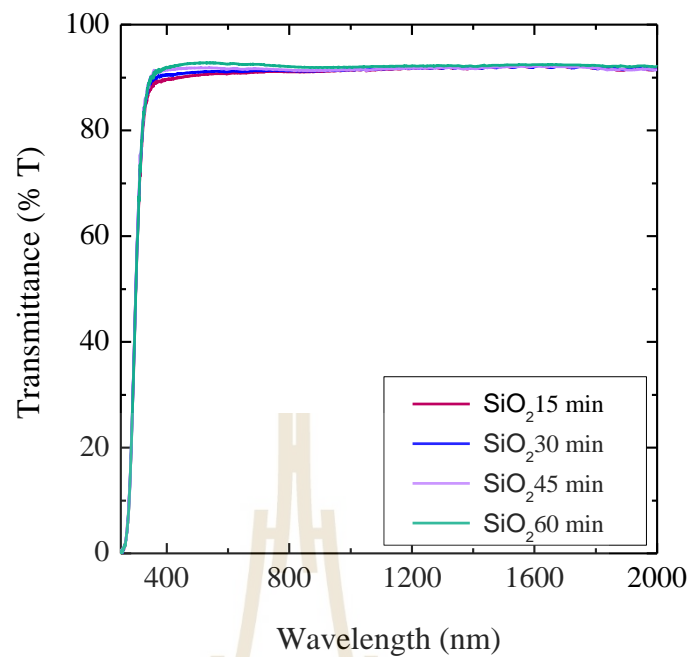


Figure 4.21 Optical transmittance of Silicon Oxide layers deposited on glass substrates with different deposition time.

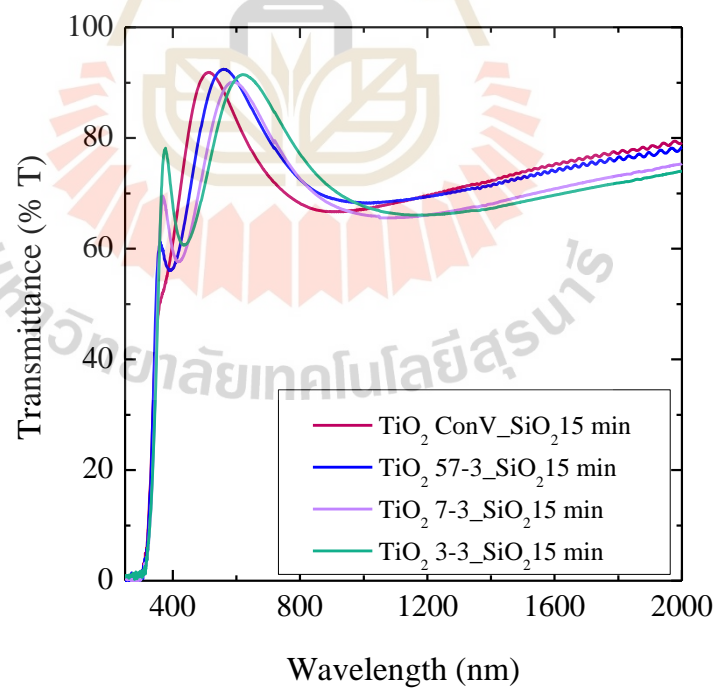


Figure 4.22 Transmittance of 15 min Silicon Oxide layers deposited on various TiO_2 films.

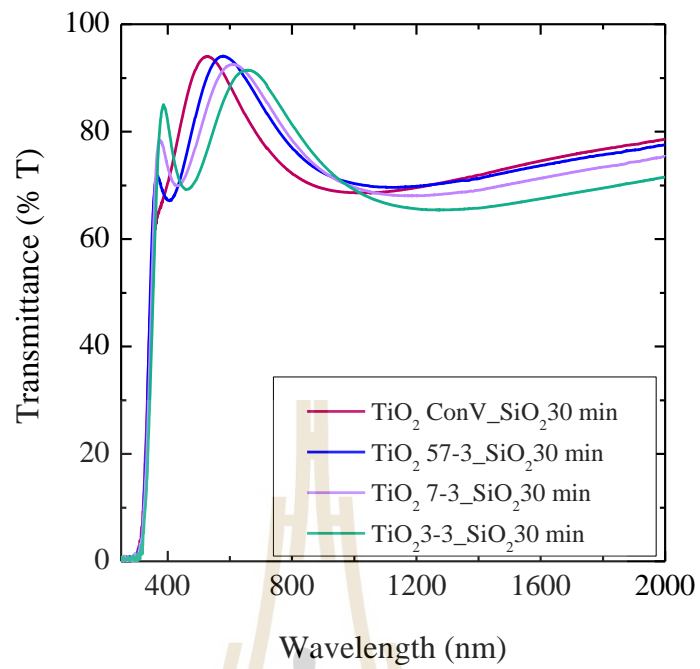


Figure 4.23 Transmittance of 30 min Silicon Oxide layers deposited on various TiO_2 films.

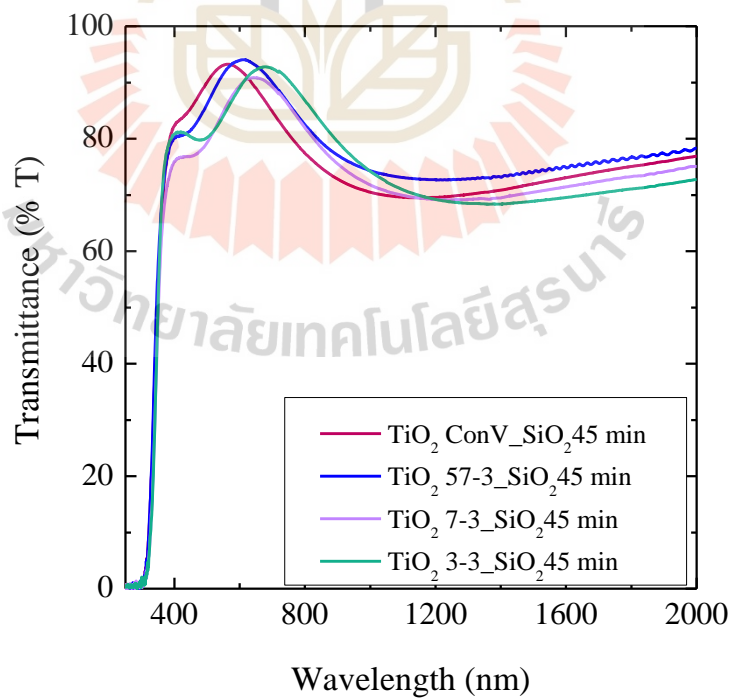


Figure 4.24 Transmittance of 45 min Silicon Oxide layers deposited on various TiO_2 films.

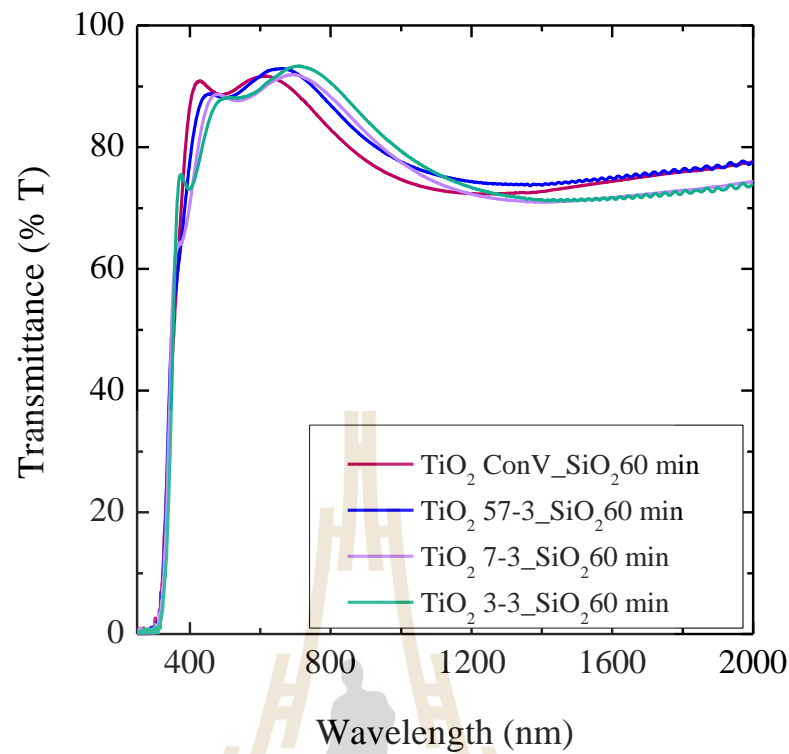


Figure 4.25 Transmittance of 60 min Silicon Oxide layers deposited on various TiO_2 films.

Figure 4.21 – 4.25 illustrates a function of wavelength vs percent T. The deposited thin films are clear and colorless. In terms of edge location and transmittance spectrum characteristics, the transmittance spectra of all samples are noticeably not different. There are oscillations in the transmittance spectra in all samples. The transmittance spectra over the full visible spectrum for all RGT films are in excellent accord with the existing literature (Kang, M. *et al.*, 2018). The shorter oxygen flow time causes longer wavelength shift in the maximum transmittance spectrum as same result found in previous study. It is found that the maximum transmission band edge is changed to at around 360 nanometers. The maximum transmittance peaks of SiO_2 coated on different condition of TiO_2 films are altered. In the visible region, the light transmittance of SiO_2 - TiO_2 multilayer films was greater than that of a single layer TiO_2 film, as seen in Figure 4.26 comparing with Figure 4.8 of transmittance vs wavelength. These multilayer thin films can be used in anti-reflection coating and filter applications.

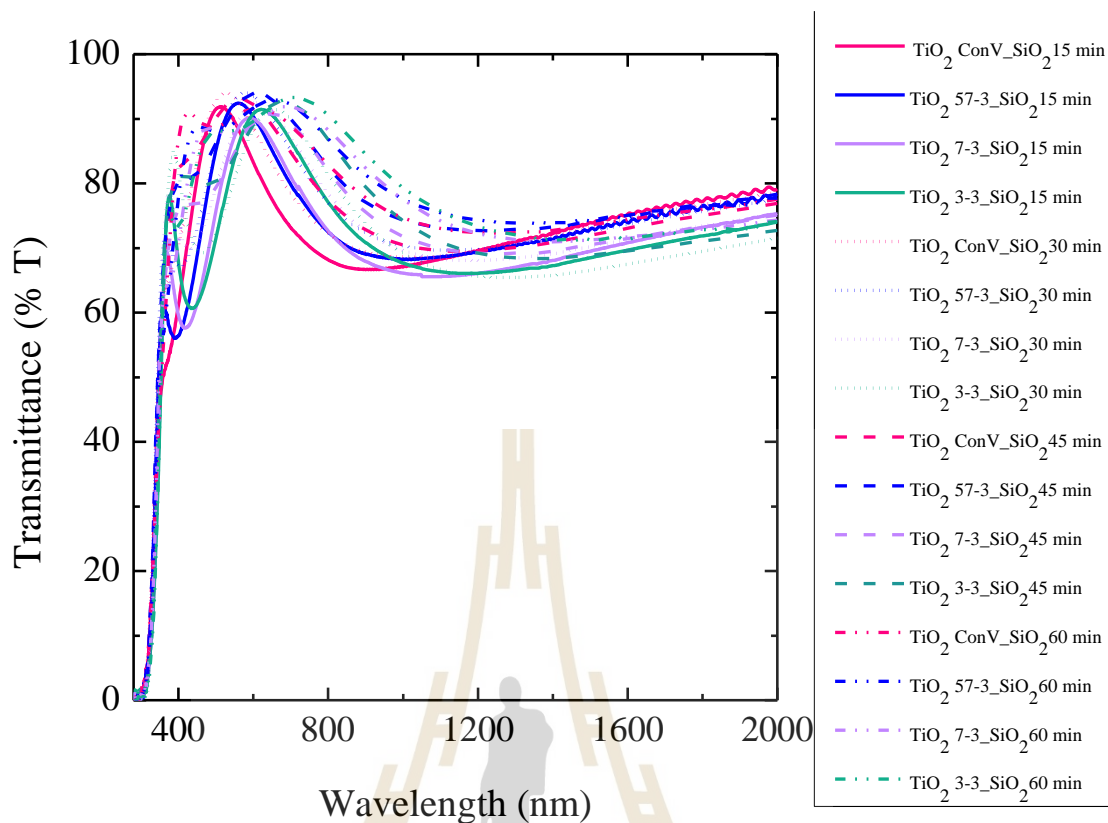


Figure 4.26 Optical transmittance of various deposition time Silicon Oxide layers deposited on various TiO_2 films.

The normalized Si K-edge XANES spectra of Silicon Oxide layers with different deposition time compared with SiO_2 powder standard is illustrated in Figure 4.27. XANES feature reveal SiO_2 structure. Sputtering time have no effect to XANES spectral characteristics, not only for different deposition time but for various pre-deposited TiO_2 layer coated with SiO_2 layer also. From Figure 4.27 -4.29, the gas-timing approach has not considerably altered the XANES spectra of these films.

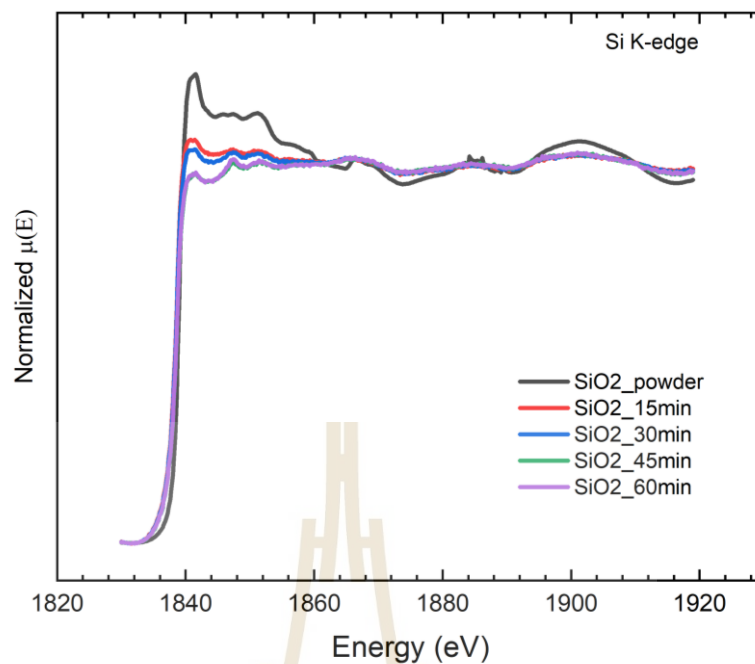


Figure 4.27 The normalized Si K-edge XANES spectra of Silicon Oxide layers with different deposition time compared with SiO₂ powder standard.

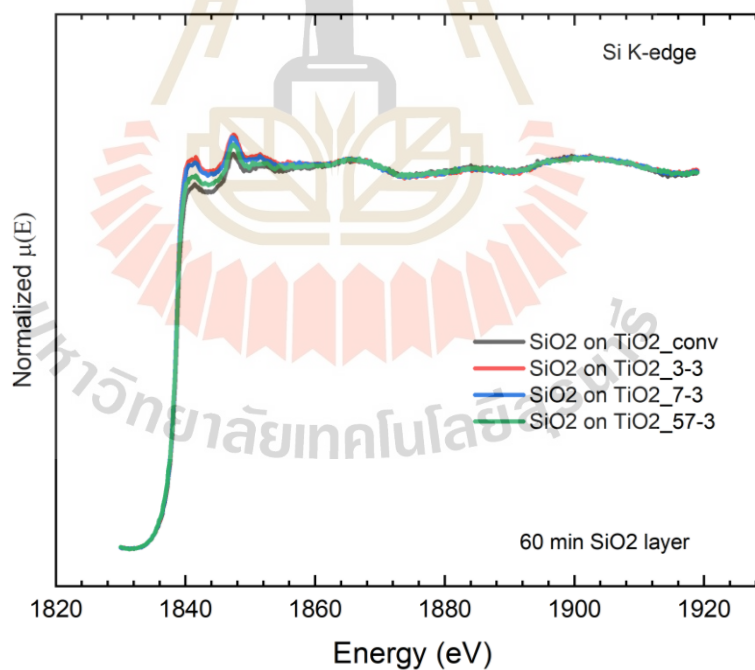


Figure 4.28 The normalized Si K-edge XANES spectra of 60 min silicon oxide layers deposited on various TiO₂ films.

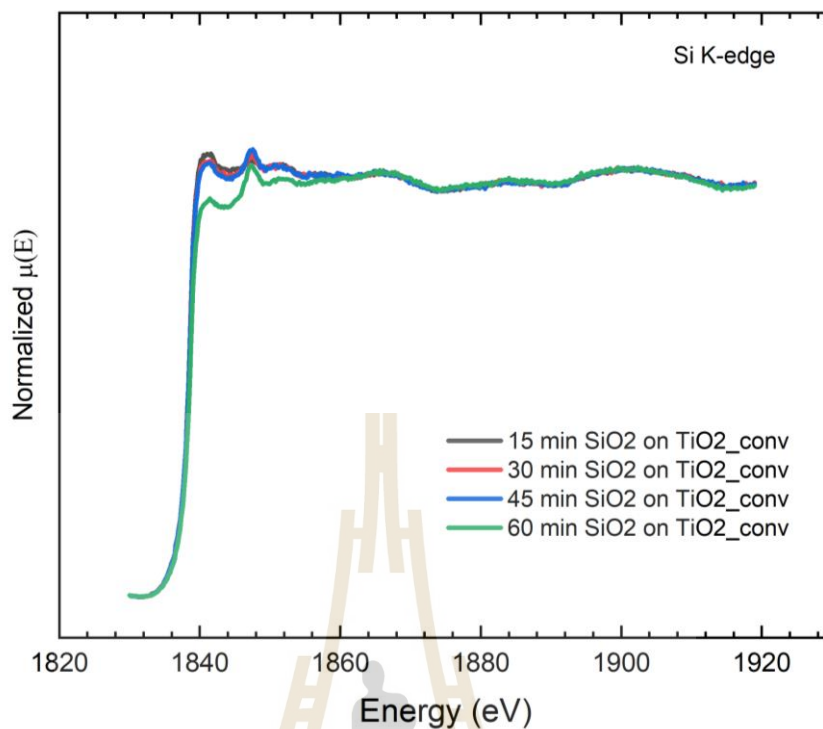


Figure 4.29 The normalized Si K-edge XANES spectra of different deposition time SiO₂ layer coated on TiO₂ films prepared by conventional reactive sputtering.

In Figure 4.30 presents Si K-edge EXAFS (weighted by k^2) from experiment (black line) and fitting (red circle) of SiO₂ layers coated on TiO₂ films prepared by conventional reactive and RGT sputter technique at different oxygen flow timing. The result shows that the bond length of these films has not been significantly influenced by the gas-timing method.

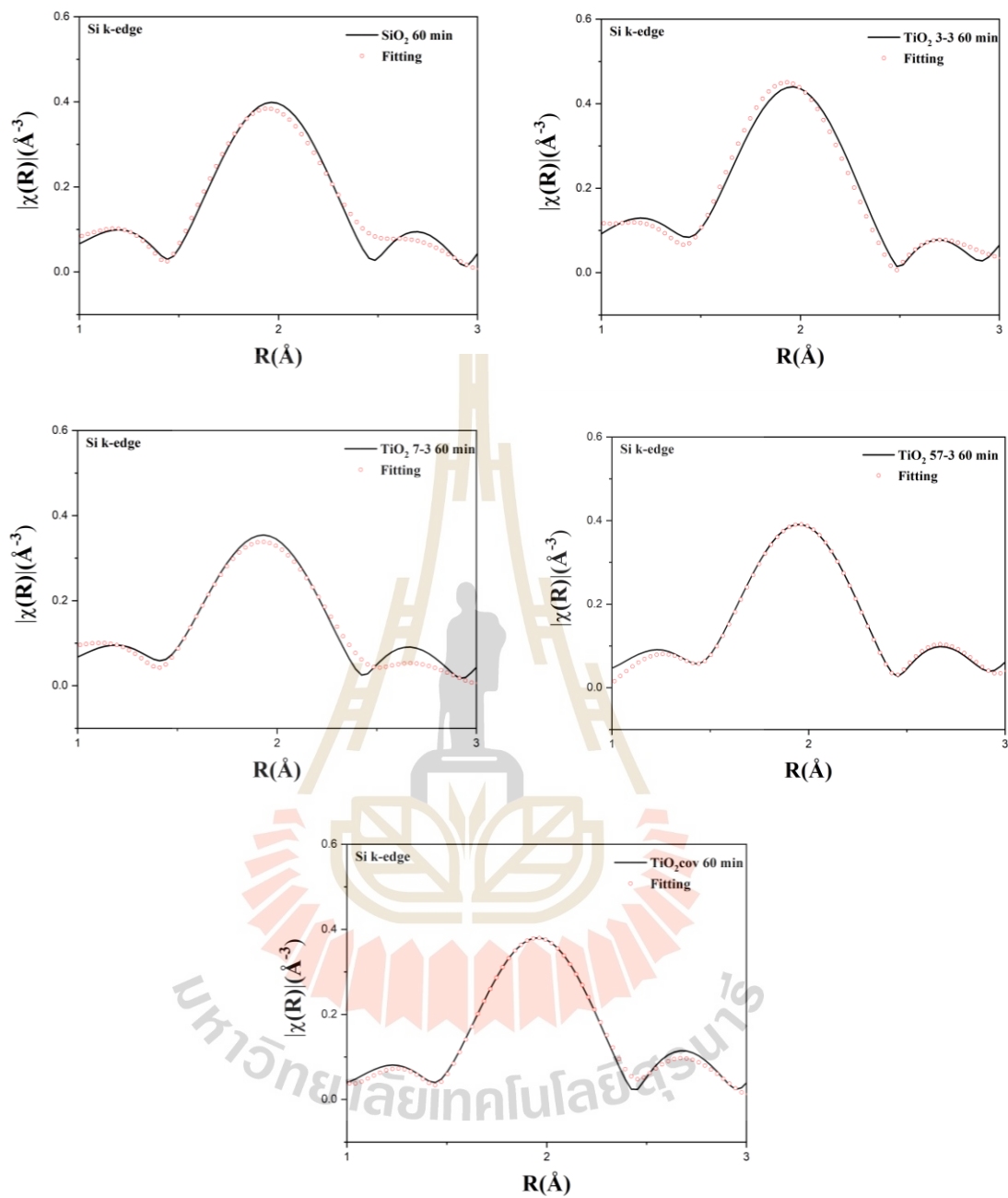


Figure 4.30 Si K-edge EXAFS (weighted by k^2) from experiment (black line) and fitting (red circle) of SiO₂ layers coated on TiO₂ films prepared by conventional reactive and RGT sputter technique at different oxygen flow timing.

CHAPTER V

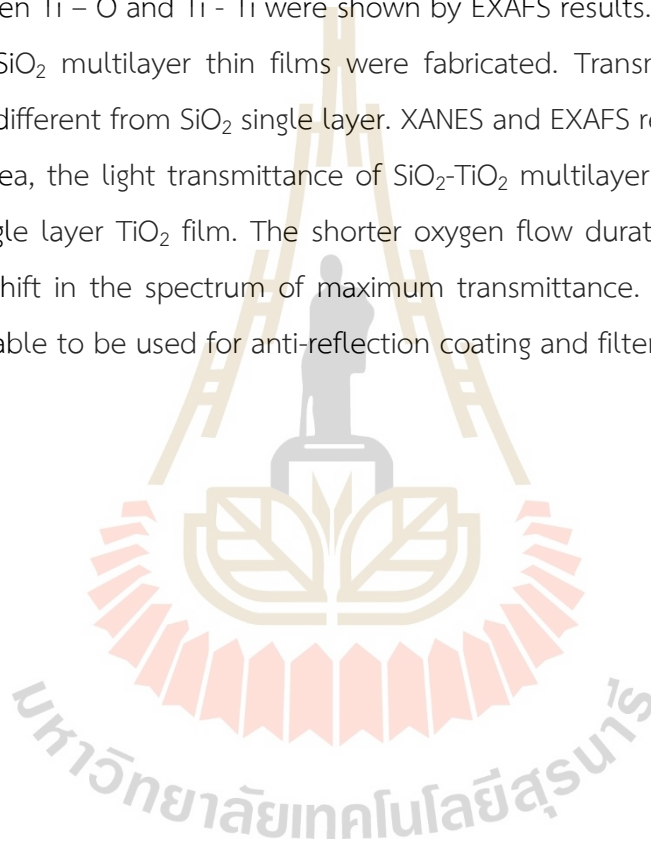
CONCLUSIONS

Titanium oxide mixed-phase thin films were successfully fabricated via RF magnetron sputtering and reactive gas timing (RGT) sputtering. For RF magnetron sputter deposition, the prepared TiO_2 films are ultra-thin (less than 5 nm). In the visible and near-IR spectrum, all samples exhibit a high transmittance ($> 85\%$). Except for the 2.2 Pa sample, the transmittance tended to decrease as the working pressure increased. Refractive index depends on preparation condition (working pressure). Mixing phase of Rutile and Anatase were found in all films corresponding to XANES results. The fitted plots of EXAFS data in the R-space show that the bond length of the lower working pressure sample is greater than that of higher.

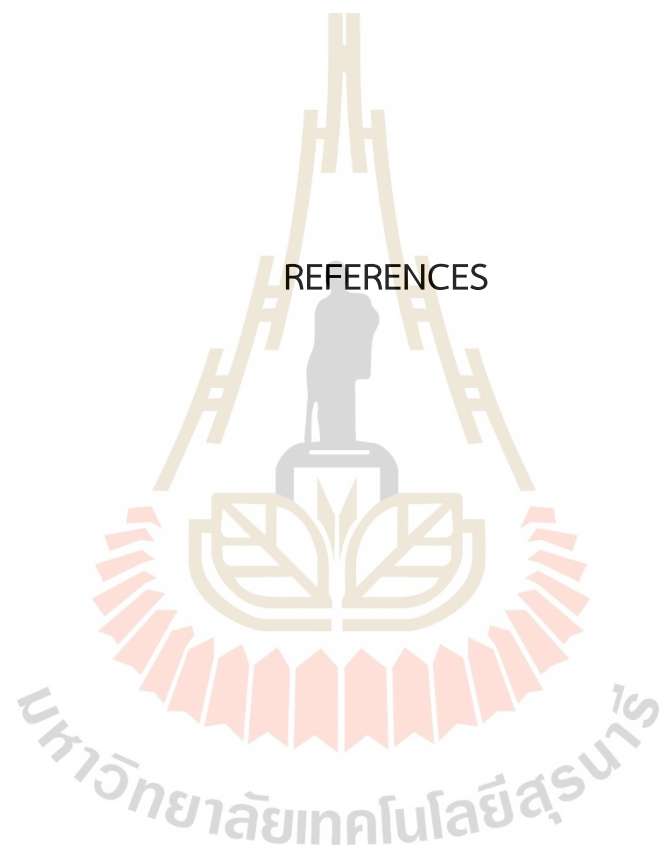
By using reactive gas timing (RGT) sputtering technique, TiO_2 thin films were fabricated on a silicon and glass substrates at fixed working pressure and power. The oxygen flow timing was varied between 3 and 57 s and the stop timing was kept at 3 s. Cross-sectional SEM images reveal that the morphology of prepared TiO_2 thin films have noticeably nano-column shape. The transmittance spectra from UV-vis measurement of the RGT samples are obviously different from the spectrum of uncoated glass slide. The maximum transmittance spectra of the shorter oxygen flow timing show a longer wavelength. Conventional, RGT 57:3, RGT 27:3, and RGT 3:3 films have maximum transmittance peaks at about 475, 530, 560, and 596 nm, respectively, and the maximal light transmittance value is 96%. All of the investigated metal oxides lowered the optical transmittance of undeposited glass when applied as a single layer of TiO_2 . The GIXRD diffraction pattern and Raman spectra of all films exhibits mixed anatase and rutile structure. The XRD results also show that the intensity of the anatase and rutile peaks varies on the preparation conditions.

Considering with the UV-vis result, the transmittance of TiO_2 thin films is sensitive to slight variation in the film structure. The normalized Ti K-edge XANES result in fluorescence mode at different oxygen timing sequence including the spectra of reference samples are report. The characteristics of pre-edge and white line regions of all films reveal the rutile-anatase phase mixture. Linear combination fitting of XANES data exhibits that weight of TiO_2 Anatase and Rutile in TiO_2 thin films depend on the oxygen flow timing which is good agreement between XANES and XRD results. Bond length between Ti – O and Ti - Ti were shown by EXAFS results.

$\text{TiO}_2+\text{SiO}_2$ multilayer thin films were fabricated. Transmittance of $\text{TiO}_2+\text{SiO}_2$ multilayer is different from SiO_2 single layer. XANES and EXAFS results are analyzed. In the visible area, the light transmittance of $\text{SiO}_2\text{-TiO}_2$ multilayer films was larger than that of a single layer TiO_2 film. The shorter oxygen flow duration results in a larger wavelength shift in the spectrum of maximum transmittance. These multilayer thin films are suitable to be used for anti-reflection coating and filter applications.



REFERENCES



REFERENCES

- Agirseven, O., Rivella, Jr. D. T., Haggerty, J. E. S., Berry, P. O., Diffendaffer, K., Patterson, A., Krebs, J., Mangum, J. S., Gorman, B. P., Perkins, J. D., Chen, B. R., Schelhas, L. T., and Tate, J. (2020). Crystallization of TiO₂ polymorphs from RF-sputtered, amorphous thin-film precursors. *AIP Advances* 10, 025109.
- Berghuis, W. J. H., Melskens, J., Macco, B., Basuvalingam, S. B., Verheijen, M. A., and Kessels, W. M. M. (2020). Atomic layer deposition of Nb-doped TiO₂: Dopant incorporation and effect of annealing. *Journal of Vacuum Science & Technology. A. Vacuum, Surfaces, and Films*, 38(2).
- Bharti, B., Kumar, S., Lee, H. N., and Kumar, R. (2016). Formation of oxygen vacancies and Ti³⁺ state in TiO₂ thin film and enhanced optical properties by air plasma treatment. *Scientific Reports*, 6(1).
- Boonkoom, T., Tantisantisom, K., and Manyam, J. (2015). Study of structural properties of N-doped ZnO thin film prepared by reactive gas-timing RF magnetron sputtering. *Advanced Materials Research*, 1131, 8-11.
- Braem, A., David, C., and Joram, C. (2005). Metal multi-dielectric mirror coatings for Cherenkov detectors. *Nuclear Instruments and Methods in Physics Research A*, 553, 182–186.
- Braeuer, G., Szyszka, B., Vergoehl, M., and Bendorf, R.. (2010). Magnetron sputtering – Milestones of 30 years. *Vacuum*, 84, 1354–1359.
- Carta, D., Mountjoy, G., Regoutz, A., Khat, A., Serb, A., and Prodromakis, T. (2015). X-ray Absorption Spectroscopy Study of TiO_{2-x} Thin Films for Memory Applications. *Journal of Physical Chemistry. C*, 119(8), 4362–4370.
- Choi, H. C., Jung, Y. M., and Kim, S. B. (2005). Size effects in the Raman spectra of TiO₂ nanoparticles. *Vibrational Spectroscopy*, 37(1), 33–38.

- Chittinan, D., Buranasiri, P., Lertvanithphol, T., Eiamchai, P., Tantiwanichapan, K., Sathukarn, A., Limwichean, S., Klamchuen, A., Wutikhun, T., Limsuwan, P., Nakajima, H., Phae-Ngam, W., Triamnak, N., and Horprathum, M. (2023). Tailoring the structural and optical properties of fabricated TiO₂ thin films by O₂ duty cycle in reactive gas-timing magnetron sputtering. *Vacuum*, 214, 112205.
- Dou, W., Wang, P., Zhang, D., and Yu, J. (2016). An efficient way to prepare hydrophobic antireflective SiO₂ film by sol–gel method. *Materials Letters*, 167, 69–72.
- Dubey, R. S., and Ganesan, V. (2017). Fabrication and characterization of TiO₂/SiO₂ based Bragg reflectors for light trapping applications. *Results in Physics*, 7, 2271–2276.
- El-Deen, S. S., Hashem, A. M., Abdel Ghany, A. E., Indris, E., Ehrenberg, H., Mauger, A. and Julien, C. M. (2018). Anatase TiO₂ nanoparticles for lithium-ion batteries. *Ionics*, 24, 2925–2934.
- Esch, T. R., Gadaczek, I., and Bredow, T. (2014). Surface structures and thermodynamics of low-index of rutile, brookite and anatase -A comparative DFT study. *Applied Surface Science*, 288, 275– 287.
- Fan, C., Chen, C., Wang, J., Fu, X., Ren, Z., Qian, G., and Wang, Z. (2015). Black Hydroxylated Titanium Dioxide Prepared via Ultrasonication with Enhanced Photocatalytic Activity. *Scientific Reports*, 5, 11712.
- Fedulova, E. (2016). *Development of dielectric multilayer coating for ultrafast oscillator*. Ph.D. Dissertation, Ludwig Maximilian University of Munich, Germany.
- Fracchia, M., Ghigna, P., Minguzzi, A., Vertova, A., Turco, F., Cerrato, G., and Meroni, D. (2020). Role of Synthetic Parameters on the Structural and Optical Properties of N,Sn-copromoted Nanostructured TiO₂: A Combined Ti K-edge and Sn L2,3-edges X-ray Absorption Investigation. *Nanomaterials*, 10, 1224.
- Fujiyama, H., Sumomogi, T., and Endo, T. (2002). Effect of O₂ gas partial pressure on mechanical properties of SiO₂ films deposited by radio frequency magnetron sputtering. *Journal of Vacuum Science & Technology A*, 20, 356-361.
- Ghamsari, M. S., Radiman, S., AzmiAbdulHamid, M., Mahshid, S., and Rahmani, Sh. (2013). Room temperature synthesis of highly crystalline TiO₂ nanoparticles. *Materials Letters*, 92, 287–290.

- Gonçalves, D., and Irene, E. A. (2002). Fundamentals and applications of spectroscopic ellipsometry. *Química Nova*, 5, 794-800.
- Gracia, F., Yubero, F., Holgado, J. P., Espinos, J. P., Gonzalez-Elipe, A. R., and Girardeau, T. (2006). SiO₂/TiO₂ thin films with variable refractive index prepared by ion beam induced and plasma enhanced chemical vapor deposition. *Thin Solid Films*, 500, 19-26.
- Grayeli Korpi, A. R., Rezaee, S., Luna, C., Talu, S., Arman, A., and Ahmadpourian, A. (2017). Influence of the oxygen partial pressure on the growth and optical properties of RF-sputtered anatase TiO₂ thin films. *Results in Physics*, 7, 3349–3352.
- Gnaser, H., Lösch, J., Orendorz, A., and Ziegler, C. (2011). Temperature-dependent grain growth and phase transformation in mixed anatase-rutile nanocrystalline TiO₂ films. *physica status solidi (a)*, 208(7), 1635-1640.
- Guillén, E., Krause, M., Heras, I., Rincón-Llorente, G., and Escobar-Galindo, R.. (2021). Tailoring Crystalline Structure of Titanium Oxide Films for Optical Applications Using Non-Biased Filtered Cathodic Vacuum Arc Deposition at Room Temperature. *Coatings*, 11, 233, 1-16.
- Han, K., and Kim, J. H. (2011). Fabrication of TiO₂/SiO₂ multilayer film structure by the sol-gel process with efficient thermal treatment methods. *Applied Surface Science*, 263, 69-72.
- Han, K., and Kim, J. H. (2011). Reflectance modulation of transparent multilayer thin films for energy efficient window applications. *Materials Letters*, 65, 2466–2469.
- Hilfiker, J. N., Pribil, G. K., Synowicki, R., Martin, A. C., and Hale, J. S. (2019). Spectroscopic ellipsometry characterization of multilayer optical coatings. *Surface & Coatings Technology*, 357, 114-121.
- Hou, L., Zhang, M., Guan, Z., Li, Q., and Yang, J. (2018). Effect of annealing ambience on the formation of surface/bulk oxygen vacancies in TiO₂ for photocatalytic hydrogen evolution. *Applied Surface Science*, 428, 640-647

- Jasinski, J., Lubas, M., Suchorab, K., Gawda, M., Kurpaska, L., Brykala, M., Kosinska, A., Sitarz, M., and Jagielski, J. (2022). Qualitative and semi-quantitative phase analysis of TiO₂ thin layers by Raman imaging. *Journal of Molecular Structure*, 1260, 132803.
- Jeong, S. H., Kim, J. K., Kim, B. S., Shim, S. H., and Lee, B. T. (2004). Characterization of SiO₂ and TiO₂ films prepared using rf magnetron sputtering and their application to anti-reflection coating. *Vacuum*, 76, 507-515.
- Jia, J., Yamamoto, H., Okajima, T., and Shigesato, Y. (2016). On the Crystal Structural Control of Sputtered TiO₂ Thin Films. *Nanoscale Research Letters*, 11(1).
- Jia, T., Zhang, J., Wua, J., Wanga, D., Liu, Q., Qi, Y., Hue, B., He, P., Pan, W., and Qi, X. (2020). Synthesis amorphous TiO₂ with oxygen vacancy as carriers transport channels for enhancing photocatalytic activity. *Materials Letters*, 265, 127465.
- Jin, F., Zhang, X., Wei, M., and Ma, Y. (2019). Effects of defects on the electronic and optical properties of TiO₂ nanosheet. *Electronic Structure*, 044002.
- Kang, M., Kim, S. W., and Park, H. Y. (2018). Optical properties of TiO₂ thin films with crystal structure. *Journal of Physics and Chemistry of Solids*, 123, 266-270.
- Karlsson, S., Bäck, L. G., Kidkhunthod, P., Lundstedt, K., and Wondraczek, L. (2016). Effect of TiO₂ on optical properties of glasses in the soda-lime-silicate system. *OPTICAL MATERIALS EXPRESS*, 1198.
- Kavaliunas, V., Sestakauskaitė, A., Sriubas, M., and Laukaitis, G. (2019). Influence of Deposition Parameters on the Structure of TiO₂ Thin Films Prepared by Reactive Magnetron Sputtering Technique. *INTER-ACADEMIA*, 53, 49-57.
- Kesmez, Ö., Akarsu, E., Çamurlu, H.E., Yavuz, E., Akarsu, M., and Arpaç, E. (2018). Preparation and characterization of multilayer anti-reflective coatings via sol-gel process. *Ceramics International*, 44, 3183-3188.
- Khatibnezhad, H., Ambriz-Vargas, F., Ettouil, F. B., and Moreau, C. (2022). Role of phase content on the photocatalytic performance of TiO₂ coatings deposited by suspension plasma spray. *Journal of the European Ceramic Society*, 42(6), 2905-2920.

- Kim, D., Kim, K. M., Han, H., Lee, J., Ko, D., Park, K. R., Jang, K., Kim, D., Forrester, J. S., Lee, S. H., Kim, J. C., and Mhin, S. (2022). Ti/TiO₂/SiO₂ multilayer thin films with enhanced spectral selectivity for optical narrow bandpass filters. *Scientific Reports*, 12(32), 1-10.
- Kim, W. B., Choi, S. H., and Lee, J. S. (2000). Quantitative Analysis of Ti-O-Si and Ti-O-Ti Bonds in Ti-Si Binary Oxides by the Linear Combination of XANES. *the Journal of Physical Chemistry*, 104(36), 8670–8678.
- Klaitabtim, D., Pratontep, S., and Nukeaw, J. (2008). Effect of gas-timing technique on structure and optical properties of sputtered zinc oxide films. *Ceramics International*, 34, 1103-1107.
- Kojima, I., Li, B., and Fujimoto, T. (1999). XRR and XPS Studies of SiO₂ Thin Films Formed by r.f. Magnetron Sputtering. *Surf. Interface Anal*, 28, 267-270.
- Kurenkova, A. Y., Kremneva, A. M., Saraev, A. A., Murzin, V., Kozlova, E. A., and Kaichev, V. V. (2020). Influence of Thermal Activation of Titania on Photoreactivity of Pt/TiO₂ in Hydrogen Production. *Catalysis Letters*, 151, 748-754.
- Le, N. T. H., Thanh, T. D., Pham, V.-T., Phan, T. L., Lam, V. D., Manh, D. H., Anh, T. X., C. Le, T. K., Thammajak, N., Hong, L. V. and Yu, S. C. (2016). Structure and high photocatalytic activity of (N, Ta)-doped TiO₂ nanoparticles. *JOURNAL OF APPLIED PHYSICS*, 120, 142110.
- Lee, C. C., and Jan, D. J. (2006). DC magnetron sputtering of Si to form SiO₂ in low-energy ion beam. *Vacuum*, 80, 693-697.
- Lertvanithphol, T., Rakreungdet, W., Chananonnawathorn, C., Eiamchai, P., Limwichean, S., Nuntawong, N., Patthanasettakul, V., Klamchuen, A., Khemasiri, N., Nukeaw, J., Seawsakul, K., Songsiriritthigul, C., Chanlek, N., Nakajima, H., Songsiriritthigul, P., and Horprathum, M. (2019). Spectroscopic study on amorphous tantalum oxynitride thin films prepared by reactive gas-timing RF magnetron sputtering. *Applied Surface Science*, 492, 99-107.
- Lertvanithphol, T., Rakreungdet, W., Chananonnawathorn, C., Eiamchai, P., Limwichean, S., Nuntawong, N., and Horprathum, M. (2019). Spectroscopic study on amorphous tantalum oxynitride thin films prepared by reactive gas-timing RF magnetron sputtering. *Applied Surface Science*, 492, 99-107.

- Li, J., Zhou, H., Zhuo, H., Wei, Z., Zhuang, G., Zhong, X., Deng, S., Li, X., and Wang, J. (2013). Oxygen Vacancy on TiO_2 Promoted the Activity and Stability of Supported Pd Nanoparticles for Oxygen Reduction Reaction. *Journal of Materials Chemistry A*, 1-3.
- Lu, W., Bruner, B., Casillas, G., Mejia-Rosales, S., Farmer, P. J., and Jos'e-Yacam'an, M. (2012). Direct oxygen imaging in titania nanocrystals. *Nanotechnology*, 23, 335706.
- Macleod, H. G. (2010). *Thin-Film Optical Filters* (4th ed.), Florida, CRC Press.
- Matsuo, S., Sakaguchi, N., and Wakita, H. (2005). Pre-edge Features of Ti K-edge X-ray Absorption Near-edge Structure for the Local Structure of Sol-Gel Titanium Oxides. *Analytical Sciences*, 21(7), 805-809.
- Mattox, D. M. (2010). *Handbook of Physical Vapor Deposition (PVD) Processing* (2nd ed.). New York, William Andrew.
- Nair, P. B., Justinivictor, V., Daniel, G. P., Joy, K., Ramakrishnan, V., and Thomas, P. (2011). Effect of RF power and sputtering pressure on the structural and optical properties of TiO_2 thin films prepared by RF magnetron sputtering. *Applied Surface Science*, 257(24), 10869-10875.
- Nair, P. B., Justinivictor, V. B., Daniel, G. P., Joy, K., James Raju, K. C., Kumar, D. D., and Thomas, P. V. (2014). Optical parameters induced by phase transformation in RF magnetron sputtered TiO_2 nanostructured thin films. *Progress in Natural Science: Materials International*, 24, 218-225.
- Nair, P. B., Justinivictor, V. B., Daniel, G. P., Joy, K., Ramakrishnan, V., and Thomas, P. V. (2011). Effect of RF power and sputtering pressure on the structural and optical properties of TiO_2 thin films prepared by RF magnetron sputtering. *Applied Surface Science*, 257, 10869-10875.
- Nakai, I., Hattori, A., Ishii, T., and Li, Y. (2013). XAS spectra of mechanically milled TiO_2 . *Journal of Physics. Conference Series*, 430, 012084.
- Nakajima, H., Mori, T., Shen, Q., and Toyoda, T. (2005). Photoluminescence study of mixtures of anatase and rutile TiO_2 nanoparticles: Influence of charge transfer

- between the nanoparticles on their photoluminescence excitation bands. *Chemical Physics Letters*, 409, 81-84.
- Nezar, S., Saoula, N., Sali, S., Faiz, M., Mekki, M., Laoufi, N. A., and Tabet, N. (2017). Properties of TiO₂ thin films deposited by rf reactive magnetron sputtering on biased substrates. *Applied Surface Science*, 395, 172-179.
- Nezar, S., Saoula, N., Salic, S., Faiz, M., Mekki, M., Laoufi, N. A., and Tabet, N. (2017). Properties of TiO₂ thin films deposited by rf reactive magnetron sputtering on biased substrates. *Applied Surface Science*, 395, 172-179.
- Niltharach, A., Kityakarn, S., Worayingyong, A., Thienprasert, J., Klysubun, W., Songsirittthigul, P., and Limpijumnong, S. (2012). Structural characterizations of sol-gel synthesized TiO₂ and Ce/TiO₂ nanostructures. *Physica. B, Condensed Matter*, 407(15), 2915-2918.
- Park, S., Kim, C. H., Lee, W. J., Sung, S., and Yoon, M. H. (2017). Sol-gel metal oxide dielectrics for all - solution- processed electronics. *Materials Science and Engineering R*, 114, 1-22.
- Pjević, D., Obradović, M., Marinković, T., Grce, A., Milosavljević, M., Grieseler, R., Kups, T., Wilke, M., and Schaaf, P. (2015). Properties of sputtered TiO₂ thin films as a function of deposition and annealing parameters. *Physica B: Physics of Condensed Matter*, 463, 1-6.
- Popok, V. N., Barke, I., Campbell, E. E. B., and Meiwes-Broer, K. H. (2011). Cluster-surface interaction: From soft landing to implantation. *Surface Science Reports*, 66, 347-377.
- Ran, J., Liu, H., Dong, H., Gao, P., Cheng, H., Xu, J., Wang, H., Wang, Z., Fu, Q., Yan, J., and Liu, J. (2023). Accurate quantification of TiO₂(B)'s phase purity via Raman spectroscopy. *Green Energy & Environment*, 8(5), 1371-1379.
- Raut, H. K., Ganesh, V. A., Nair, A. S., and Ramakrishna, S. (2011). Anti-reflective coatings: A critical, in-depth review. *Energy Environ. Sci.*, 4, 3779-3804.
- Raut, H. K., Nair, A. S., Dinachali, S. S., Ganesh, V. A., Walsh, T. M., and Ramakrishna, S. (2013). Porous SiO₂ anti-reflective coatings on large-area substrates by electrospinning and their application to solar modules. *Solar Energy Materials & Solar Cells*, 111, 9-15.

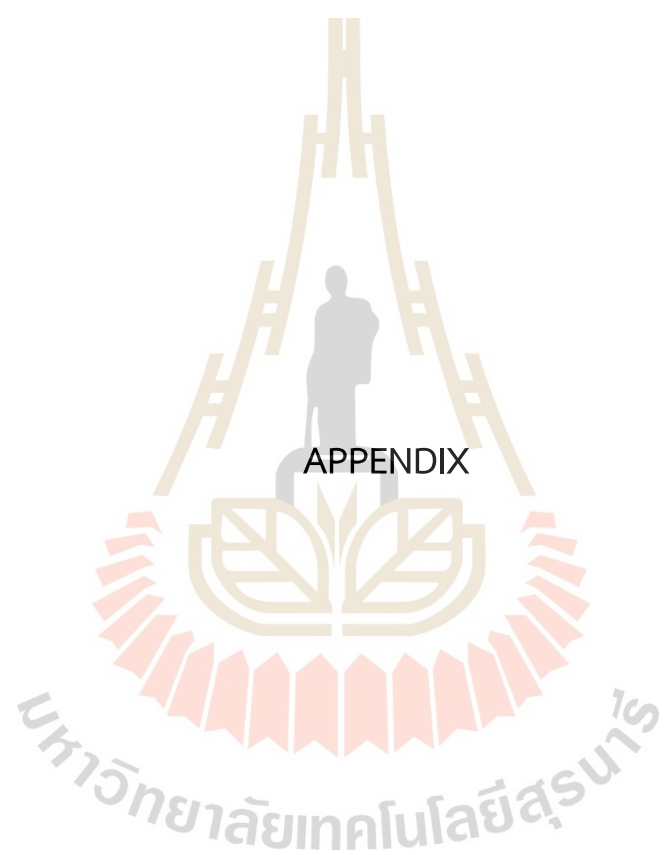
- Rekas, M. (2015). XAS study of TiO₂-based nanomaterials. *Radiation Physics and Chemistry*, 112, 195-198.
- Rojsatien, S., Mannodi-Kanakkithodi, A., Walker, T., Nietzold, T., Colegrove, E., Lai, B., Cai, Z., Holt, M., Chan, M. K., and Bertoni, M. (2023). Quantitative analysis of Cu XANES spectra using linear combination fitting of binary mixtures simulated by FEFF9. *Radiation Physics and Chemistry*, 202, 110548.
- Sahoo, M., Yadav, A. K., Jha, S. N., Bhattacharyya, D., Mathews, T., Sahoo, N. K., Dash, S., and Tyagi, A. K. (2015). Nitrogen Location and Ti-O Bond Distances in Pristine and N-Doped TiO₂ Anatase Thin Films by X-ray Absorption Studies. *The Journal of Physical Chemistry C*, 119, 17640-17647.
- Savio, A. K., Starikov, D., Bensaoula, A., Pillai, R., De La Torre García, L. L., and Hernández, F. C. R. (2012). Tunable TiO₂ (anatase and rutile) materials manufactured by mechanical means. *Ceramics International*, 38(5), 3529-3535.
- Scanlon, D. O., Dunnill, C. W., Buckeridge, J., Shevlin, S. A., Logsdail, A. J., Woodley, S. M., Catlow, C. R. A., Powell, M. J., Palgrave, R. G., Parkin, I. P., Watson, G. W., Keal, T. W., Sherwood, P., Walsh, A., and Sokol, A. A. (2013). Band alignment of rutile and anatase TiO₂. *Nature Materials*, 12(9), 798-801.
- Schneider, K., Zajac, D., Sikora, M., Kapusta, C., Michalow-Mauke, K., Graule, T., and Rekas, M. (2015). XAS study of TiO₂-based nanomaterials. *Radiation Physics and Chemistry*, 112, 195-198.
- Schneider, K., Zajac, D., Sikora, M., Kapusta, Cz., Michalow-Mauke, K., Graule, Th., and Schnohr, C. S., and Ridgway, M. C. (2015). X-Ray Absorption Spectroscopy of Semiconductors, *Springer Series in Optical Sciences*, 190.
- Seguini, G., Schamm-Chardon, S., Pellegrino, P., and Perego, M. (2011). The energy band alignment of Si nanocrystals in SiO₂. *Applied Physics Letters*, 99, 082107-082111.
- Serway, R. A., and Jewett, Jr. J. W. (2014). *Physics for Scientists and Engineers with modern physics (9th ed.)*, Brooks/Cole.
- Šimurka, L., Čtvrtlík, R., Tomašík, J., Bektaş, G., Svoboda, J., and Bange, K. (2018). Mechanical and optical properties of SiO₂ thin films deposited on glass. *Chemical Papers*, 72, 2143-2151.

- Singh, R., Gupta, M., Phase, D. M., and Mukherjee, S. K. (2019). Phase growth analysis of sputtered TiO₂ thin films at low oxygen partial pressures using XANES and XRR. *Materials Research Express*, 6(11), 116449.
- Songsiriritthigul, P. and Limpijumnonng, S. (2012). Structural characterizations of sol–gel synthesized TiO₂ and Ce/TiO₂ nanostructures. *Physica B*, 407, 2915–2918.
- Soult M. C., Siller, V., Zhu, X., Gehlhaar, R., Wojcik, P. J., Morata, A., Tarancón, A., Vereecken, P. M., and Hubin, A. (2022) Spectroscopic Ellipsometry for Operando Monitoring of (De)Lithiation-Induced Phenomena on LiMn₂O₄ and LiNi_{0.5}Mn_{1.5}O₄ Electrodes. *Journal of The Electrochemical Society*, 169(4), 040501
- Stabrawa, I., Kubala-Kuku, A., Bana, D., Pepponi, G., Braziewicz, J., Pajek, M., and Teodorczyk, M. (2019). Characterization of the morphology of titanium and titanium (IV) oxide nanolayers deposited on different substrates by application of grazing incidence X-ray diffraction and X-ray reflectometry techniques. *Thin Solid Films*, 671, 103–110.
- Sultan, Md. Z. and Sultana N. (2015). Analysis of Reflectance and Transmittance Characteristics of Optical Thin Film for Various Film Materials, Thicknesses and Substrates. *Journal of Electrical & Electronic Systems*, 4(3), 160-163.
- Sungthong, A., Nukeaw, J., and Pratontep, S. (2015). Silicon nitride thin Films deposited by reactive gas-timing magnetron sputtering for protective coating applications. *Advanced Materials Letters*, 6, 554-559.
- Tripathi, A. K., Singh, M. K., Mathpal, M. C., Mishra, S. K., and Agarwal, A. (2013). Study of structural transformation in TiO₂ nanoparticles and its optical properties. *Journal of Alloys and Compounds*, 549, 114–120.
- Wang, B., Qi, H., Wang, H., Cui, Y., Zhao, J., Guo, J., Cui, Y., Liu, Y., Yi, K., and Shao, J. (2015). Morphology, structure and optical properties in TiO₂ nanostructured films annealed at various temperatures. *OPTICAL MATERIALS EXPRESS*, 5(11), 1410-1418.
- Wang, B., Wei, S., Guo, L., Wang, Y., Liang, Y., Xu, B., Pan, F., Tang, A., and Chen, X. (2015). Effect of deposition parameters on properties of TiO₂ films deposited by reactive magnetron sputtering. *Ceramics International* 43(14), 10991-10998.

- Wang, D., Zhao, J., Chen, B., and Zhu, C. (2008). Lattice vibration fundamentals in nanocrystalline anatase investigated with Raman scattering. *Journal of Physics. Condensed Matter*, 20(8), 085212.
- Wang, L., Jiang, Y., Jiang, C., Liu, H., Ji, Y., Zhang, F., Fan, R., and Chen, D. (2018). Effect of oxygen flow rate on microstructure properties of SiO₂ thin films prepared by ion beam sputtering. *Journal of Non-Crystalline Solids*, 482, 203-207.
- Wang, L., Liu, H., Jiang, Y., Yang, X., Liu, D., Ji, Y., Zhang, F., and Chen, D. (2017). Effects of hot-isostatic pressing and annealing post-treatment on HfO₂ and Ta₂O₅ films prepared by ion beam sputtering. *Optik*, 142, 33-41.
- Xiong, Z., Wu, H., Zhang, L., Gu, Y., and Zhao, X. S. (2014). Synthesis of TiO₂ with controllable ratio of anatase to rutile. *Journal of Materials Chemistry A*, 2, 9291-9297.
- Xiong, Z., Wu, H., Zhang, L., Gu, Y., and Zhao, X. S. (2014). Synthesis of TiO₂ with controllable ratio of anatase to rutile. *Journal of Materials Chemistry. A*, 2(24), 9291.
- Yoshiya, M., Tanaka, I., Kaneko, K., and Adachi, H. (1999). First principles calculation of chemical shifts in ELNES/NEXAFS of titanium oxides. *J. Phys.: Condens. Matter* 11, 3217–3228.
- Zhan, C., Ke, W. J., Li, X. M., Du, W. L., Wang, L. J., and Ye, C. (2013). The Influence of Substrate Temperature on the Morphological and Optical Properties of ZnTiO₃ Thin Films Prepared by Magnetron Sputtering. *Advanced Materials Research*, 804, 3-7.
- Zhang, H., Chen, B., and Banfeld, J. F. (2008). Atomic structure of nanometer-sized amorphous TiO₂. *Phys Rev B*, 78, 214106.
- Zhang, J., Li, M., Feng, Z., Chen, J., and Li, C. (2005). UV Raman Spectroscopic Study on TiO₂. I. Phase Transformation at the Surface and in the Bulk. *the Journal of Physical Chemistry. B*, 110(2), 927–935.
- Zhang, Y., Jiang, Z., Huang, J., Lim, Y. L., Li, W., Deng, J., Gong, D., Tang, Y., Lai, Y., and Chen, Z. (2015). Titanate and Titania Nanostructured Materials for Environmental and Energy Applications: A Review. *RSC Advances*, 1-31.

Zhao, Y., Zhao, Y., Shi, R., Wang, B., Waterhouse, H. I. N., Wu, L. Z., Tung, C. H., and Zhang, T. (2019). Tuning Oxygen Vacancies in Ultrathin TiO_2 Nanosheets to Boost Photocatalytic Nitrogen Fixation up to 700 nm. *Advanced Materials*, 31(16), 1806482.





APPENDIX

Influence of Deposition Pressure on Local Structure, Optical and Structural Properties of Sputtered Silicon Oxide Thin Films

Ekachai Chongsereechoen^{a,b,*}, Piyaporn Thangdee^b, Rattikorn Yimnirun^c, Saroj Rujirawat^d, Suchinda Sattayaporn^d, Pattanapong Janphuang^d, Narong Chanlek^d, Mati Horprathum^e, Artit Chingsungnoen^f, Prayoon Songsirittigul^b

^a*Faculty of Science and Technology, Valaya Alongkorn Rajabhat University, Klong Luang, Pathum Thani 13180, Thailand*

^b*Research Network NANOTEC-SUT on Advanced Nanomaterials and Characterization, School of Physics, Institute of Science, Suranaree University of Technology, Nakhon Ratchasima 30000, Thailand*

^c*Research Network of NANOTEC-VISTEC on Nanotechnology for Energy and School of Energy Science and Engineering, Vidyasirimedhi Institute of Science and Technology, Wangchan, Rayong 21210, Thailand*

^d*Synchrotron Light Research Institute (Public Organization), Nakhon Ratchasima 30000, Thailand*

^e*Spectroscopic and Sensing Devices Research Group, National Electronics and Computer Technology Center (NECTEC), Klong Luang, Pathum Thani 12120, Thailand*

^f*Technological Plasma Research Unit, Department of Physics, Faculty of Science, Mahasarakham University, Mahasarakham 44150, Thailand*

*Corresponding Author's E-mail: ekachai@vru.ac.th

Abstract

Titanium oxide thin films were prepared by an RF magnetron sputtering by using TiO₂ ceramic target. Under the deposition condition i.e. the RF power of 60 watt, deposition time of four hours and the deposition pressure was varied from 2.2 – 16.8 Pa, the deposited thin films had shown amorphous structure. The local structure of the prepared thin films was measured at Ti K-edge by x-ray absorption near-edge structure (XANES). Surface morphology was investigated by scanning electron microscopy (SEM) and atomic force microscopy (AFM).

Their optical properties such refractive index and optical constants were investigated by a spectroscopic ellipsometry. Its optical transmittance spectra were obtained by an UV-Vis measurement. Finally, discussion related on the influences of deposition conditions on the structural and optical properties of the deposited films was made.

Keywords: Titanium oxide, Optical thin film, RF sputtering.

Abstract presented at the 21st International Union of Materials Research Societies – International Conference in Asia (IUMRS-ICA2020), 23-26 February 2021, Chiang Mai, Thailand



CURRICULUM VITAE

Name: Mr. Ekachai Chongsereechaoren

Place of birth: Kanchanaburi, Thailand

Education

Academic year

2001-2004 Silpakorn University, Nakhon Pathom, Thailand.

Bachelor of Science (Physics)

2005-2008 Chiang Mai University, Chiang Mai, Thailand.

Master of Science (Materials Science)

2018-2022 Suranaree University of Technology, Nakhon Ratchasima, Thailand. Doctor of Philosophy (Applied Physics)

Grants and Fellowships

- Scholarship for Potential Graduate Students to Study
- Research Network of Nanotechnology (RNN) Scholarship

Academic Experiences

- Research Assistant at BL3.2, Synchrotron Light Research Institute (Public Organization), Thailand.
- Teaching Assistant at Laboratory, School of Physics, Suranaree University of Technology, Thailand.

Position and Place of Work

- Lecturer at Faculty of Science and Technology,
Valaya Alongkorn Rajabhat University under the royal patronage, Pathum Thani